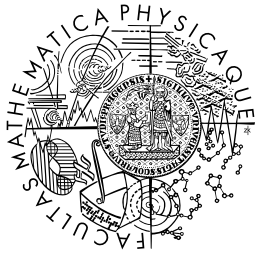

FACULTY
OF MATHEMATICS
AND PHYSICS
Charles University

DOCTORAL THESIS

Aurelio Gallardo

Theoretical study of charge states in molecular nanostructures on surfaces

Department of Condensed Matter Physics

Supervisor of the doctoral thesis: doc. Ing. Pavel Jelínek, Ph.D.

Study programme: Physics

Study branch: Physics of Condensed Matter and Materials Research

Prague 2022

I declare that I carried out this doctoral thesis independently, and only with the cited sources, literature and other professional sources. It has not been used to obtain another or the same degree.

I understand that my work relates to the rights and obligations under the Act No. 121/2000 Sb., the Copyright Act, as amended, in particular the fact that the Charles University has the right to conclude a license agreement on the use of this work as a school work pursuant to Section 60 subsection 1 of the Copyright Act.

In ..... date ....

Author's signature

A mis padres y hermanas.

Acknowledgements

First of all, I would like to thank Pavel Jelínek for the opportunity to be part of the Nanosurf group and for his friendly guidance.

I could not forget to also thank Blanca Biel, for giving me the opportunity to work with her, encouraging me to take up a research career.

I would not have been able to get here without the help of all the colleagues and friends I made at FZU and the CATRIN: Shayan Edalatmanesh, Jesús Redondo, Aleš Cahlik, Benjamin Mallada, Jack Hellerstedt, Federico Frezza, Qifan Chen, Andres Pinar, Ana Sanchez, Marco Lozano, Adam Matěj, Narendra Prabhakar, Christian Wäckerlin, Karl-Heinz Ernst, Bruno de la Torre, Hector Gonzalez, Jesus Mendieta, Diego Soler, Jose Martin Gago, Martin Švec, Jiři Doležal, Oleksander Stetsovych, Martin Ondracek, Pingo Mutombo, Prokop Hapala, Ondřej Krejči and Martina Zatkova.

I would also like to thank all my collaborators from the National University of Singapore, ÚOCHB, IMDEA, EMPA, CEITEC and Donostia International Physics Center. The value of the discussions we have had and the work we have developed is inestimable.

En especial quiero expresar el mayor de los agradecimientos a mi familia y amigos en España, por hacerme sentir tan cerca aun estando tan lejos.

Title: Theoretical study of charge states in molecular nanostructures on surfaces

Author: Aurelio Gallardo

Department: Department of Condensed Matter Physics

Supervisor: doc. Ing. Pavel Jelínek, Ph.D., Institute of Physics of the ASCR, v.v.i.

Abstract: Scanning probe microscopy (SPM) techniques are well known to provide images of molecular structures deposited on surfaces. Equipped with functionalized tips, these techniques have broadly demonstrated to achieve atomic resolution. However, the origin of certain aspects of the obtained images is still under debate.

This thesis investigates the origin of the sharp intermolecular features that frequently appear in the high-resolution SPM images. It is confirmed that the saddle points of the potential energy surface are the origin of the lateral bendings of the probe which are detected as narrow edges in the images. This situation can occur between non-covalently bonded atoms, due to their mere presence. Therefore, they cannot be interpreted as a direct representation of weak intermolecular bonds.

This text also describes the work done to obtain direct images of anisotropic charge distributions, such as σ-holes, using a Kelvin probe force microscope with a properly functionalized tip. The simulations performed using a model developed expressly for this project demonstrate that the images obtained experimentally can reflect both the electrostatics of the tip and the sample.

Additionally, the isomerization of organometallic chains, driven by the strain induced by the substrate on which the chains lie is characterized. To this end, theoretical ab-initio simulations of the molecular dynamics based on density functional theory were performed, which elucidated key aspects of the experimental process.

Keywords: Density functional theory (DFT), electronic structure, Kelvin probe force microscopy (KPFM), molecular electronics, on-surface synthesis.

Contents

Introduction

The research on the surface of solids has been growing in recent decades, boosted by the advances in ultra-high vacuum (UHV) and surface analysis techniques. In the last years, many authors have published their research about the behaviour of different structures deposited on the surfaces of solids. For example, the deposition and self-assembly of molecules in ordered structures[1–5] or the formation of one-dimensional (1D) molecular chains[6–8] has been largely investigated. Another good example are the two-dimensional (2D) planar materials, which have been widely investigated,[9,10] mainly since the experimental isolation of graphene in 2004.[11]

Surface sciences usually focus on model systems consisting of predominantly clean, homogeneous or ordered materials. Also, the structures that are grown or the molecules that are deposited on these surfaces do so under extremely controlled conditions. That is why most of these experiments are carried out under UHV conditions, in order to properly prepare and preserve the desired chemical and physical properties of the samples.

For the preparation and preservation of such samples, surface physics counts with a broad variety of experimental techniques.[12] The low energy electron diffraction (LEED) technique for example, is commonly used to characterize the crystallographic order of the sample. Another good example could be the X-ray photoelectron spectroscopy (XPS), where the photoemission of core-level electrons from the sample after its exposition to X-ray light will reveal information about the chemical composition of the surface. Nevertheless, these two examples will only provide information that is averaged over areas of the order of micrometers, missing for example the description of isolated defects or molecules.

It was not until the invention of the scanning tunnel microscope (STM) and the atomic force microscope (AFM)[13,14] that it became possible to image the surfaces in real space at nanometric levels and beyond. These techniques also allowed to manipulate individual atoms on the surface and control the compounds absorbed on it at molecular level. Since then, many modifications have been made to the so-called scanning probe microscopy (SPM) family of experimental techniques. One of the most important improvements was probably the functionalization of the tip by attaching an atom or molecule to its apex.

The experimental development of surface sciences has been accompanied by a similar development of theoretical methods. For example, different models for the simulation of SPM experiments have been proposed and implemented.[15–20] Furthermore, different theoretical approaches have been used to study the electronic and atomic structure of the molecules and solids. The most extended option to describe large atomic structures is probably the density functional theory (DFT), but many approaches could be found in the literature.[21–23] Also, the ab-initio molecular dynamics (MD) simulations[24] had been gaining attention in the last decades, due to their proficiency to describe molecular transformations.[25–29]

The following chapters can be divided into two groups. The first three chapters introduce the essential theoretical foundation behind the calculations and results presented afterwards. Then, the three last chapters introduce three papers published by the author of this thesis and his colleagues. These three works

were chosen among the author's publications to exemplify how useful the computational methods are for the study of molecules in the solid-vacuum interface.

Chapter 4 introduces the work carried out to analyze the imaging mechanism of certain SPM techniques. Using the probe particle (PP) model[15], we investigated the origin of the SPM signal when the probe scans the area between halogenated benzene rings absorbed on a metallic substrate. Based on the obtained results, we discuss the extensively debated topic of non-covalent bond visualization using SPM.

Then, chapter 5 details the motivation, implementation and theoretical background of a computational model developed to simulate Kelvin probe force microscopy (KPFM) experiments. We implemented this model with the aim of assisting the KPFM experiments that were performed to study the electrostatic character of halogenated tetraphenyl molecules. The main outcome of this experiment was the novel visualization of the σ-hole exhibited by one of the studied molecules. This result demonstrates not only the already predicted existence of the σ-hole but also the capability of the KPFM to achieve subatomic resolution.

Finally, chapter 6 summarizes the calculations performed to characterize the isomerization of molecular chains deposited on a metallic substrate. In this project, we used AFM simulations to confirm our interpretation of the experimentally obtained images. We also used DFT calculations to elucidate the driving force of the internal transformations suffered by the chains during the annealing at room temperature. To complete the characterization of the chains isomerization, we performed quantum mechanics/molecular mechanics (QM/MM) based MD simulations to work out the most probable reaction mechanism. The QM/MM method allowed us to describe the system that we used to simulate the reaction with a combination of DFT and empirical force fields, keeping the calculation computationally affordable.

1. Scanning probe microscopy

The Scanning probe microscopy (SPM) is a group of experimental techniques that consists of the sample's surface examination using an atomically sharp tip. Essentially, a needle is brought close to the sample, as it is schematized in Figure 1.1, up to nanometric distances. Then the tip is moved across the sample, recording certain quantities that depends on the tip-sample interaction, to map the sample surface and control the scanning process.

Since the scanning tunnel microscope (STM) was invented,[13] several variations of this technique had been developed, creating the SPM family. This chapter introduces the basic theory of the experimental SPM modes studied theoretically during this thesis.

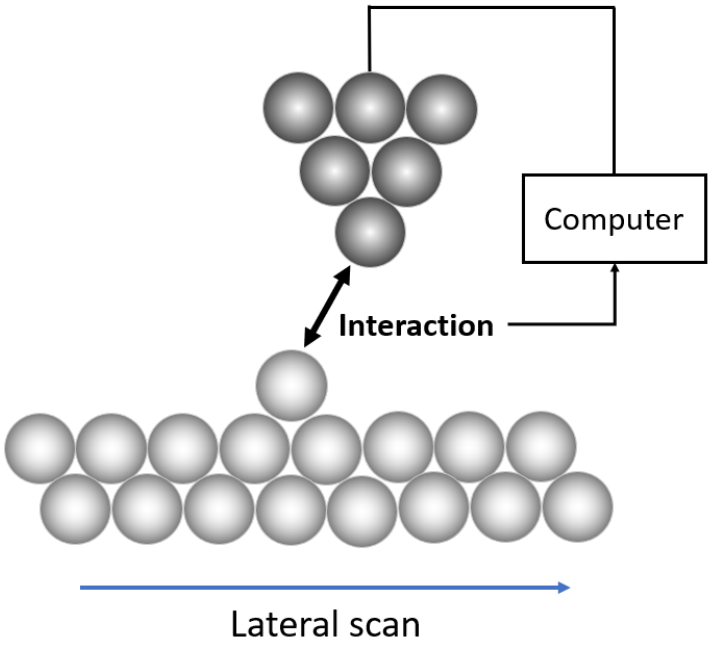

Figure 1.1: *Scheme of a general SPM setup. The tip, controlled by the computer, scans a certain characteristic of the surface. The tip-sample interaction is both recorded as data by the computer and used to adjust the control of the tip.*

1.1 Scanning tunnel microscopy

The STM technique records the tunnel current that flows between the tip and the sample when they are subject to a external potential difference. This current can be approximated as the electrons tunneling between two electrodes brought close together, separated by a potential barrier, and under an external bias voltage (see Figure 1.2).

Based on the work of Bardeen for a metal-oxide-metal interface,[30] the quantum tunnel current between tip and sample can be described by means of perturbation theory:[31]

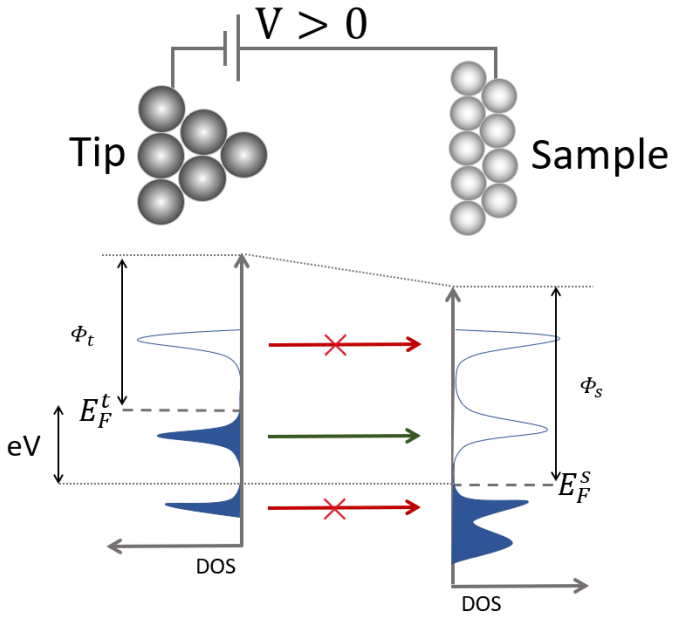

Figure 1.2: *Schematic depiction of a STM tip-sample system. The positive applied potential lowers the energy levels of the sample allowing the electrons to tunnel between compatible states. The green arrow exemplifies a certain allowed transition between a initial state in the tip and a final state in the sample. The red arrows indicate forbidden transitions because the initial state is empty (upper arrow) or because the final state in filled (bottom arrow).*

$$I = \frac{4\pi e}{\hbar} \int_0^{eV} \rho_{tip}(E_F^t + \varepsilon)\rho_{sample}(E_F^s + \varepsilon - eV)|M_T|^2 d\varepsilon, \tag{1.1}$$

where ρ_{tip} and ρ_{sample} are the densities of states (DOS) of tip and sample, with fermi levels E_F^t and E_F^s respectively, ε is the energy of a given electron tunneling from tip to sample, and M_T is the transmission matrix between the initial and final states.

The elements of the matrix M_T, assuming a single orbital in the tip for simplicity, can be approximated using the Chen's rules[16,32,33] as:

$$M_T = \sum_a^{atoms} 4\pi C_a \kappa^{\frac{1}{2}} e^{-\kappa|r_a|} \cdot \sum_\alpha^{orb.} Y_\alpha c_{a,\alpha}, \tag{1.2}$$

where the index a sums over all the atoms in the sample and α over all the orbitals in the atom a, Y_α is the spherical harmonic that corresponds to the orbital α, $c_{a,\alpha}$ is a weight prefactor to the orbital α of the atom a, κ is the decay length that depends on the the work function of the tip (Φ_t) and sample (Φ_s), r_a is distance between the tip and the scanned atom and C_a is an amplitude constant for the transition between the tip and the atom a.

To summarize, the tunnel current depends on the density of states of tip and sample, the shape of the corresponding wave functions, the work function of the tip and sample and the distance between them.

1.2 Atomic force microscopy

A few years after the invention of STM, the atomic force microscope (AFM) appeared.[14] This technique detects the direct interaction forces between the tip and the sample, eliminating the need of conducting sample/tips.

The components of the interaction force can be divided in long range (LR) and short range (SR) forces. At distances of a few Angstroms, the Pauli exclusion between the electrons of tip and sample manifest in the form of a repulsive force that decay exponentially with the distance. In the same region, the dispersion interaction between atoms contributes with an attractive force to compensate the Pauli repulsion. The interplay between Pauli repulsion and SR dispersion can be described with the LJ force field:

$$V(r) = V_0\left[-2\left(\frac{\sigma}{r}\right)^6 + \left(\frac{\sigma}{r}\right)^{12}\right], \tag{1.3}$$

where r is the distance between a pair of atoms that have a minimal interaction energy V_0 at $r = \sigma$, as it is shown in Figure 1.3.

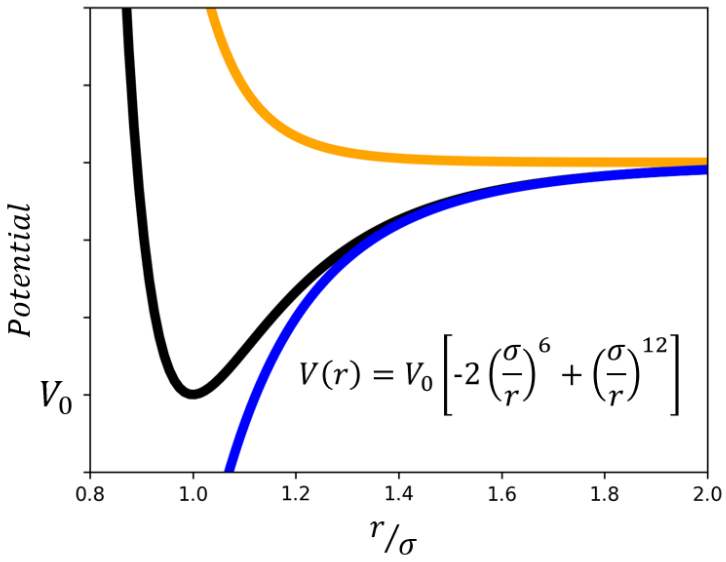

Figure 1.3: *Lennard-Jones potential components. The dispersion interaction between a pair of atoms is plotted in blue, the Pauli repulsion in orange and total potential in black. The depth of the energy well is given by the constant V_0 and its position by σ.*

In the case of tips and samples with net charge, an electrostatic interaction (V_{El}) will also act between them:

$$V_{El}(r) = \frac{1}{4\pi\varepsilon_0}\frac{Q_t Q_s}{r}, \tag{1.4}$$

where ε_0 is the vacuum permittivity and Q_t and Q_s are the net charges of tip and sample. Additionally, chemical interactions could appear at really close distances, where the orbitals of tip and sample overlap.

At large tip-sample distances, the electrostatic interaction still present as it decays as $1/r$. Also, despite the fast decay of the SR dispersion interaction between

atom pairs, the LR dispersion interaction between the macroscopic tip and the sample's substrate still present. For the case of a spherical tip of radius R_{tip} and an infinite plane that represents the sample, the LR dispersion interaction is given by:[34,35]

$$V_{LR-disp.} = -\frac{A_H R_{tip}}{6z}, \tag{1.5}$$

where A_H is the Hamaker constant, that depends on the type of materials that constitute the tip and sample, which usual values are of the order of 1 eV.

1.2.1 Operation modes

Different experimental approaches are usually used to detect the tip-sample interaction forces. The AFM operation methods can be basically cataloged in static and dynamics modes.

In static mode, the tip is brought close the sample and the surface is mapped observing the vertical deflection of the tip due to its interaction with the sample. In the dynamic mode instead, the tip is externally driven by an oscillating arm called cantilever that will act as force sensor.

Essentially, in the dynamic mode, the cantilever is externally excited to its eigenfrequency (f_0). Then, the tip-sample interaction force is detected by the changes it induces in the oscillation of the cantilever. In amplitude modulation AFM mode (AM-AFM), changes in the oscillation amplitude are measured, while in the frequency modulation AFM mode (FM-AFM) the amplitude is keep constant and shifts in the frequency are recorded.

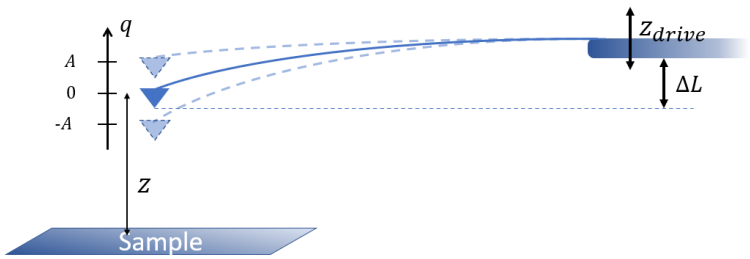

Figure 1.4: *Scheme of a nc-AFM set up. The driving force $F_{drive} = -kz_{drive}$ induces and oscillation to the cantilever. The swinging movement of the tip (placed at the end of the cantilever) is perturbed by the tip sample interaction and the changes in the dynamics of the tip are recorded as force descriptors.*

This thesis presents computational simulations of the FM dynamic mode of non-contact AFM (nc-AFM). In this modality, the dynamics of the tip can be modeled, as illustrated in Figure 1.4, using a driven-damped harmonic oscillator:[31]

$$m\ddot{q}(t) + \frac{m\omega_0}{Q_{cant}}\dot{q}(t) + k(q(t) - z_{drive} - \Delta L) = F_{ts}(z + q(t)), \tag{1.6}$$

where k, ω_0, m and Q_{cant} are the elastic constant, natural angular frequency, mass and quality factor of the cantilever, ΔL and z are the equilibrium position of the tip with respect to the base of the cantilever and the sample respectively,

F_{ts} is the tip sample interaction, $-kz_{drive}$ is the driving force according to Hook's law and $q(t)$ is the tip oscillation position around the equilibrium position.

The frequency shifts Δf induced by the tip-sample interaction force (F_{ts}), assuming and harmonic solution and small shifts on the angular frequency ($\Delta\omega << \omega$), is:[36]

$$\Delta f = \frac{1}{A^2 k} \int_0^T F_{ts}[z + q(t)] \cdot q(t) dt, \tag{1.7}$$

where the frequency shift Δf is proportional to the time average of the product of F_{ts} and $q(t)$ over a complete oscillation of period T and amplitude A.

1.3 Kelvin probe force microscopy

The Kelvin probe force microscopy (KPFM) adapts the Kelvin probe experiment[37] to a nc-AFM set-up with the aim of map the electrostatic character of surfaces. This technique records the variations of electrostatic interaction force between tip and sample when an external potential is applied between them.

To obtain a theoretical description of the interaction mechanism, the far and close tip-sample distance regimes need to be treated independently. The theoretical model for the macroscopic long range interaction is described in the following, and the interaction at close tip-sample distances will be treated in chapter 5 with a model developed by the author.

At far tip-sample distances the KPFM system can be modeled as the plates of a capacitor. This model starts considering two conductive materials, the tip and the sample, with different work function, brought close to each other at a distance z (Figure 1.5a). Then, when the two materials get connected with a wire (Figure 1.5b), a flow of electrons occurs to balance their Fermi levels. This charge reorganization creates opposite superficial charges that attract each other with an energy:

$$E_{KPFM} = \frac{1}{2}\frac{Q^2}{C(z)} = \frac{1}{2} C(z) V_{CPD}^2 = \frac{1}{2} C(z) (\Phi_t - \Phi_s)^2, \tag{1.8}$$

where $C(z)$ is the capacitance of the tip-sample system, Q is the superficial charge created on each plate and the so-called contact potential difference V_{CPD} is defined as the difference between the work function of tip Φ_t and sample Φ_s.

To determine the value of V_{CPD}, an external bias (V) is applied to revert the charge reorganization and nullify the electrostatic attraction (See Figure 1.5c):

$$E_{KPFM} = \frac{1}{2} C(z) (V - V_{CPD})^2. \tag{1.9}$$

Hence, as V is known, the V_{CPD} and therefore the difference between work functions $V_{CPD} = \Phi_t - \Phi_s$ is determined.

The experimental determination of the V_{CPD} is done using a nc-AFM setup, commonly using frequency modulation, analyzing the dependence of force with V through the frequency shift (Δf). The bias dependent force between tip and sample (F_{KPFM}), due to the superficial charges, can be derived from equation 1.9:

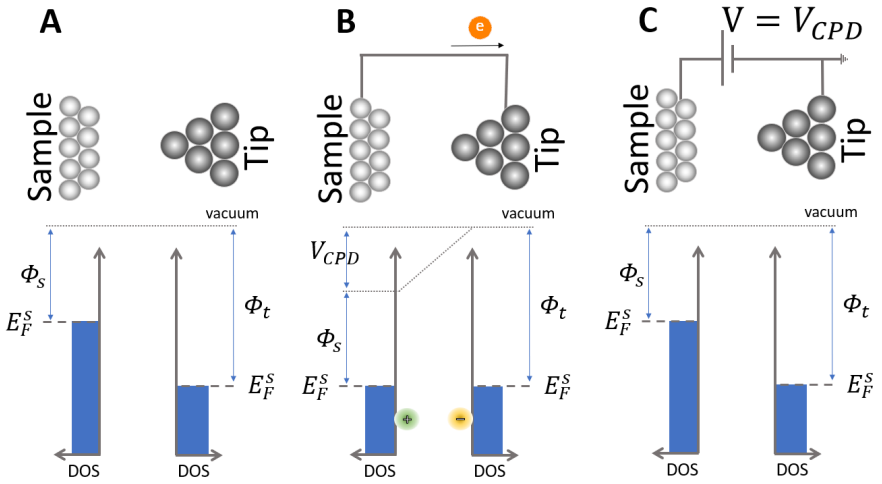

Figure 1.5: *Density of states scheme of the capacitor model of a KPFM set-up. (**A**) Before the electric connection. (**B**) electrically connected, the Fermi levels balance and the contact potential difference force appears. (**C**) After the V_{CPD} is externally compensated.*

$$F_{KPFM} = \frac{1}{2}\frac{\partial C\,(z)}{\partial z}\,(V - V_{CPD})^2\,. \tag{1.10}$$

F_{KPFM} is always attractive, as $C(z)$ is inversely proportional to the plates distance z, and with a minimal magnitude at $V = V_{CPD}$. When this force is added to the total force F_{ts} in equation 1.7 and the Δf is represented as a function of the external bias voltage, a parabola which maximal point is centered at V_{CPD} is obtained (see Figure 1.6A).

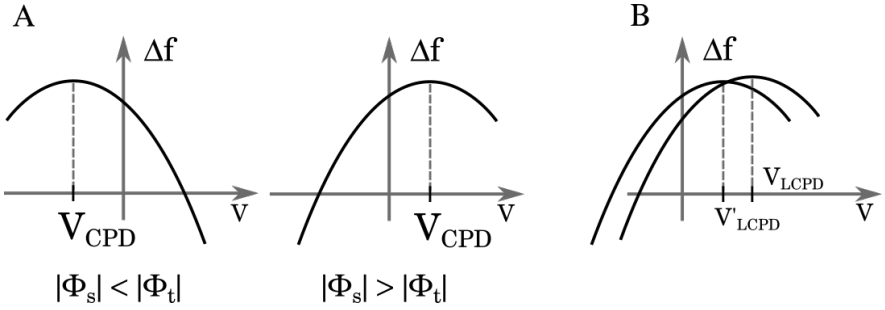

Figure 1.6: *Depiction of the frequency shift vs applied bias parabolas ($\Delta f(V)$) commonly obtained in KPFM experiments. (**A**) Examples of $\Delta f(V)$ parabolas obtained at far tip-sample distances. The values of V_{CPD} in this case are determined by the work functions of the tip (Φ_t) and sample (Φ_s). (**B**) At close tip-sample distances, the local values of the contact potential difference (V_{LCPD}) depend on the tip lateral position.*

At far tip-sample distances, the value of V_{CPD} is independent of the tip-sample relative lateral position and depends only on the difference between the work functions of tip and sample $V_{CPD} = \Phi_t - \Phi_s$ (see Figure 1.6A). On the other hand, local differences on the values of V_{CPD} can be observed at close tip-sample distances (Figure 1.6A). The different values in this case are labeled V_{LCPD}

(local contact potential difference) to distinguish these from the macroscopic term V_{CPD}. The origin of the local variations of V_{CPD} are discussed in chapter 5, where a theoretical model is implemented to describe the physical mechanism behind a series of experimentally obtained results.

1.4 Tip functionalization

One of the mayor advances in SPM microscopy in the last years was the discovery of the enhanced molecular resolution that could be achieved functionalizing the microscope's tip. Placing an inert molecule on the apex of a metallic tip notably reduces its chemical reactivity. At the same time, the molecule will become the mechanically softest part of the tip-sample junction. As a consequence of this functionalization, the microscope can operate at short tip-sample distances, allowing to map the interaction at repulsive distances without inducing permanent changes in the sample or the tip.

Leo Gross and his colleges presented in 2009[38] the first high-resolution AFM images of pentacene molecules using a carbon monoxide (CO) functionalized tip, triggering a deep research on tip fuctionalized AFM.[39] The contrast enhancing in the case of AFM is attributed to the capacity to obtain images at repulsive distances and the lateral bending of the molecule that decorates the tip.[15,40]

The enhancement of STM resolution due to the decoration of the tip with a flexible molecule is also well documented. In 2005, Jascha Reep et al.[41] used a pentacene decorated tip to obtain images of the molecular orbitals of other pentacene molecules with submolecular resolution. A few years later, Ruslan Temirov et al.[42] found the resolution of their STM images enhanced after allowing the admission of molecular hydrogen in the vacuum chamber that contains the tip-sample system. For the case of a CO terminated tip, the enhanced contrast in STM is attributed to the highly directional mixture of s and p_z orbitals that terminate the CO molecule[43] and the lateral relaxation of the CO molecule.[16]

Additionally, an special feature of STM with CO decorated tip was introduced by the group of Wilson Ho, the inelastic electron tunnel spectroscopy (IETS).[44] This technique detects the inelastic tunnel events, recording the second derivative of the tunnel current (d^2I/dV^2) obtained with a CO decorated tip measuring across the sample.

An inelastic tunneling event can occur in STM when the applied bias voltage match the energy of the vibrational modes of the molecules in the tunnel junction.[45] Also, the energy of the vibrational modes of a CO molecule attached to the STM tip will be sensible to the tip sample interaction. Knowing this, the tip-sample interaction can be measured scanning the surface with a CO decorated tip at a bias close to energy of the frustrated translation mode of the CO molecule ($E_{vib} \sim 2.4meV$). Then, the changes in E_{vib} will be reflected in d^2I/dV^2, that will show sharp peaks at repulsive distances, where the decorating molecule bends laterally.

1.5 Probe particle model

The probe particle (PP) model is a family of theoretical models that characterize different SPM techniques, initiated in 2014 by Hapala et al.[15] with a PP model for AFM (PPAFM). The model introduces the concept of PP, that describe the flexible atom/molecule at the tip apex as a single particle (depicted as the black atom in Figure 1.7) that is bond to the tip apex by certain harmonic recovery forces (F_{spring} and F_{lat} in Figure 1.7).

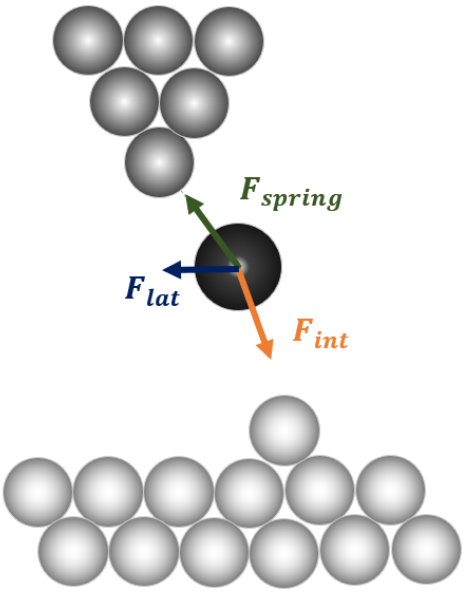

Figure 1.7: *Scheme of the concept of probe particle.[15] The atom/molecule that decorates the tip is modulated as a single particle (black atom) bonded to the tip by the recovery force F_{spring} and the lateral stiffness F_{lat}*

The AFM modality of the the PP model[15] relaxes the position of the probe particle under the interplay of F_{spring}, F_{lat} and the probe-sample interaction force (F_{int}), as depicted in Figure 1.7. F_{int} is described using a LJ potential (see equation 1.6 and Figure 1.3). Finally, the Coulomb electrostatic interaction based on the Hartree potential calculated from density functional theory (DFT) can be included.[46] Then, the frequency shift is calculated using the method proposed by Giessibl.[36]

The model closely reproduces the experimental results, with blunt contrast in the attractive region and sharp edges at repulsive distances. This is due to the lateral depletion of the probe near the saddle points of the potential energy surface of the sample. The relation between the observed sharp edges and the presence of bonds in the sample is extensively discussed in the literature[15,47] as well as in the chapter 4.

The PP model is also designed to describe the IETS mode with a CO decorated tip.[46] This modality calculate the changes induced by F_{int} in the vibrational modes of a CO molecule attached to the tip. This modality of the model reproduces the expected sharp peaks and edges in the d^2I/dV^2 signal due to the softening of the normal modes associated with the lateral bending (see Figure 11 in ref.[46]).

Besides a simple STM model was included in the original PP model[15] based on exponential tunnel hoppings, Krejčí et al.[16] introduced a more sophisticated model, combining the PPAFM mechanics of the probe and Chen's rules to describe the tunneling process. The results discussed in the original paper already demonstrates that the spatial distortion induced by the deflection of the flexible probe is crucial to reproduce the experimental findings.

The PP model toolkit family had demonstrated to be extremely useful to understand the experimental results obtained with functionalized tips. Therefore, with the aim of contributing to this effort, an important part of the present thesis is dedicated to extend this model to describe the short range contrast in KPFM experiments.

2. Quantum description of atomic assemblies.

Atomic systems such as bulk materials, surfaces, molecules, etc. can be described solving the quantum-mechanic stationary Schrödinger equation:

$$H\Psi = E\Psi, \tag{2.1}$$

in which Ψ is the wave function of the system, E is the corresponding energy eigenvalue and H is the Hamiltonian operator that describes the system.

The complete many-body Hamiltonian of a system formed by N_{atm} ions and N electrons is:

$$H = T_n + V_{n-n} + T_e + V_{e-e} + V_{n-e}, \tag{2.2}$$

where, T_n is the sum of kinetic energy of all the nuclei with mass M_α at position $\vec{R}_\alpha$:

$$T_n = -i\hbar \sum_{\alpha=1}^{N_{atm}} \frac{1}{2M_\alpha} \left(\frac{\partial}{\partial \vec{R}_\alpha} \right)^2, \tag{2.3}$$

V_{n-n} sums the coulomb interactions between the α^{th} and β^{th} nuclei with atomic numbers Z_α and Z_β for all the atoms:

$$V_{n-n} = \sum_{\alpha}^{N_{atm}} \sum_{\beta \neq \alpha}^{N_{atm}} \frac{Z_\alpha Z_\beta e^2}{|\vec{R}_\alpha - \vec{R}_\beta|}, \tag{2.4}$$

T_e is the kinetic energy of all the electrons with mass m_e at positions $\vec{r}_i$:

$$T_n = -i\hbar \sum_{i=1}^{N} \frac{1}{2m_e} \left(\frac{\partial}{\partial \vec{r}_i} \right)^2, \tag{2.5}$$

V_{e-e} sums over the interactions between the i^{th} and j^{th} electrons:

$$V_{e-e} = \sum_{i}^{N} \sum_{j \neq i}^{N} \frac{e^2}{|\vec{r}_i - \vec{r}_j|}, \tag{2.6}$$

and the last term, V_{n-e}, is the electron-nuclei interaction:

$$V_{n-e} = -\sum_{\alpha=1}^{N_{atm}} \sum_{i=1}^{N} \frac{e^2 Z_\alpha}{|\vec{R}_\alpha - \vec{r}_i|}. \tag{2.7}$$

The Schrödinger equation (2.1), with a complete Hamiltonian as the above described, is in most cases impossible to treat neither analytically or computationally and a series of approximations need to be assumed.

The first simplification, known as the Born-Oppenheimer approximation, assumes that the electrons move much faster than the nuclei and hence their dynamics can be separated. Further simplifications of the problem bifurcates in two kinds of methods, depending if they rely on the wave functions or in the electronic density of the system.

Originally, the quantum chemistry methods where, and in most cases still are, based in the calculation of the wave functions of the system. On the other hand, methods based in the density functional theory are preferred in fields like condensed matter physics. This chapter introduces briefly both approaches, in order to justify the election of the density functional theory (DFT) to describe the electronic structure of the systems studied in the present thesis.

2.1 One-electron approximation

An usual approach to a formalism based on the wave function is the one electron approximation in which the electronic wave function is separated in single electron wave functions. A simple way to formulate this approximation is the Hartree product, that for the simplest case of two electrons is:

$$\Psi_N\left(\vec{r}_1\sigma_1, \vec{r}_2\sigma_2\right) = \phi_1(\vec{r}_1, \sigma_1)\phi_2(\vec{r}_2, \sigma_2), \tag{2.8}$$

where the wave function of each electron ϕ_i depends on its position $\vec{r}_i$ and its spin state σ_i.

The main drawback of this formulation is its disregarding of the exchange interaction between electrons. To account for the exchange interaction, the wave function needs to be anti-symmetric under the exchange of the two electrons. To fulfill this condition, a more adequate formulation would be:

$$\Psi_N\left(\vec{r}_1\sigma_1, \vec{r}_2\sigma_2\right) = \frac{1}{\sqrt{2}}\Big[\phi_1(\vec{r}_1, \sigma_1)\phi_2(\vec{r}_2, \sigma_2) - \phi_1(\vec{r}_2, \sigma_2)\phi_2(\vec{r}_1, \sigma_1)\Big], \tag{2.9}$$

or in matrix representation:

$$\Psi_N\left(\vec{r}_1\sigma_1, \vec{r}_2\sigma_2\right) = \frac{1}{\sqrt{2}}\begin{vmatrix}\phi_1(\vec{r}_1, \sigma_1) & \phi_2(\vec{r}_1, \sigma_1)\\ \phi_1(\vec{r}_2, \sigma_2) & \phi_2(\vec{r}_2, \sigma_2)\end{vmatrix}.$$

This formulation for the general case of N electrons is known as single Slater determinant:

$$\Psi_N\left(\vec{r}_1\sigma_1, ..., \vec{r}_N\sigma_N\right) = \frac{1}{\sqrt{N!}}\begin{vmatrix}\phi_1(\vec{r}_1, \sigma_1) & \cdot & \cdot & \cdot & \phi_N(\vec{r}_1, \sigma_1)\\ \cdot & \cdot & & & \cdot\\ \cdot & & \cdot & & \cdot\\ \cdot & & & \cdot & \cdot\\ \phi_1(\vec{r}_N, \sigma_N) & \cdot & \cdot & \cdot & \phi_N(\vec{r}_N, \sigma_N)\end{vmatrix},$$

where if the electrons i and j with the same spin ($\sigma_i = \sigma_j$) occupy the same point of the space ($\vec{r}_i = \vec{r}_j$), the i^{th} and j^{th} rows of the determinant will be identical, vanishing the wave function.

Using the Slater representation of the wave function in the Schrödinger equation leads to the Hartree-Fock (HF) equations:

$$-\frac{\hbar^2\nabla^2}{2m_e}\phi_i\left(\vec{r}, \sigma\right) + \Big[\sum_{\sigma'}\int d\vec{r}\,'\; V_{eff}^{HF}\left(\vec{r}\sigma, \vec{r}\,'\sigma'\right)\Big]\phi_i\left(\vec{r}\,', \sigma'\right) = \varepsilon_i\phi_i\left(\vec{r}, \sigma\right), \tag{2.10}$$

where $V_{eff}^{HF}\left(\vec{r}\right)$ is the effective (HF) potential:

$$V_{eff}^{HF}\left(\vec{r}\sigma,\vec{r}\,'\sigma'\right)=\delta_{\sigma,\sigma'}\delta\left(\vec{r}\,'-\vec{r}\right)\left[V_{ion}\left(\vec{r}\right)+V_{H}\left(\vec{r}\right)\right]+V_{x}\left(\vec{r}\sigma,\vec{r}\,'\sigma'\right). \tag{2.11}$$

The three terms that constitute the HF potential are the potential created by the nuclei $V_{ion}\left(\vec{r}\right)$, the Hartree potential created by the rest of electrons $V_H\left(\vec{r}\right)$, and the exchange potential $V_x\left(\vec{r}\right)$:

$$V_{ion}\left(\vec{r}\right)=-\sum_{\alpha=1}^{N_{atm}}\frac{e^2Z_\alpha}{|\vec{R}_\alpha-\vec{r}|}, \tag{2.12}$$

$$V_H\left(\vec{r}\right)=-e^2\int d\vec{r}\,'\sum_{\sigma'}\sum_{j\neq i}^{N}\frac{|\phi_j\left(\vec{r}\,',\sigma'\right)|^2}{|\vec{r}\,'-\vec{r}|}, \tag{2.13}$$

$$V_x\left(\vec{r}\sigma,\vec{r}\,'\sigma'\right)=-e^2\sum_{j=1}^{N}\frac{\phi_i\left(\vec{r},\sigma\right)\phi_j^*\left(\vec{r}\,',\sigma'\right)}{|\vec{r}\,'-\vec{r}|}. \tag{2.14}$$

The main asset of the HF method is the exact treatment of the exchange interaction, but on the other hand, the correlation between electrons is completely neglected. Different formulations beyond HF are commonly used to include the correlation energy in the calculation. An extended option for example is to apply perturbation theory (Møller-Plesset)[48] to the electron-electron interaction. Another option is the so-called configuration interaction that applies the variational method, using a combination of Slater determinants as wave function to include unoccupied orbitals in the calculation. Nevertheless, this implementations beyond HF can become computationally very expensive for large systems.

2.2 Density functional theory

Condensed matter physics usually deals with systems too large to be treated with above mentioned methods based on HF. A common alternative are the methods based on the electronic density of the systems, offering a good balance between accuracy and computational cost.

2.2.1 Hohenberg–Kohn theorem

The density functional theory (DFT) relies on the Hohenberg–Kohn (HK) theorems[49] for a system of electrons under an external potential v_{ext}.

The first HK theorem states that the ground state wave function of the system Ψ is an unique functional of the electronic density $\rho(\vec{r})$:

$$\Psi=\Psi[\rho(\vec{r})], \tag{2.15}$$

and consequently, so it is the energy of the system:

$$E[\rho(\vec{r})]=\int d\vec{r}\rho(\vec{r})v_{ext}(\vec{r})+F[\rho(\vec{r})], \tag{2.16}$$

where the energy functional $F[\rho(\vec{r})]$ gathers the kinetic T and the electron-electron interaction V_{ee}:

$$F[\rho(\vec{r})] = \langle \Psi[\rho(\vec{r})] | T + V_{ee} | \Psi[\rho(\vec{r})] \rangle. \tag{2.17}$$

The second theorem introduces the variational principle to the energy density functional. It establishes that the ground state energy is given by the minimum of the energy density functional and that this minimum is only reached for the ground state electronic density.

The HK theorem allows to reduce the dimension of the problem from the original $3N$ spatial coordinates of the N electrons, to the the 3 spatial coordinates in which the density is defined. It also enables to find the ground state electronic density $\rho(\vec{r})$ and consequently the wave functions of the system minimizing the energy functional $E[(\rho(\vec{r}))]$.

Although the great level of simplification could suggest a similar loose in the rigorousness of the theory, is important to highlight that the treatment of the problem has been exact up to now. For its practical application however, certain parts of the functional $F[\rho(\vec{r})]$ are very difficult or directly impossible to express analytically. The exchange part of the electron interaction and the correlation part of the kinetic energy need to be separated and empirically characterized. The most commonly used approximations are commented in the section 2.2.3, after introducing the practical application of DFT by means of the Kohn-Sham equations.

2.2.2 Kohn-Sham equations

The practical solution of the problem is not usually found minimizing the energy functional, as the Hohenberg–Kohn theorem proposes, but through the Kohn-Sham (KS) equations. This method defines a non-interacting single-particle system, known as KS system, that has the same electronic density as the original system, under an external potential V_{eff}^{KS}:

$$\left\{ -\frac{\hbar^2 \nabla^2}{2m} + V_{eff}^{KS}\left[\rho(\vec{r})\right] \right\} \xi_i\left(\vec{r}\right) = \varepsilon_i \xi_i\left(\vec{r}\right), \tag{2.18}$$

where ξ_i are single-particle wave functions of the non-interacting system, and the ground state density of the system will be:

$$\rho^{KS}(\vec{r}) = \sum_{i=1}^{N} |\xi_i\left(\vec{r}\right)|^2. \tag{2.19}$$

For the electronic density of the KS system (ρ^{KS}) to match the density of the original system, the potential V_{eff}^{KS} should resemble the interaction between particles of the original system:

$$V_{eff}^{KS}\left[\rho(\vec{r})\right] = V_{ion}\left(\vec{r}\right) + V_H\left[\rho\left(\vec{r}\right)\right] + V_{xc}\left[\rho\left(\vec{r}\right)\right], \tag{2.20}$$

where V_{ion} is the potential created by the nuclei, V_H is the potential created by the electrons:

$$V_H[n\left(\vec{r}\right)] = \frac{1}{2} e^2 \int d\vec{r}\,' \frac{\rho(\vec{r})}{|\vec{r} - \vec{r}\,'|}, \tag{2.21}$$

and V_{xc} is the so-called exchange and correlation (XC) potential:

$$V_{xc}\left[\rho(\vec{r})\right] = \frac{\delta E_{xc}\left[\rho(\vec{r})\right]}{\delta\rho\left(\vec{r}\right)}, \tag{2.22}$$

where the exchange and correlation energy (E_{xc}) contains the many-body interactions that are not included analytically in the total energy, the exchange and the correlation energy. The correlation can be seen as the effect that the interaction between electrons has in the kinetic energy and the exchange corresponds to the repulsion between electrons with alike spin.

Because the V_{eff}^{KS} is a functional of $\rho(\vec{r})$, that is calculated from the set of wave functions $\{\xi_i\left(\vec{r}\right)\}$, the KS problem need to be solved self-consistently. The process starts with a guessed initial solution $\{\xi_i^{in}\left(\vec{r}\right)\}$ and the corresponding density $\rho^{in}(\vec{r})$ associated to it. Then, the KS equation is solved using $V_{eff}^{KS}[\rho^{in}(\vec{r})]$, obtaining the solution wave functions $\{\xi_i^{out}\left(\vec{r}\right)\}$ and its corresponding density $\rho^{out}(\vec{r})$. This cycle is repeated, as schematized in the flow-chart in Figure 2.1, until the convergence between $\rho^{in}(\vec{r})$ and $\rho^{out}(\vec{r})$ under a certain tolerance ζ_{tol} is reached.

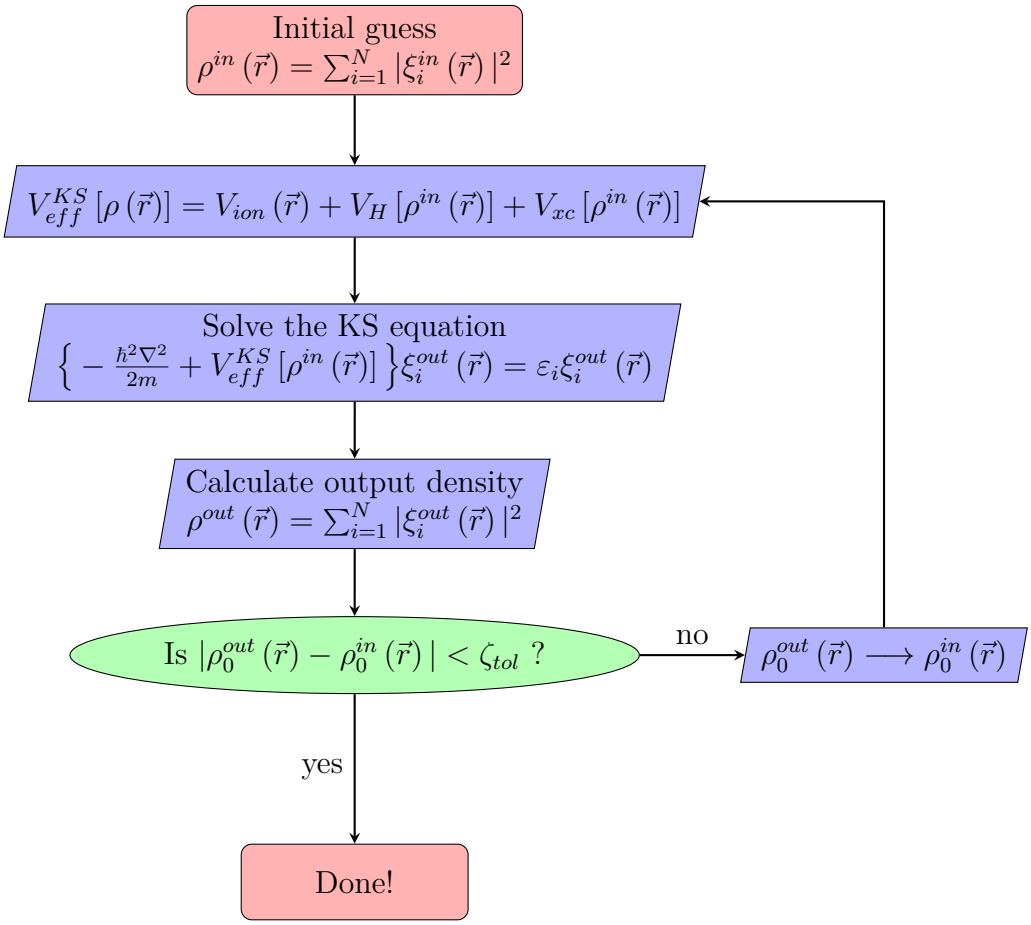

Figure 2.1: *Flow diagram of the self-consistent solution strategy of the KS equations. The potential of the system is calculated from an initial guess of the electronic structure of the system. Then, the KS equations are solved and the solution is used as a new initial guess until the convergence is reached.*

2.2.3 Exchange-correlation approximation method

The only thing yet to be done to solve the KS equations is to define the exchange and correlation energies. These components of the energy are usually described together by means of an exchange and correlation (XC) approximated functional.

The simpler of these potentials is the local density approximation (LDA).[50] This potential uses the XC energy per particle ($e_{xc}^{HEG}\{\rho(\vec{r})\}$) of an homogeneous electron gas (HEG) with the same electronic density as the KS system $\rho(\vec{r})$ to calculate the E_{xc} of the system:

$$E_{xc}^{LDA}[\rho(\vec{r})] = \int d\vec{r}\,\rho(\vec{r})\,e_{xc}^{HEG}\{\rho(\vec{r})\}. \tag{2.23}$$

While analytical forms of the exchange energy of the HEG can be used, the correlation needs to be obtained, for example, from the results of Monte Carlo calculations. Because $E_{xc}^{LDA}[\rho(\vec{r})]$ depends only on local values of $e_{xc}^{HEG}\{\rho(\vec{r})\}$, this approximation is specially adequate for homogeneous crystals and systems without abrupt changes in the density.

For the case of systems with higher inhomogeneity, such as molecules or defected systems, the general gradient approximation (GGA)[51–53] offers estimations of higher precision. The XC energy in this case is calculated from certain functions depending not only on the local value of the density of the system ($\rho(\vec{r})$), but also on its gradient ($\nabla\rho(\vec{r})$):

$$E_{xc}^{GGA}[n] = \int d\vec{r}\,\mathcal{F}\{\rho(\vec{r}), \nabla\rho(\vec{r})\}, \tag{2.24}$$

where the shape of the function $\mathcal{F}\{\rho(\vec{r}), \nabla\rho(\vec{r})\}$ will differ depending on the definition of the GGA potential.

Another family of functionals that offer an ever more precise description of the exchange energy are the so-called hybrid potentials. This option uses a mixture of the XC correlation energy calculated with an empirical potential and the exact exchange energy calculated with Hartree-Fock methods.[54,55]

2.2.4 Dispersion interaction

One last important aspect to comment in the context of DFT calculations is the inability of the above mentioned XC potentials to describe dispersion forces. The dispersion forces are a consequence of the instantaneous polarization of the electronic density in a given region of the space as a response to electronic fluctuations in another point of the space.

The usual XC potential does not consider instantaneous electronic fluctuations or non-local correlation, therefore additional terms are needed to consider the dispersion interaction. This section describes the most popular options, depending on their level of complexity.

The most common solution is adding a pairwise dispersion energy term to the total energy after the KS calculation:

$$E_{disp.} = -\frac{1}{2}\sum_{\alpha}^{N_{atm}}\sum_{\beta}^{N_{atm}}\left(f_n(R_{\alpha\beta})\frac{\sigma_{n,\alpha\beta}}{(R_{\alpha\beta})^n}\right);\ n = 6, 8, ... \tag{2.25}$$

where the damping function $f_n(R_{\alpha\beta})$ prevents the interaction to diverge for short distances and $R_{\alpha\beta}$ is the distance between the α^{th} and β^{th} atoms. The first term ($n = 6$) that decays with $1/R^6_{\alpha\beta}$ usually dominates the interaction, but higher order terms are occasionally included as well.

The simpler way to obtain the coefficients $\sigma_{n,\alpha\beta}$ is using tabulated values, this is known as dispersion corrected DFT (DFT-D) methods. The main flaw of using tabulated values is that it considers the dispersion interaction to be independent of the chemical state of the involved atoms. The polarizability of the electron cloud of an atom can be affected by its oxidation state or the presence of other atoms and is not necessarily isotropic.

Different approaches are available to reflect the effect of the structure of the system in the dispersion energy. The DFT-D3 formulation of Grimme et al.[56] for example counts the number of near neighbours of each atom to modify the values of $\sigma_{n,\alpha\beta}$ according to the expected changes in the polarizability. Also in 2009 a method considering the electronic structure of the system was proposed by Alexandre Tkatchenko and Matthias Scheffler.[57] This method divides the space, assigning a certain volume to each core to determine the charge that "belongs" to each atom. This density is then compared with the atomic charge of the free atoms, and this ratio is used to scale the values of the $\sigma_{n,\alpha\beta}$ coefficients.

More complex treatments are also available for the treatment of the dispersion interaction. For example, the inclusion of non-local correlation terms to the XC potential[58] or a many-body treatment of the coupling between atomic dipoles.[59]

This chapter intends to provide a brief introduction to the DFT and the quantum treatment of atomic assemblies for the less familiar readers. A far more detailed description of the aspects discussed here can be found in the literature.[22,23,60]

3. Quantum mechanics/ molecular mechanics in molecular dynamics calculations

The molecular dynamics (MD) methods are a computational approach to describe the time evolution of atomic systems. For the case of large systems which partition function can not be treated analytically, MD solves numerically the equations of motion of the particles that conform the system to obtain its average properties.

The Verlet algorithm[61] proposes a simple but effective method to solve the equations of motion, expanding the position and velocity of the particles of the system at a given time $t + \Delta t$ in Taylor series:[24]

$$r_i(t + \Delta t) = r_i(t) + v_i(t)\Delta t + \frac{\Delta t^2}{2m_i} F_i(t), \tag{3.1}$$

$$v_i(t + \Delta t) = v_i(t) + \frac{\Delta t}{2m_i}[F_i(t) + F_i(t + \Delta t)], \tag{3.2}$$

where r_i and v_i are the position and velocity of the i^{th} particle with mass m_i subjected to a force F_i. The Verlet algorithm consist on the recurrent solution of these equations, after choosing a set of initial conditions and an adequate time step Δt.

The procedure starts with a set of guessed initial positions $r_i(t = t_0)$, velocities $v_i(t = t_0)$ and forces $F_i(t = t_0)$, used to obtain $r_i(t + \Delta t)$ with the equation 3.1. Subsequently, the forces that affect the particles $F_i(t + \Delta t)$ are calculated and the new velocities of the particles are obtained using the equation 3.2. Then, the time is updated ($t = t + \Delta t$) and the process is repeated.

After repeating the algorithm a sufficient number of times and assuming the ergodicity of the system, the average value A of a given property of the system $a(t)$ can be obtained from the time average:

$$A = \langle a \rangle = \frac{1}{N_\tau} \sum_{n=1}^{N_\tau} a(t_0 + n\Delta t). \tag{3.3}$$

3.1 Calculation of the forces

In the previous section, the procedure to calculate the forces that affect the particles $F_i(t+\Delta t)$ was left unspecified. In this thesis the so called QM/MM (quantum mechanic/molecular mechanic) method[62,63] is used to describe the interaction between particles. This method describes the main regions of the system, where the chemical reactions occurs, with a quantum formalism and the surrounding areas using classical mechanics.

Empirical force fields provide a fast and reliable method to calculate the interaction forces between particles, but fails in the description of covalent bond formation and other charge density related effects. For the case of chemical reactions for example, where bonds are broken or created, quantum mechanic methods need to be used.

3.1.1 Classical forces

The classical treatment considers the particles under certain empirical potentials that decribe different aspects of the interaction:[64]

$$V = \sum_{ij\,bonded} K_{r,ij}(r_{ij} - r_{0,ij})^2 + \sum_{ijk\,bonded} K_{\theta,ijk}(\theta_{ijk} - \theta_{0,ijk})^2 + \sum_{ijkl\,bonded} \frac{1}{2} K_{\phi,ijkl}[1 + cos(n\phi_{ijkl} - \phi_{0,ijkl})] + \frac{1}{4\pi\varepsilon_0\varepsilon_r} \sum_{ij\,non-bonded} \frac{Q_i Q_j}{r_{ij}} + \sum_{ij\,non-bonded} V_{ij}\left[\left(\frac{\sigma_{ij}}{r_{ij}}\right)^{12} - 2\left(\frac{\sigma_{ij}}{r_{ij}}\right)^{6}\right], \tag{3.4}$$

where the first three terms of the right hand side sum over all the covalently bonded groups of atoms and the last two terms over pairs of atoms with no chemical bond between them.

The first term controls the bond length r_{ij} between the i^{th} and j^{th} atom to keep it similar to the empiric value $r_{0,ij}$ with an harmonic potential which stiffness is given by the constant $K_{r,ij}$. The second term controls the angle θ_{ijk} between the bonds that link the i^{th} with the j^{th} atom and the j^{th} with the k^{th} atom, where the $\theta_{0,ijk}$ is the empirical value and $K_{\theta,ijk}$ an empirical constant. The third term controls the dihedral angle ϕ_{ijkl} between the plane described by the atoms i, j and k and the one defined by the atoms j, k and l, as illustrated in Figure 3.1. This term uses a cosine with multiplicity n that minimizes this component of the energy for $\phi_{ijkl} = {}^{\phi_{0,ijkl}}/_{n}$ and a constant $K_{\phi,ijkl}$ that sets the rigidity of this condition.

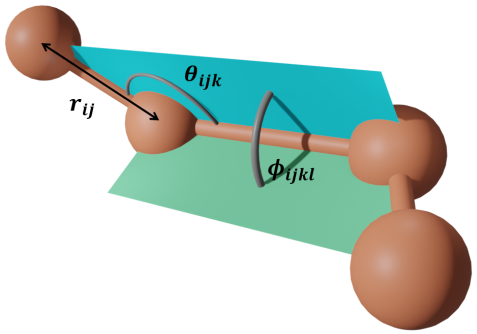

Figure 3.1: *Scheme of the definition of the distance r_{ij} and the angles θ_{ijk} and ϕ_{ijkl} in equation 3.4*

The fourth term is the coulomb interaction between the empirical charges Q_i and Q_j assigned to the i^{th} and j^{th} atoms and the last term is a Lennard-Jones (LJ) potential that describe the dispersion and Pauli interaction between not bonded atoms with σ_{ij} the position of the interaction minima (V_{ij}), as depicted in Figure 1.3.

3.1.2 Quantum forces

The formalism used in the present thesis for the description of the quantum region is the density functional theory (DFT) (see chapter 2). First, the ground state

energy of the quantum region E^0_{DFT} is calculated for a given set of coordinates at a time t. Then, the force that affect the nuclei of the atoms can be obtained from the calculated energy with the Hellman-Feynman theorem:[65]

$$F_\alpha = \frac{\partial}{\partial R_\alpha} E^0_{DFT}(R_\alpha) = \frac{\partial}{\partial R_\alpha} \langle \Psi_0 | H | \Psi_0 \rangle, \tag{3.5}$$

where F_α will be the force that affect the α^{th} atom in the position R_α. A more detailed derivation of this theorem can be found in the literature.[23]

3.1.3 QM/MM forces

When a system is described with the QM/MM method, the system is divided in two regions. The most important parts of the system are described with quantum methods and the remaining areas of the system are described with empirical force fields. Then, for the two regions to not be isolated from each other, the interaction between atoms of different regions need to be take into account.

To introduce the effect of the MM region into the QM region and vice versa, three basic interaction terms should be added to the Hamiltonians.[66] First, the interaction between the empirical charges and the DFT described electronic clouds is included with the term:

$$H^{QM/MM}_{e-e} = \sum_{k,\alpha,\beta} Q_k \int \frac{\phi_\alpha(\vec{r} - \vec{R}_\alpha)\phi_\beta(\vec{r} - \vec{R}_\beta)}{|\vec{r} - \vec{R}_k|} d\vec{r}, \tag{3.6}$$

where Q_k is the empirical charge of a classically described atom at position R_k, and ϕ_α and ϕ_β are two atomic orbitals at positions $\vec{R}_\alpha$ and $\vec{R}_\beta$.

The interaction between the empirical charge Q_k and the nuclei of the γ^{th} quantum described atom is:

$$H_{Q_k,\gamma} = \frac{e^2 Q_k Z_\gamma}{|\vec{R}_k - \vec{R}_\gamma|}, \tag{3.7}$$

where Z_γ is the atomic number of the γ^{th} atom at position $\vec{R}_\gamma$.

To conclude the connection between the QM and MM regions, the dispersion and Pauli interaction between the k^{th} classic atom and the γ^{th} quantum described atom is given a the Lennard-Jones (LJ) potential:

$$H^{LJ}_{k,\gamma} = V_{k,\gamma} \left[\left(\frac{\sigma_{ij}}{r_{k,\gamma}} \right)^{12} - 2 \left(\frac{\sigma_{ij}}{r_{k,\gamma}} \right)^{6} \right], \tag{3.8}$$

where $r_{k,\gamma}$ is the distance between the k^{th} and γ^{th} atoms of the QM and MM regions respectively.

3.2 Inclusion of temperature

In the present thesis, the molecular dynamics simulations are done within the frame of the canonical ensemble with the temperature included in the calculation by the Langevin thermostat[24] that ads an additional term to the particle's energy:

$$F_i^{temp} = -\gamma m_i v_i + \sqrt{2 m_i \gamma k_B T}\eta(t). \tag{3.9}$$

The constant γ is the frequency of collision between particles, T is the temperature, k_B is the Bolztman's constant and $\eta(t)$ is a distribution of uncorrelated variables that randomize the spread of instantaneous thermal energy among the particles. The inclusion of the temperature of the system in the calculation takes in consideration the effect of entropy, allowing to analyze the free energy landscape of the conformational space instead of the potential energy surfaces:

$$F = U - TS, \tag{3.10}$$

where F is the Helmholtz free energy, U is the potential energy and S is the entropy of the system.

Using this method we can include the effects of the thermal energy in the dynamics of the system. According to the virial theorem, the average thermal energy of an equilibrium system is $k_B T$. Nevertheless, the instantaneous energy of each vibrational mode fluctuates with time. This means that a certain mode can eventually gather enough energy to overcome a barrier of energy higher than the mean thermal energy $\langle E \rangle = k_B T$ in its direction of vibration in the conformational space.

4. Origin of sharp contrast in scanning probe microscopy

Sharp features in SPM are usually considered as a direct visualization of atomic bonds in the sample. In AFM/IETS experiments, the charge that accumulates between covalently bonded atoms of the sample interacts repulsively with the tip at close distances, causing the lateral relaxation of the probe. For the case of intermolecular features, the direct relation between the non-covalent interactions among atoms in the sample and the contrast in the images is still under debate.

With the aim of clarify this controversy, this work presents a theoretical analysis of the interaction between halogen-substituted benzene molecules (C_6Br_6 and C_6F_6) forming supramolecular assemblies on a silver [110] substrate. The relation between the tip-sample interaction and contrast in AFM/IETS images is also investigated, with the objective of understanding the origin of the sharp edges in the images.

The analyzed C_6Br_6 and C_6F_6 molecular clusters are found to interact with a combination of dispersive and electrostatic forces. Also the saddle points in the potential energy surfaces of the sample are demonstrated to be the source of the sharp edges in the AFM/IETS images, in accordance with previous works.[15,47] Then, to conclude this project, the origin of saddle points in the potential energy is discussed.

4.1 σ-hole and halogen bonding

Before we start the characterization of the interaction between halogen-benzene molecules, is worthy to introduce briefly the concept of σ-hole and halogen bond. A more detailed description of these can be found in the literature.[67] This concept will be necessary as well in chapter 5, where the direct visualization of the σ-hole is treated.

The concept of σ-hole was first introduced by Politzer et al.[68,69], Murray et al.[70,71] and Clark et al.[72] to explain the, until then counter-intuitive, attractive intermolecular interaction between halogen terminated molecules. Their work theorize that the electron density of an halogen atom bonded to a more electronegative atom, a carbon for example, is not uniformly distributed around the atom. The elements from the halogen column of the periodic table are characterized for having 5 p in the valence band. Then, because sp hybridization is negligible in halogen atoms, one of the p electrons will form the covalent bond with the other atom and the remaining 4 electrons will form a belt around the halogen atom. This particular configuration, as depicted in Figure 4.1a, leaves exposed the inner electrons of the halogen atom in the region opposite to the covalent atom, creating a positive crown surrounded by a negative belt (see Figure 4.1b). This exposed positive part is the so called σ-hole and its magnitude grows with the atomic number of the halogen atom, or in more precise words its magnitude enhances as the halogen atom is less electronegative.

An halogen bond is defined as the interaction between the σ-hole of an halogen atom and the negative belt of another halogen atom (see Figure 4.1c). This

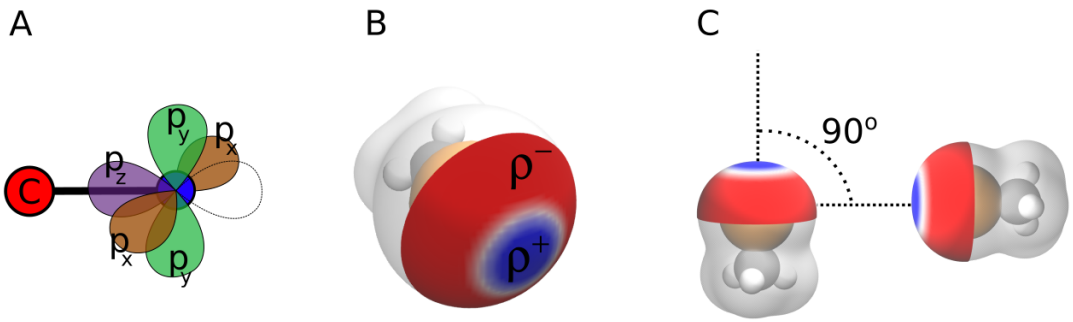

Figure 4.1: *Graphical definitions of σ-hole and halogen bond. (**A**) Scheme of the configuration of the 5 p valence orbitals of an halogen atom (in blue) when is covalently bonded to a more electronegative atom, for example a carbon (in red). (**B**) Hartree potential of a methyl bromide molecule (CH_3Br) projected on a isosurface of charge density to illustrate the concept of σ-hole (blue area labeled with ρ^+). (**C**) Scheme of an ideal halogen bond between two (CH_3Br) molecules. The positive area of the right molecule interacts with the negative belt of the left molecule with a perfect relative orientation of 90^o.*

interaction is attributed to be an interplay between electrostatic force and dispersion interaction. The role of the dispersion energy is enhanced by the anisotropic decrease of charge density known as polar flattering. This deflection of charge density in the area of the σ-hole in the halogen atom leads to a reduction of the Pauli interaction in this direction. This weakening of the Pauli repulsion allow the halogen atoms to get closer than the sum of their van der Waals radii, leading to stronger dispersion interactions.

4.2 Bond identification with SPM

In high-resolution SPM, the atomic structure of organic molecules is usually well reproduced by the sharp edges and bright spots observed in the images. Nevertheless, certain features in the contrast are usually observed in the areas between molecules, where the weak intermolecular interaction are predominant. The correct interpretation of these sharp edges in the SPM images in both inter- and intramolecular areas is only possible under a proper understanding of the physics that rule the imaging process.

At close tip-sample distances, the Pauli repulsion provokes the lateral relaxation of the probe[15] inducing sudden shifts in the recorded signal, providing submolecular spatial resolution. This is in concordance with the blunt images observed at far distances, where the weak interaction only cause negligible probe bending. In this context, the relation between a covalent bond and the contrast observed in the images is straightforward and widely accepted. The Pauli repulsion between the bond charge and the probe is the direct source of the observed contrast. On the other hand, the intermolecular sharp edges were sometimes understood as a direct consequence of non-covalent bonds,[73,74] while other authors[15,17,75] had reported sharp edges between unbounded atoms, leaving the discussion open.

4.3 Nature of binding in planar halogenbenzene assemblies and their possible visualization in scanning probe microscopy

With this work, we aim to contribute to the discussion about the SPM contrast and the weak intermolecular interactions. For this, we have analyzed the behaviour of C_6Br_6 and C_6F_6 molecules deposited on a silver [110] substrate. Then, using the probe particle (PP) model,[15] we examined the SPM imaging mechanism using a CO decorated tip.

In order to confirm the validity of the used model to describe the tip-sample interaction, we compared the theoretical results with the experimental results obtained by the group of Wilson Ho.[73]

4.3.1 Intermolecular interaction

We start the analysis of the intermolecular interactions looking at the electrostatic potential surfaces (EPS). We found that, while a significant σ-hole terminates the brominated molecule, the fluorine atoms in C_6F_6 are surrounded by an homogeneous distribution of negative charge. Then, we also analyzed the interaction energy between different configurations of two molecules for both the C_6F_6 and the C_6Br_6 compounds. Remarkably, we found the dispersion energy to be around three times larger than the electrostatic energy in the case of C_6Br_6. This diference is even larger in the case of C_6F_6, where the electrostatic interaction is an order of magnitude smaller than the dispersion energy. From the geometrical point of view, we found the halogen-halogen distances to be larger than twice the sum of their van der Waals radii. Also, the the angles between the atoms are far from the 90° expected from a ideal halogen bond (see Figure 4.1). Lately, analyzing the charge distribution between the molecules, we found no significant charge that could suggest covalent bonding between them.

Putting these arguments together, the interaction between C_6Br_6 molecules consist of an interplay between dispersive and electrostatic forces, while in the case of C_6F_6 is mostly dispersion interaction, with no role of charge transference in any case.

4.3.2 Origin of the SPM contrast

In the second part of this work, we simulated AFM and IETS images of the C_6Br_6 and C_6F_6 planar clusters. We carried out SPM simulations using the PP model[15,46] and we compared the results with the experimental work published by the group of Wilson Ho,[73] to confirm the validity of the model.

In the obtained AFM and IETS images, we observe several intermolecular features between the molecules in both C_6Br_6 and C_6F_6 molecular clusters, always in areas of large lateral relaxation of the flexible probe. The question is then, why the sharp edges appear in the intermolecular areas, or equivalently, what is the reason for this lateral probe deflection.

The absence of charge accumulation, due to covalent bonding, between the halogens discards the possibility of a Pauli repulsion between the tip and the

bond charge. We have also ruled out the implication of the electrostatic interaction between the tip and the σ-hole. For this, we have repeated the calculation neglecting the electrostatic tip-sample interaction, obtaining similar results.

We found the sharp edges to appear in saddle points of the potential energy surface of the sample, where the tip suddenly slide laterally to minimize its energy, causing sharp shifts in the recorded signal. This is in concordance with the results of Pavliček et al.[47] where they found similar features between atoms without any expected direct bond between them. Hence, we concluded that the origin of the sharp edges is just the mere presence of the halogen atoms close to each other. This is exemplified in Figure 4.2, where the CO molecule that terminates the tip slides laterally over the saddle point.

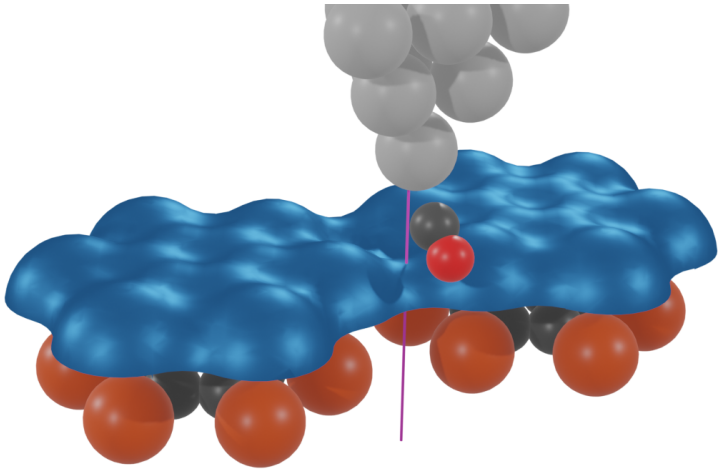

Figure 4.2: *Schematic view of the probe relaxation over a saddle point in the potential surface of the a C_6Br_6 dimer.*

As a summary of all the conclusions of this work, the main differences between covalent and non-covalent bonds and their SPM imaging mechanism should be remarked.

A covalent bond consist in the re-hybridization of the electronic states of the implicated atoms, creating a charge localization along the line that connects both atoms. The Pauli repulsion between the electrons of the tip and the bond charge creates a saddle point in the energy surface where the flexible probe will bend laterally and give rise to sharp edges. So in this case the relation between the localized charge that forms the bond and the narrow feature observed in the images is straightforward.

In the case of non-covalent interactions the saddle points in the potential energy are a consequence of the mere presence of two atoms very close to each other and not of the interactions between them. Also, the dispersion and electrostatic interactions have a non-local character that is difficult to relate with a directional observation such a sharp edge in the SPM contrast.

Hence, we consider that the covalent bonds can be directly visualized, because the signal recorded arises from the direct interaction between the tip and the charge that forms the bond. On the other hand, non-local bonds could not be related with a narrow feature on the recorded images and hence, these should not be identified as visualization of weak non-covalent bonds.

5. KPFM probe particle model

5.1 Introduction

The Kelvin probe force microscopy (KPFM) technique was introduced earlier in chapter 1 as an SPM technique capable to measure the relative work function of metallic surfaces. The section 1.3 describes the theoretical foundation of the tip-sample interaction in a KPFM experiment at macroscopic distances. The maximal point (V_{CPD}) of the parabola described by the frequency shift vs the external bias ($\Delta f(V)$) is determined by the difference between the work function of the tip and sample (Φ_t and Φ_s). However, at close tip-sample distances, an additional interaction mechanism enters in play, giving rise to local changes in the value of the contact potential difference (V_{CPD}). These local changes in the $\Delta f(V)$ parabola can be recorded across the sample, obtaining KPFM images mapping the values of V_{CPD}.

The spatial resolution down to atomic scale with KPFM at close distances has been repeatedly achieved experimentally,[76–78] but its theoretical background is still being understood. The work function is a macroscopic characteristic of the surfaces, and should be hence independent of the tip-sample relative position. Consequently, the molecular resolution accomplish experimentally at close distances should have a different source.

This chapter details the model developed by the author of this thesis to computationally simulate KPFM experiments. This model is based on the electrostatic interaction between localized charges and bias-induced dipoles in the tip-sample junction. Then, we present a combined effort of experiments and computational simulations to obtain direct KPFM images of the σ-hole of halogenated molecules absorbed on a metallic substrate.

5.2 Theoretical background of the KPFM probe particle model

This section explains the interaction forces that arise when the tip is brought close to the sample and a potential difference is applied between them. Then, the relation between the KPFM forces (F_{KPFM}) and the frequency shift (Δf) is described as a function of the external bias (V).

5.2.1 Description of the tip-sample interaction force

First, we separate the bias dependent forces in two terms, the short range (SR) and long range (LR) terms:

$$F_{KPFM} = F^{SR}_{KPFM}(V, \vec{r}_{tip}) + F^{LR}_{KPFM}(V, z_{tip}), \tag{5.1}$$

where both terms depends on the external bias V. We should note here that, while the microscopic term $F_{SR}(V, \vec{r}_{tip})$ depends on the tip-sample relative position $\vec{r}_{tip}$, the macroscopic term $F_{LR}(V, z_{tip})$ depends only on the tip-sample vertical distance z_{tip}.

In the simplest approximation, we could describe the LR interaction term as the force that acts between the plates of a capacitor:

$$F_{KPFM}^{LR}(V, z_{tip}) = \frac{1}{2}\frac{\partial C\left(z_{tip}\right)}{\partial z_{tip}}\left(V - V_{CPD}\right)^2, \tag{5.2}$$

where $C\left(z_{tip}\right)$ is the capacitance of the tip-sample junction and V_{CPD} is the contact potential difference:

$$V_{CPD} = \Phi_t - \Phi_s, \tag{5.3}$$

where Φ_t and Φ_s are the work functions of the tip and sample respectively. The F_{LR} force is always attractive, and gives the $\Delta f(V)$ parabola, its characteristic quadratic dependence, as depicted in Figure 1.6.

At close tip-sample distances, the electrostatic interactions between the probe apex and the atoms of the sample immediately below the tip intensifies. This interaction can be described using the Coulomb's interaction between the net charges of tip (ρ_t) and sample (ρ_s), under the applied external potential V:

$$F_{El}(\vec{r}, V) = \int\int \frac{\rho_t(\vec{r}, V)\rho_s(\vec{r}\,', V)}{|\vec{r} + \vec{r}_{tip} - \vec{r}\,'|^2} d\vec{r}\, d\vec{r}\,', \tag{5.4}$$

where $\vec{r}_{tip}$ is the relative position of the tip with respect to the sample and where $\vec{r}$ and $\vec{r}\,'$ are tridimensional integration variables. To understand the implications of considering the tip and sample under the external applied bias it is illustrative to separate their charge densities in two terms:

$$\rho_{t/s}(\vec{r}, V) = \rho_{t/s}^0(\vec{r}) + \delta\rho_{t/s}(\vec{r}, V), \tag{5.5}$$

where $\rho_{t/s}^0(\vec{r})$ is the intrinsic net charge, i.e. the charge in the absence of external potential and $\delta\rho_{t/s}(\vec{r}, V)$ is the polarization induced by the electric field created by the external bias voltage. We should note here that our model considers only the polarization due to the electric field induced by the applied bias. This means that for example, polarizations induced in the tip or the sample by the presence of each other are neglected. Using the charge density description from equation 5.5 in the equation 5.4, the $F_{El}(\vec{r}, V)$ separates in four terms:

$$\begin{aligned} F_{El}(\vec{r}, V) = &\int\int \frac{\rho_t^0(\vec{r})\rho_s^0(\vec{r}\,')}{|\vec{r} + \vec{r}_{tip} - \vec{r}\,'|^2} + \int\int \frac{\delta\rho_t(\vec{r}, V)\rho_s^0(\vec{r}\,')}{|\vec{r} + \vec{r}_{tip} - \vec{r}\,'|^2} \\ &+ \int\int \frac{\rho_t^0(\vec{r})\delta\rho_s(\vec{r}\,', V)}{|\vec{r} + \vec{r}_{tip} - \vec{r}\,'|^2} + \int\int \frac{\delta\rho_t(\vec{r}, V)\delta\rho_s(\vec{r}\,', V)}{|\vec{r} + \vec{r}_{tip} - \vec{r}\,'|^2}. \end{aligned} \tag{5.6}$$

The first term in the right-hand side of equation 5.6 is the interaction between the intrinsic charges of tip and sample, this will be the only term of the electrostatic interaction for $V = 0$. The second term describes the interaction between the intrinsic charges of the sample $\rho_s^0(\vec{r}\,')$ and the dipoles induced in the tip by the bias $\delta\rho_t(\vec{r}, V)$. Similarly, the third term accounts for the interaction between the intrinsic charges of the tip $\rho_t^0(\vec{r})$ and the dipoles induced in the sample by the external bias $\delta\rho_s(\vec{r}\,', V)$. The fourth and last term is the interaction between the dipoles induced by the external bias in both the tip ($\delta\rho_t(\vec{r}, V)$) and sample ($\delta\rho_s(\vec{r}\,', V)$). In the proposed model, we will suppose the polarizations ($\delta\rho$) to be

much smaller than the intrinsic charges (ρ_0), so this last term is neglected in the further discussion.

To analyze the bias dependence of the $F_{El}(\vec{r}, V)$, we should note that the first term is independent of the external potential and will not affect the bias dependence of the $\Delta f(V)$ parabola. Then, as the last term was neglected, the bias-dependent, short range interaction between the tip and sample will be described by the two remaining terms:

$$F^{SR}_{KPFM}(\vec{r}, V) = \int\int \frac{\delta\rho_t(\vec{r}, V)\rho^0_s(\vec{r}\,')}{|\vec{r} + \vec{r}_{tip} - \vec{r}\,'|^2} + \int\int \frac{\rho^0_t(\vec{r})\delta\rho_s(\vec{r}\,', V)}{|\vec{r} + \vec{r}_{tip} - \vec{r}\,'|^2}, \tag{5.7}$$

where we will suppose the polarizability of tip and sample constant within the range of induced electric fields. Hence, the induced dipoles ($\delta\rho$) and consequently F^{SR}_{KPFM} will depend linearly with the external bias that induce the electric field.

The two terms in equation 5.7 will affect the $\Delta f(V)$ parabola, changing the position of its maximal point. Since the values of V_{CPD} at close tip-sample distances will depend on the tip-sample relative position ($\vec{r}_{tip}$), the more adequate notation V_{LCPD} will be used, where LCPD stands for local contact potential difference.

5.2.2 Effect of the short range KPFM forces in the frequency shift

To visualize the effect of F^{SR}_{KPFM} in the frequency shift Δf, their relation can be expressed in a rather approximated but intuitive way:[79]

$$\Delta f(V) \simeq -\frac{f_0}{2k}\frac{\partial}{\partial z}F^{SR}_{KPFM}(\vec{r}, V), \tag{5.8}$$

where f_0 and k are the eigen-frequency of oscillation and the stiffness of the cantilever. To illustrate the correspondence between the interaction force and the frequency shift, lets apply, as an example, the relation in equation 5.8 to the repulsive and attractive components of a Lennard-Jones (LJ) potential:

- A repulsive force such as F^{LJ}_{Pauli}:

$$F^{LJ}_{Pauli} \propto \frac{1}{z^{13}} \Rightarrow \frac{\partial}{\partial z}F^{LJ}_{Pauli} \propto -\frac{1}{z^{14}} \Rightarrow \Delta f \propto \frac{1}{z^{14}} > 0 \tag{5.9}$$

  will cause a positive shift in the frequency.

- An atractive force such as $F^{LJ}_{Disp.}$:

$$F^{LJ}_{Disp.} \propto -\frac{1}{z^{7}} \Rightarrow \frac{\partial}{\partial z}F^{LJ}_{Disp.} \propto \frac{1}{z^{8}} \Rightarrow \Delta f \propto -\frac{1}{z^{8}} < 0 \tag{5.10}$$

  will cause a negative shift in the frequency.

Then according to equation 5.8, repulsive interactions will result in positive shifts of the frequency Δf and attractive interactions in negative shifts of the frequency Δf, as schematized in Figure 5.1A.

Because the signs of $\delta\rho_t$ and $\delta\rho_s$ are determined by the sign of the applied bias V, the two components of F^{SR}_{KPFM} could be either attractive for $V < 0$ and

repulsive for $V > 0$ or vice versa. Consequently, observing the scheme in Figure 5.1B, we obtain our first rule of thumb to relate the interaction force and the frequency shift:

- The interactions that get more repulsive with bias will shift V_{LCPD} to the right (towards positive values).
- The interactions that get more attractive with bias will shift V_{LCPD} to the left (towards negative values).

Because the sign of the induced dipole ($\delta\rho$) is considered independent of the tip relative position $\vec{r}_{tip}$,the spatial dependence of $\Delta f(V)$ should be determined by the sign of the intrinsic charges of tip and sample (ρ_t^0 and ρ_s^0).

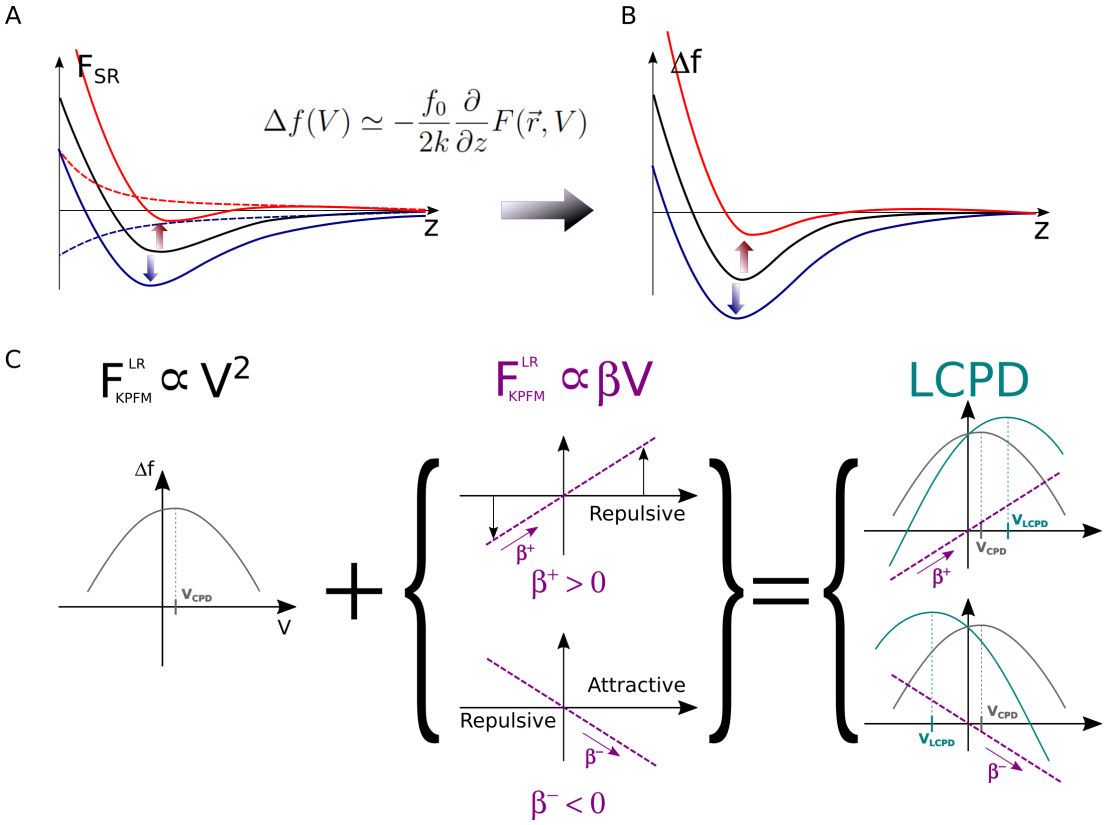

Figure 5.1: *Scheme of the correspondence between tip-sample interaction forces and the frequency shift induced in the tip. The attractive and repulsive additional electrostatic forces (dashed blue and red lines respectively) in the left plot in panel (**A**) will shift the force profile (black solid line) to the blue and red solid lines respectively. According to equation 5.8 these changes in the total interaction force will switch the frequency shift spectroscopy towards lower or higher values respectively (right plot in panel **A**). (**B**) The characteristic linear dependence of the additional electrostatic forces with the external potential (violet dashed line in the central plot in panel **B**) will induce shifts on the long range $\Delta f(V)$ parabola (left plot in panel **B**). These shifts will be towards the right (if the repulsive character of the force increases with bias) or to the left (in the case of increasingly attractive forces). The combination of F^{SR}_{KPFM} and F^{LR}_{KPFM} give rise to the $\Delta f(V)$ parabolas depicted in cyan, which maximal is at V_{LCPD}.*

Then, we should now apply this rule to the two terms of F^{SR}_{KPFM} for the case of positive and negative intrinsic charges on the tip and the sample (ρ^0_t and ρ^0_s) and observe their effect in the V_{LCPD}. For this it will be useful to first set the sign of the induced dipoles on tip ($\delta\rho_t$) and sample ($\delta\rho_s$) for a positive and negative applied bias (V).

The most common wiring of a KPFM experimental system is with the ground set on the tip, so the external bias is applied to the sample. This means that the electric field in the junction points towards the sample for $V < 0$ and towards the tip for $V > 0$. Then, a dipole created on the tip will orient with the positive part towards the sample for negative bias and with the negative part for positive bias, as it is schematized in Figure 5.2. Under the same logic, a dipole created on the sample by a negative external bias will align with its negative part towards the tip and with its positive part for the case of positive external bias.

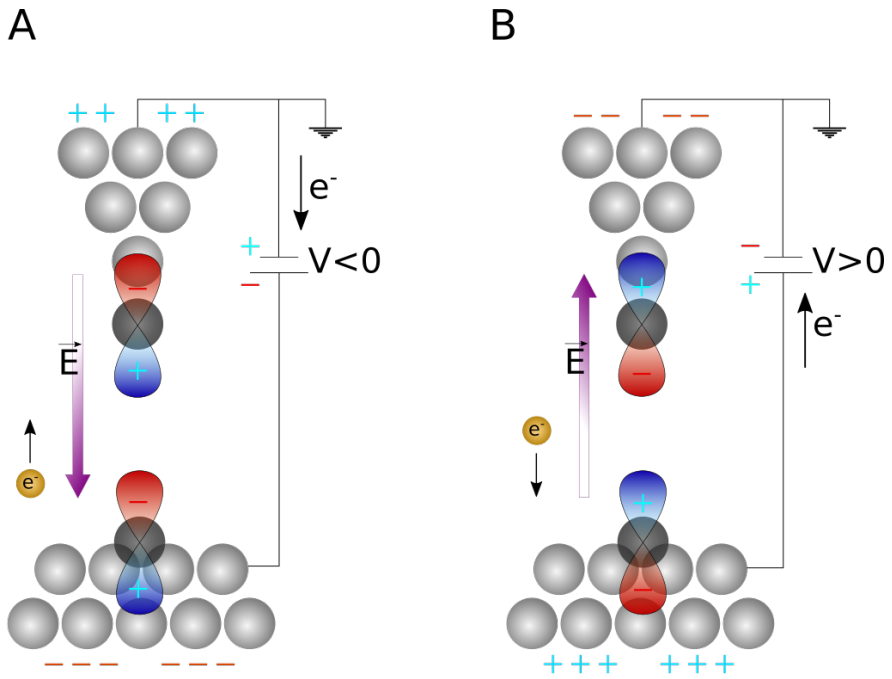

Figure 5.2: *Scheme of the dipoles induced in the tip-sample junction by an external potential in the case of (**A**) negative bias and (**B**) positive bias for the case of a KPFM system with the ground set on the tip.*

Now that the sign of the induced dipoles is established, we can analyze the behaviour of the two terms of F^{SR}_{KPFM} (equation 5.7) for both positive and negative intrinsic charges. Lets start the analysis with the 1^{st} term of equation 5.7, where the dipoles induced in the tip ($\delta\rho_t$) interacts with the intrinsic charges of the sample (ρ^0_s).

First term: $\delta\rho_t \cdot \rho^0_s$

The case of a positive intrinsic charge in the sample interacting with a dipole induced in the tip ($\delta\rho_t$) is schematized in the Figure 5.3. The positive part of the dipole is repelled by the sample for $V < 0$ and attracted for $V > 0$. In this case, according to the rule of thumb extracted from Figure 5.1, this term will shift the V_{LCPD} towards negative values.

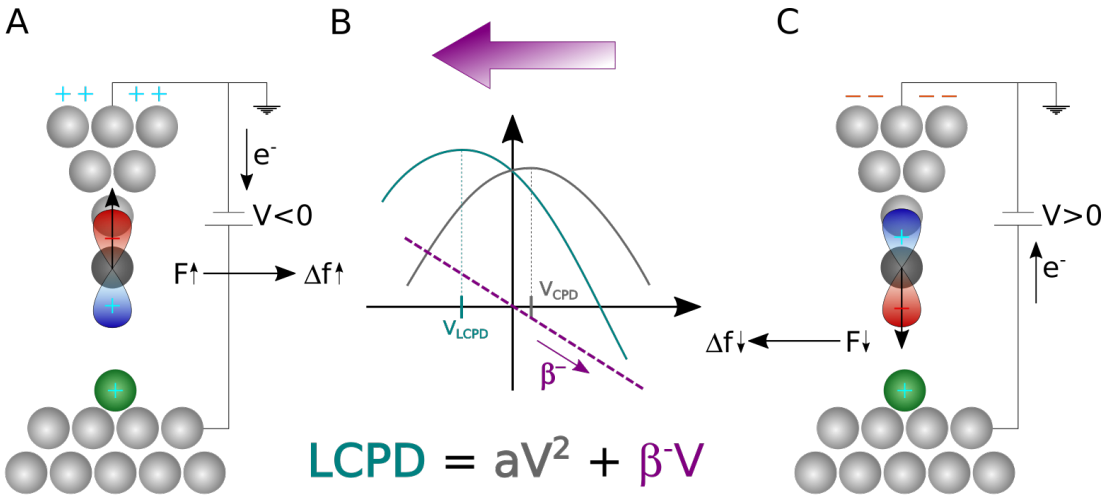

Figure 5.3: *Scheme of the V_{LCPD} shift induced by the first term of equation 5.7, due to the interaction between a dipole induced in the tip and an intrinsic positive charge in the sample. The interaction force results repulsive for $V < 0$ and attractive for $V > 0$, provoking a shift of the LCPD parabola to the left.*

Similarly, for the case of a negative intrinsic charge in the sample interacting with the same dipole induced in the tip ($\delta\rho_t$), the positive part of the dipole is attracted by the sample for $V < 0$ and repelled for $V > 0$. Hence, under the same logic, this configuration will induce a shift of the V_{LCPD} towards positive values, as schematized in Figure 5.4.

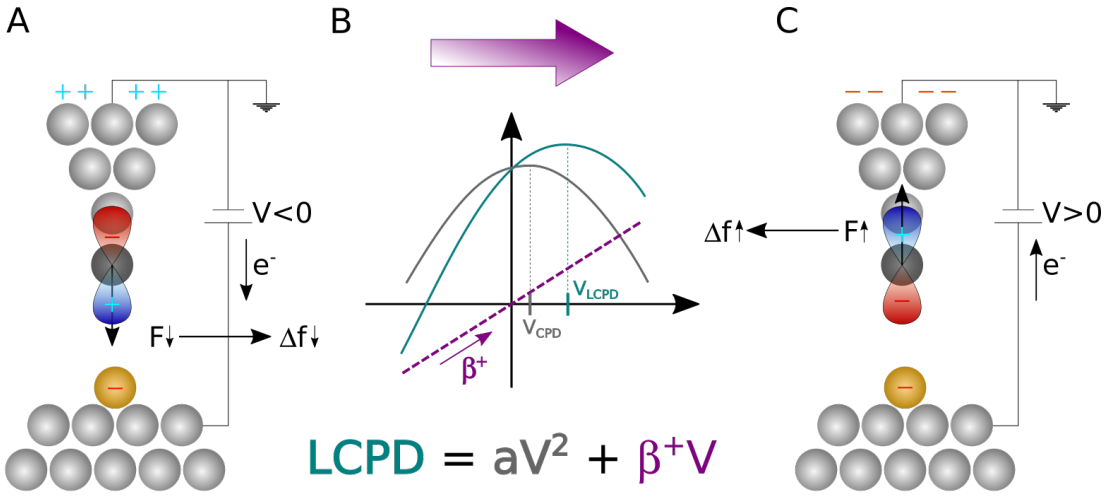

Figure 5.4: *Scheme of the V_{LCPD} shift induced by the first term of equation 5.7, due to the interaction between a dipole induced in the tip and an intrinsic negative charge in the sample. The interaction force results attractive for $V < 0$ and repulsive for $V > 0$, provoking a shift of the LCPD parabola to the right.*

The analysis of these two cases (Figures 5.3 and 5.4) indicate that the 1^{st} term of the equation 5.7 shifts the $\Delta f(V)$ parabola to the left for positive charges in the sample and to the right for negative charges in the sample. This behaviour is in accordance with the experimental results of previous works.[76–78,80]

Second term: $\rho_t^0 \cdot \delta\rho_s$

Lets now analyze the 2^{nd} term of the equation 5.7 in the same way. For the case of a positive net charge in the apex of the tip, the tip-sample interaction will be attractive for $V < 0$ and repulsive for $V > 0$. This, using again the scheme in Figure 5.1, will shift the value of V_{LCPD} towards positive values, as schematized in Figure 5.5.

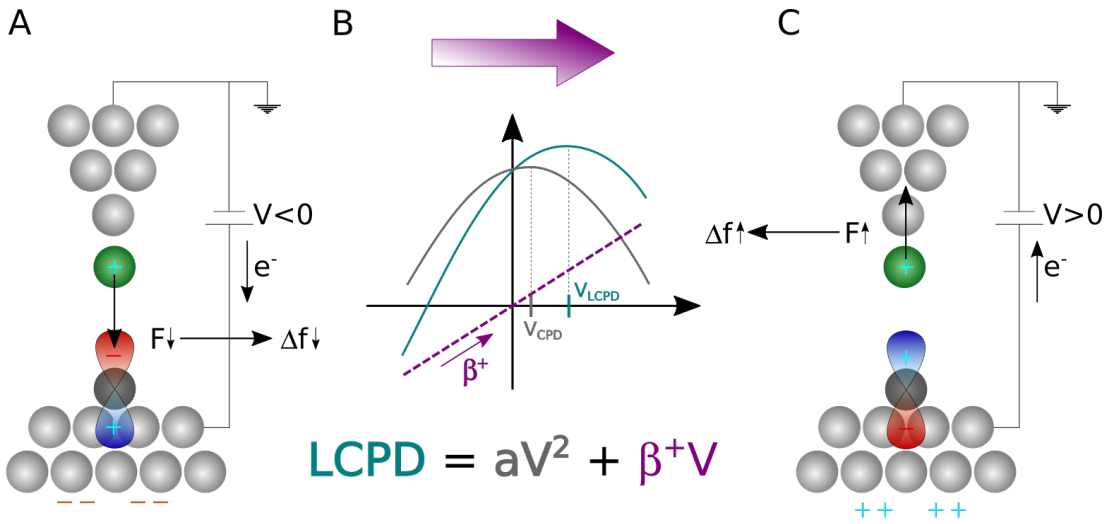

Figure 5.5: *Scheme of the V_{LCPD} shift induced by the second term of equation 5.7, due to the interaction between a dipole induced in the sample and an intrinsic positive charge in the tip. The interaction force results attractive for $V < 0$ and repulsive for $V > 0$, provoking a shift of the LCPD parabola to the right.*

Similarly for a negative net charge in the apex of the tip, the negative part of $\delta\rho_s$ will repel the tip for $V < 0$, while the dipole with positive topmost part in the sample will attract the tip for $V > 0$. This situation, that will shift the value of V_{LCPD} towards negative values, is depicted in Figure 5.6.

Then, the sign analysis of the 2^{nd} term of the equation 5.7 done in Figures 5.5 and 5.6 indicates that the presence of positive/negative charges in the tip will shift the LCPD parabola to the right/left, respectively.

Complete F_{KPFM}^{SR} interaction: $\delta\rho_t \cdot \rho_s^0 + \rho_t^0 \cdot \delta\rho_s$

Gathering the conclusions of this discussion about the effect of F_{KPFM}^{SR} in the values of V_{LCPD} two different tendencies are observed:

- Positive charges in the sample will be observed as lower values of V_{LCPD} and negative charges as higher values of V_{LCPD}.
- Positive charges in the tip will be observed as higher values of V_{LCPD} and negative charges as lower values of V_{LCPD}.

Hence the final value of V_{LCPD} observed experimentally will be an interplay between a term depending on the net charges of the sample and a term depending on the net charges of the tip. This means that the experimental images will be a combination of an image of the tip and an image of the sample, weighed by the

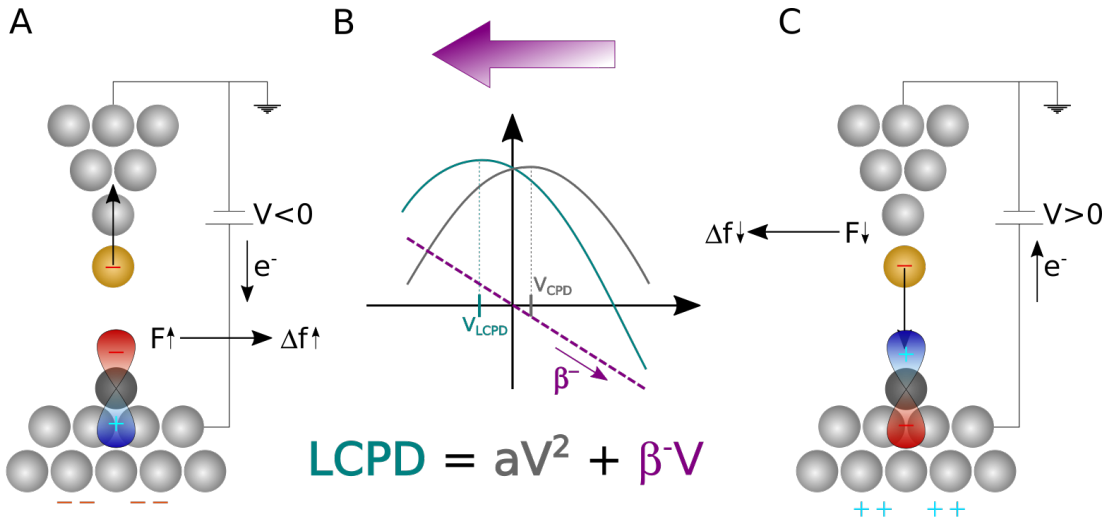

Figure 5.6: *Scheme of the V_{LCPD} shift induced by the second term of equation 5.7, due to the interaction between a dipole induced in the sample and an intrinsic negative charge in the tip. The interaction force results repulsive for $V < 0$ and attractive for $V > 0$, provoking a shift of the LCPD parabola to the left.*

polarizations of the sample and tip respectively. Ideally, to maximize the presence of an image that resembles the sample in the experimental results, one should try to maximize the polarizability of the probe. To facilitate the interpretation of the experimental results, the different contributions to V_{LCPD} that can arise from the two considered terms of F^{SR}_{KPFM} are summarized in Figure 5.7.

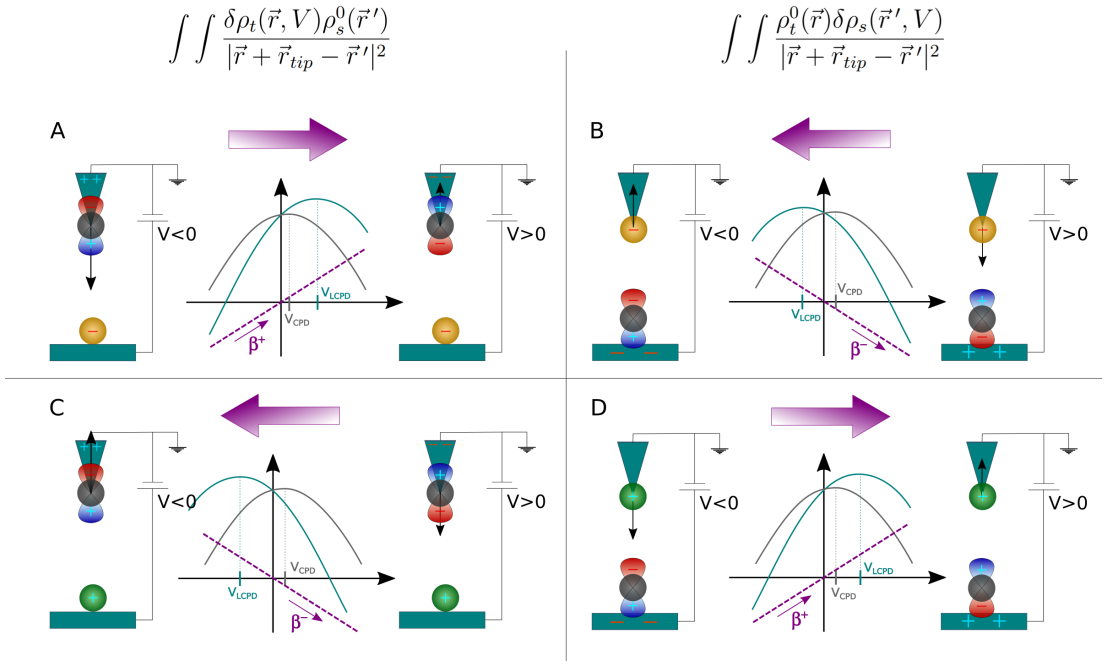

Figure 5.7: *summary of the relations between localized charges and the changes in V_{LCPD} explained in Figures 5.3 - 5.6.*

As, the two mentioned contributions are impossible to separate experimentally, the KPFM results should be analyzed with extreme caution. Our intention

with this model is to provide a computational environment in which both contributions can be separated. This allows to analyze each contribution independently, to relate each aspect of the experimental results with its true origin. This analysis procedure is exemplified in section 5.3 where we present the direct imaging of σ-holes in halogenated molecules using KPFM experiments. There, we combine experiments with simulations using the proposed model to help us distinguish between images of the tip and images of the sample.

5.2.3 Technical details of the implementation

The procedure to evaluate the F_{KPFM} force was implemented in the probe particle (PP) model package[15] by the author of the present thesis. First, lets analyze the basic AFM simulation strategy used in the PP model.

In the original version of the PP model, the interaction between the probe and the sample is calculated by means of a Lennard-Jones force field:

$$F_{LJ}(\vec{r}_{tip}) = \sum_{\alpha}\sum_{\beta}\vec{r}_{tip}\left(12\frac{B_{\alpha\beta}}{|\vec{r}_{tip}|^{14}} - 6\frac{A_{\alpha\beta}}{|\vec{r}_{tip}|^{8}}\right), \tag{5.11}$$

where α and β sums over the atoms of tip and sample respectively, and where $\vec{r}_{tip}$ is the tip-sample relative position. $A_{\alpha\beta}$ and $B_{\alpha\beta}$ are interaction coefficients for each α and β pair of atoms, which precise definition can be found in the original publication of the PP model.[15] Additionally, the electrostatic interaction can be included with the following expression:[46]

$$F_{El}(\vec{r}_{tip}) = \frac{\partial}{\partial\vec{r}_{tip}}\int \rho_t(\vec{r})V_s^h(\vec{r}-\vec{r}_{tip})d\vec{r}, \tag{5.12}$$

where V_s^h is the Hartree potential of the sample. Expressing the Coulomb interaction in this form allows to calculate the electrostatic interaction as a convolution of $\rho_t(\vec{r})$ and $V_s^h(\vec{r}-\vec{r}_{tip})$. Then the position of the flexible probe is relaxed under the interaction force and the frequency shift is calculated using the method proposed by Giessibl.[36]

We start the implementation of KPFM adding the bias dependent forces (F_{KPFM}) to the total forces (F_{LJ} and F_{El} in equations 5.11 and 5.12) for a range of values of applied external bias (V) . The macroscopic term F_{KPFM}^{LR} is included as the force that acts between an sphere of radius R_{tip} and an infinite plane at distance z_{tip}, both conductors, under an external potential:[81]

$$F_{KPFM}^{LR}(V, z_{tip}) = \pi\varepsilon_0\left[\frac{R_{tip}^2}{z_{tip}\left(z_{tip}+R_{tip}\right)}\right]\left(V - V_{CPD}\right)^2. \tag{5.13}$$

The parameter V_{CPD} can be set to the experimental value at large distance and the radius of the tip's apex (R_{tip}) can be chosen, within the range of a few tens of nanometers, to reflect the sharpness of the macroscopic tip in the experiment.

Then, we calculate the interaction between static charges and polarizations (F_{KPFM}^{SR}), in the presence of an electric field E_z, with the following expression:

$$F^{SR}_{KPFM}(\vec{r}_{tip}, E_z) = \frac{\partial}{\partial \vec{r}_{tip}} \int \delta\rho^0_t(\vec{r}, E_z) V^h_s(\vec{r} - \vec{r}_{tip})\, d\vec{r} + \frac{\partial}{\partial \vec{r}_{tip}} \int \rho_t(\vec{r}) \delta V^h_s(\vec{r} - \vec{r}_{tip}, E_z)\, d\vec{r}, \tag{5.14}$$

where we use the Hartree potential of the sample V^h_s and the potential created by the polarization of the sample (δV^h_s).

To calculate the polarizations of tip $\delta\rho_t(\vec{r}, E_z)$ and sample $\delta V_h(\vec{r} - \vec{r}_{tip}, E_z)$, we consider the polarizabilities ($\alpha(r)$) of tip and sample to be constant within the magnitude range of the induced field. Hence, the polarization of the tip at any given electric field $\delta\rho_t(\vec{r}, E_z)$ can be extrapolated from the value of polarization under a given reference electric field ($E_{ref.}$):

$$\delta\rho_t(\vec{r}, E_z) = \alpha(\vec{r}) \cdot E_z = \frac{E_z}{E_{ref}}\, \delta\rho_t(\vec{r}, E_{ref}), \tag{5.15}$$

and similarly for the Hartree potential of the polarizations induced in the sample we asume:

$$\delta V^h_t(\vec{r} - \vec{r}_{tip}, E_z) = \frac{E_z}{E_{ref}}\, \delta V^h_t(\vec{r} - \vec{r}_{tip}, E_{ref.}). \tag{5.16}$$

Hence, the interaction force F^{SR}_{KPFM} could be extrapolated from the values of the force calculated for the reference electric field E_{ref}:

$$F^{SR}_{KPFM}(\vec{r}_{tip}, E_z) = \frac{E_z}{E_{ref}} \cdot F^{SR}_{KPFM}(\vec{r}_{tip}, E_{ref.}). \tag{5.17}$$

At last, we consider the electric field between the tip and the sample to be approximately the one between the parallel plates of a capacitor:

$$E_z = \frac{V}{z_{tip}} \tag{5.18}$$

Consequently, the $F^{SR}_{KPFM}(\vec{r}_{tip}, V)$ interaction force for an applied bias V, when the metallic part of the tip and the substrate are at a vertical distance z_{tip}, can be extrapolated from the values of the force under the reference electric field $E_{ref.}$:

$$F^{SR}_{KPFM}(\vec{r}_{tip}, V) = \frac{V}{E_{ref} \cdot z_{tip}} \cdot F^{SR}_{KPFM}(\vec{r}_{tip}, E_{ref.}). \tag{5.19}$$

Then, F^{LR}_{KPFM} and F^{SR}_{KPFM} are added to the bias independent forces (equations 5.11 and 5.12) for the chosen set of applied bias. Subsequently, the frequency shift maps ($\Delta f(\vec{r}_{tip})$) are obtained at every chosen value of V, obtaining the dependence of the frequency shift with the bias ($\Delta f(V, \vec{r}_{tip})$) Then, for a precise determination of the values of V_{LCPD} at each point ($\vec{r}_{tip}$), the $\Delta f(V, \vec{r}_{tip})$ data is fitted with the equation:

$$\Delta f(V, \vec{r}_{tip}) = \alpha(\vec{r}_{tip}) \cdot V^2 + \beta(\vec{r}_{tip}) \cdot V + \gamma(\vec{r}_{tip}), \tag{5.20}$$

and the V_{LCPD} is determined at each point:

$$V_{LCPD}(\vec{r}_{tip}) = -\frac{\beta(\vec{r}_{tip})}{2\alpha(\vec{r}_{tip})} \tag{5.21}$$

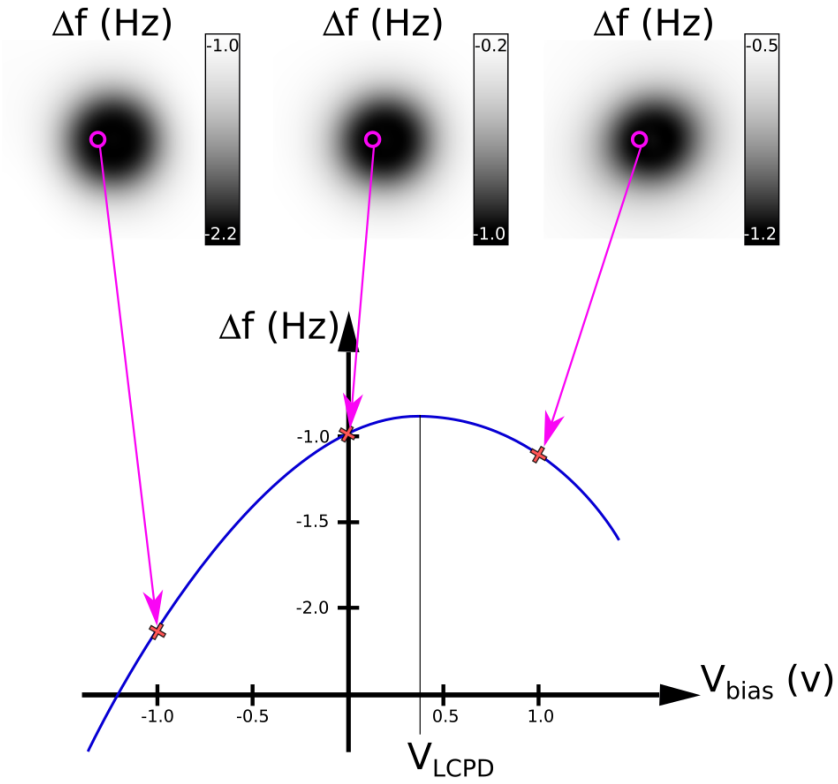

Figure 5.8: *Scheme of the* $(\Delta f(V, \vec{r}_{tip}))$ *fitting process. First the frequency shift maps are calculated for every value of the applied bias. Then, for each point of the maps, the values are extracted and fitted with the equation 5.20.*

This analysis and fitting process is schematized in Figure 5.8.

The reference polarizations $\delta\rho_t(\vec{r}, E_{ref})$ and $\delta V_h(\vec{r} - \vec{r}_{tip}, E_{ref.})$ used in the calculation are defined as:

$$\delta\rho(\vec{r}, E_{ref.}) = \rho(\vec{r}, E_{ref}) - \rho^0(\vec{r}), \tag{5.22}$$

$$\delta V_h(\vec{r}, E_{ref.}) = V_h(\vec{r}, E_{ref.}) - V_h^0(\vec{r}), \tag{5.23}$$

where $\rho(\vec{r}, E_{ref})$ and $V_h(\vec{r}, E_{ref.})$ are the charge density and Hartree potential of tip and sample under the chosen reference electric field $E_{ref.}$ and $\rho^0(\vec{r})$ and $V_h^0(\vec{r})$ are the charge density and Hartree potential of tip and sample in the absence of any external field.

The four terms in the right hand side of equations 5.22 and 5.23 can be calculated for example by means of density functional theory (DFT). The implemented code also allows to generate ρ^0_{tip} and $\delta\rho_{tip}$ analytically, using atomic orbitals (s, p_z, dz^2, ...) fitted to DFT results. In the case of DFT obtained electronic structure, both with and without external field calculations should be performed with the same fixed structure, to avoid changes in the electronic structure caused by the structural relaxation due to the external field. Also, in the case of calculating the electronic structure of the tip with DFT, the reader should keep in mind that while the equations are written in terms of the net charges of the tip ρ^0, many codes usually provide the electronic charge density, excluding the charge of the

atom's core. The net charges are then calculated as the total electronic charge of the tip $\rho_t^{elec.}$, minus the atomic charge of all the atoms that form the tip ρ_{atm} :

$$\rho_t^0(\vec{r}) = \rho_t^{elec.}(\vec{r}) - \rho_{atm}(\vec{r}). \tag{5.24}$$

5.3 KPFM identification of anisotropic charge distributions at atomic scale

The contrast in KPFM images originates from a certain part of the electrostatic force that depends on the applied bias. Studying the frequency shift dependence with the external potential allows to separate the electrostatic interaction from stronger contributions like the Pauli repulsion or the dispersion interaction. This mechanism of operation makes KPFM the ideal technique for the detection of anisotropic distributions of charge such as the σ-hole.

A σ-hole is the anisotropic charge distribution that certain halogen atoms present when they are covalently bonded to another atom with stronger electronegativity. Section 4.1 explains that the way the p valence electrons organize themselves around the halogen atom makes it exhibit a positive crown surrounded by a belt of negative potential. The existence of σ-holes in halogen atoms has only been demonstrated indirectly, observing the interaction between halogenated molecules or predicted by theoretical calculations.

Using a KPFM experimental set-up with different tip functionalizations we obtained direct images of the σ-hole on the halogen atoms of selected molecules.[82] We were also able to determine the shape and sign of the multipolar charge in the apex of a CO decorated tip. We used the proposed method to chose the tip functionalization that permits the visualization of the σ-hole, avoiding spurious effects.

To achieve our objective, we have deliberately chosen two molecules, the tetrakis(4-fluorophenyl)methane (4FPhM) and tetrakis(4-bromophenyl)methane (4BrPhM). These compounds, as it is shown in Figure 5.9, present a tripodal structure after their absorption on a silver [111] substrate. This configuration, with one of the halogen atoms pointing out of the surface allows to easily access the area where the σ-hole is supposed to be found.

We have chosen the F and Br terminations for the molecules among the halogen column, so we will have one molecule exhibiting a σ-hole and one terminated with an homogeneous charge distribution for comparison. This can be seen in the electrostatic potential surfaces (EPS) of the two selected molecules in Figure 5.10. The KPFM experiments where performed using two different tip functionalizations with distinct electrostatic character (see Figure 5.10C and D). First we choose a Xe terminated tip to experimentally obtain the images of the σ-hole in the 4BrPhM molecule. The homogeneous charge and high polarizability of this tip termination make it a great candidate for the imaging of anisotropic charge distributions in the sample. Secondly, because it is a commonly used tip termination in SPM, we performed as well KPFM experiments using a CO terminated tip. The results obtained using the CO decorated tip allowed us to experimentally confirm the electrostatic character of a CO terminated metallic tip.

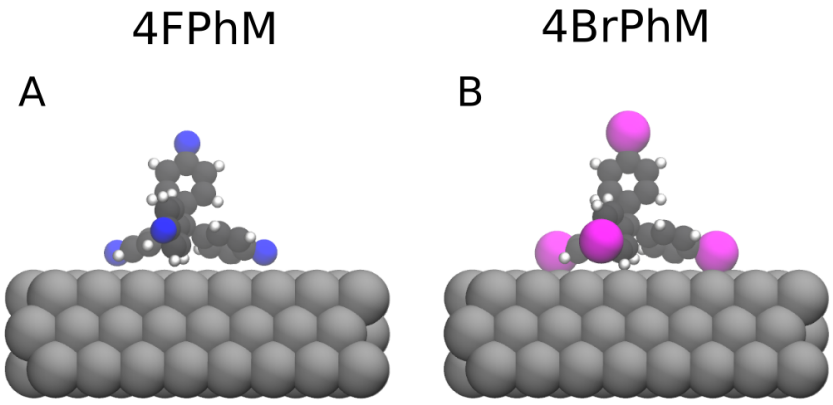

Figure 5.9: *Relaxed structure of (**A**) tetrakis(4-fluorophenyl) methane (4FPhM) and (**B**) tetrakis(4-bromophenyl) methane (4BrPhM) molecules absorbed in a silver [111] substrate. The different elements are depicted as follows: Silver in gray, carbon in black, hydrogen in white, bromine in magenta and fluorine in blue.*

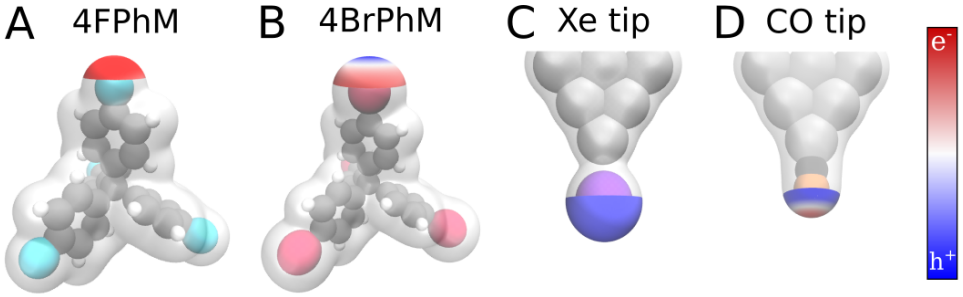

Figure 5.10: *Electrostatic potential surfaces (EPS) of the (**A**) tetrakis(4-fluorophenyl) methane (4FPhM) and (**B**) tetrakis(4-bromophenyl) methane (4BrPhM) gas phase molecules and the two tip decorations, (**C**) Xe and (**D**) CO. The used charge density isosurface is 0.001 a_0^{-3} and the values of Hartree potential that set the color scale are [-0.5, 0.5] eV for 4FPhM, [-0.8, 0.6] eV for 4BrPhM, [-0.3, 0.3] eV for the Xe decorated tip and [-0.3, 0.3] eV for the CO decorated tip.*

5.3.1 Xe terminated tip experiments and the σ-hole visualization.

The Figure 5.11 shows KPFM experimental images (panels A-B) of 4FPhM and 4BrPhM obtained with a Xe decorated tip and the corresponding simulated images (C-D). In the case of 4BrPhM we obtained a blue dot surrounded by a red belt, result that can be intuitively identified as the observation of a σ-hole (Figure 5.11B,D). On the other hand, the images of the 4FPhM molecule show an homogeneous distribution of positive contrast (Figure 5.11A,C). In both cases, the obtained images are coherent with the electrostatic potential showed in Figure 5.10. Nevertheless, it is illustrative to analyze to origin of the observed contrast and confirm that we obtained images of the atomic charges on the foremost

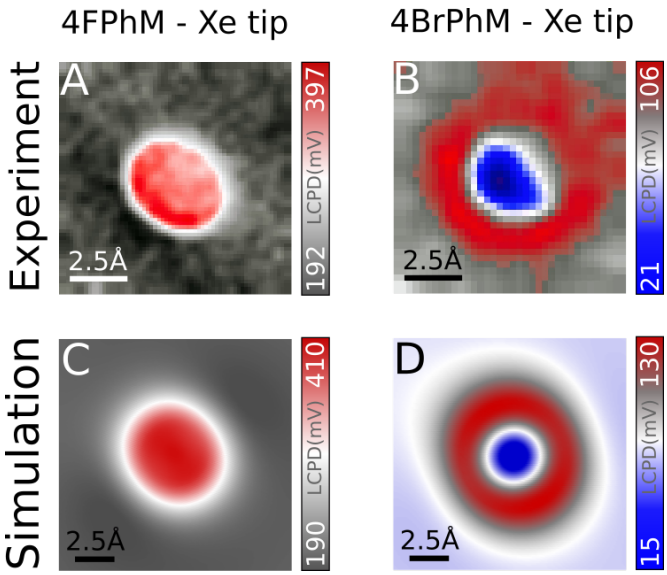

Figure 5.11: *(**A**, **B**) Experimental KPFM images of the 4FPhM (**A**) and 4BrPhM (**B**) molecules inspected with a Xe decorated tip. (**C** and **D**) Simulated KPFM images of the corresponding experiments.*

halogen atoms of the molecules.

The Figures 5.12 and 5.13 show simulated KPFM images calculated including: only the 1^{st} term (panel A1), the 2^{nd} term (panel A2), and both terms (A3), of equation 5.7. To illustrate the meaning of each image, panels B1 and B2 of Figures 5.12 and 5.13 schematize each interaction term, for $V > 0$, when the tip is positioned right above the halogen atom. Similarly, panels C1 and C2 of Figures 5.12 and 5.13 show each interaction when the tip is laterally displaced with respect to the halogen atom.

To understand the implications of each contribution in each case, lets start discussing the contribution of the 1^{st} term of equation 5.7 using the first column of Figures 5.12 and 5.13. We should remind for the analysis, that this term corresponds to the interaction between the dipole induced in the tip ($\delta\rho_t$) and the intrinsic charge of the sample (ρ_s^0).

For the case of 4FPhM, the interaction between $\delta\rho_t$ and ρ_s^0 is always repulsive (for $V > 0$) when we scan over the fluorine atom (see Figures 5.12B1 and 5.12C1). This situation creates an homogeneous image of positive values of V_{LCPD} (see Figure 5.12A1).

In the case of 4BrPhM, the dipole induced in the tip ($\delta\rho_t$) is attracted by the the positive crown of the bromine atom (Figure 5.13B1) when we scan the center of the atom. On the other hand, when the tip scans over the outer part of the bromine atom (Figure 5.13C1), the dipole induced in the tip ($\delta\rho_t$) is repelled by the negative belt of the Br atom. Then, this term will give rise to the image of the σ-hole showed in Figure 5.13A1. This analysis of the the 1^{st} term of the equation 5.7 illustrates how the dependence of this term with the tip position is given by the intrinsic charges of the sample (ρ_s^0).

A similar analysis can be done for the interaction of the dipoles induced in the sample ($\delta\rho_s$) interacting with the intrinsic charge of the tip (ρ_t^0), corresponding to the 2^{nd} term of equation 5.7. In panels B2 and C2 of Figures 5.12 and 5.13

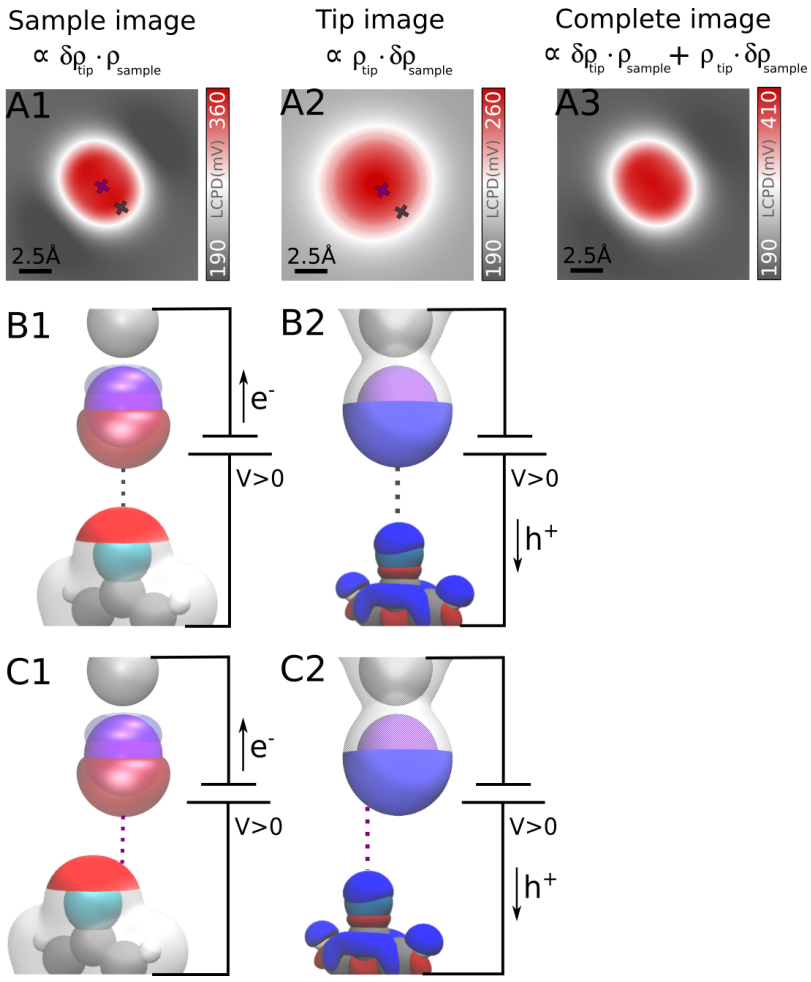

Figure 5.12: *(**A**) Simulated KPFM images of the 4FPhM molecule with a Xe decorated tip. (**A1**) Image including only the 1st term of equation 5.7, reflecting the electrostatic of the sample. (**A2**) Image including only the 2nd term of equation 5.7, reflecting the electrostatic of the tip. (**A3**) Complete KPFM image including the two contributions of panels **A1** and **A2**. (**B**) Schematic description of the interaction in each case. (**B1**) Induced dipoles in the tip interacting with the intrinsic charge of the sample and (**B2**) induced dipoles in the sample interacting with the intrinsic charge of the tip, for the case of the tip centered above the halogen atom. (**C**) Schematic description of the interactions mentioned in the case of panels **B**, but laterally displaced. In **B** and **C**, positive charge is depicted in blue and the negative charge in red.*

is shown that this component (for $V > 0$) is repulsive in all cases. Hence, this component shows the homogeneous positive charge of the Xe atom as a regular dot of positive V_{LCPD} values in Figures 5.12A2 and 5.13A2.

From the analysis of both terms we can conclude that:

- The 1st term of equation 5.7 provides an image of the charge distribution of the sample, weighted by the polarization of the tip
- The 2nd term of equation 5.7 provides an image of the charge distribution of the tip weighted by the polarization of the sample.

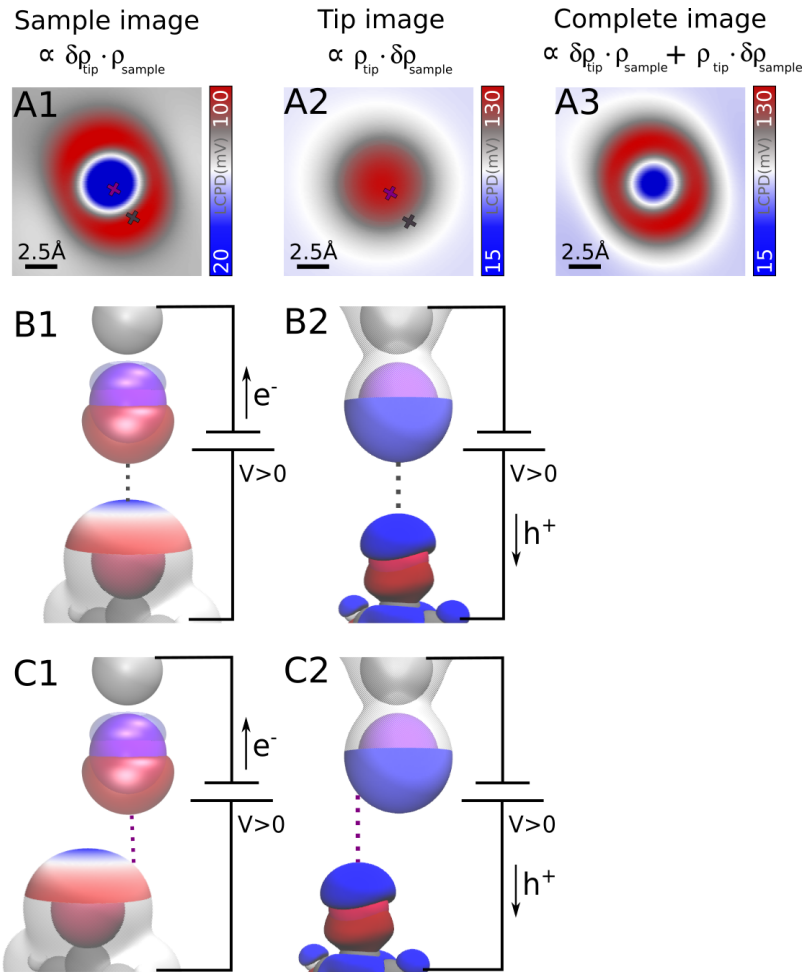

Figure 5.13: *(**A**) Simulated KPFM images of the 4BrPhM molecule with a Xe decorated tip. (**A1**) Image including only the 1^{st} term of equation 5.7, reflecting the electrostatic of the sample. (**A2**) Image including only the 2^{nd} term of equation 5.7, reflecting the electrostatic of the tip. (**A3**) Complete KPFM image including the two contributions of panels **A1** and **A2**. (**B**) Schematic description of the interaction in each case. (**B1**) Induced dipoles in the tip interacting with the intrinsic charge of the sample and (**B2**) induced dipoles in the sample interacting with the intrinsic charge of the tip, for the case of the tip centered above the halogen atom. (**C**) Schematic description of the interactions mentioned in the case of panels **B**, but laterally displaced. In **B** and **C**, positive charge is depicted in blue and the negative charge in red.*

In the case of the Xe decorated tip, we found that the probe has a large polarization. Consequently, the term we labeled as "image of the tip" dominates the complete image, allowing us to obtain an image of the σ-hole.

5.3.2 CO tip decoration and the characterization of its charge distribution.

The CO molecule is a common choice for tip termination in SPM experiments. Therefore, we decided to study the imaging mechanism using this tip functionalization. The Figure 5.14 shows the KPFM experimental and simulated images

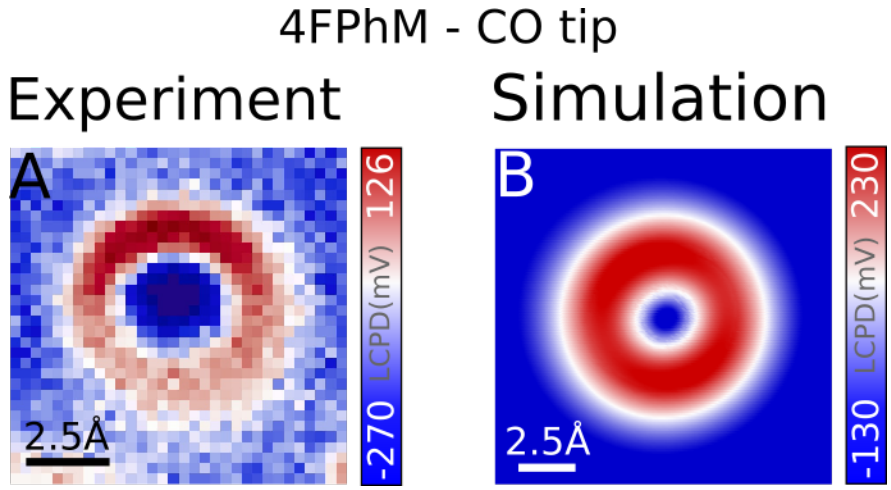

Figure 5.14: *(**A**) Experimental KPFM image of the 4FPhM molecule inspected with a CO decorated tip. (**B**) Simulated KPFM image of the corresponding Experiment.*

of the 4FPhM molecule, obtained with a CO decorated tip. Using the mentioned tip functionalization, we obtained a negative contrast feature in the center of the atom, surrounded by a belt of positive values of V_{LCPD}.

To understand the obtained images, we repeated the analysis of the imaging mechanism that we carried out in the previous section. The Figure 5.15 shows simulated KPFM images calculated including: only the 1^{st} term (panel A1), the 2^{nd} term (panel A2), and both terms (A3), of equation 5.7. To illustrate the meaning of each image, panels B1 and B2 of Figure 5.15 schematize each interaction term when the tip is positioned right above the fluorine atom. Similarly, panels C1 and C2 of Figure 5.15 depicts each interaction when the tip is laterally displaced with respect to the fluorine atom.

In this case (for $V > 0$), the 1^{st} term of equation 5.7 is repulsive (see Figure 5.15B1 and C1), creating the image of the fluorine atom showed in Figure 5.15A1. The 2^{nd} term of equation 5.7 will be attractive when the tip scan the center of the F atom, because $\delta\rho_s$ interacts mainly with the central lobe of the probe (see Figure 5.15B2). Then, when the tip scans the edge of the atom, $\delta\rho_s$ will be mainly repealed by the positive belt of the probe apex (see Figure 5.15C2). Then, this last term creates the image of the tip shown in Figure 5.15A2, with a positive dot in the center, surrounded by a belt of negative values of V_{LCPD}.

In the case of the images obtained with a CO decorated tip, we found the interaction arising from the 2^{nd} term of equation 5.7 to be stronger than the contribution of the 1^{st} term. This means that the experimental images obtained in this case (Figure 5.14) are and images of the CO molecule attached to the tip. With this analysis, we have confirmed the predictions of previous authors about a CO terminated tip.[83] A CO molecule attached to a metallic tip exhibits an inner negative lobe, surrounded by a positive ring as it is show in Figure 5.16)

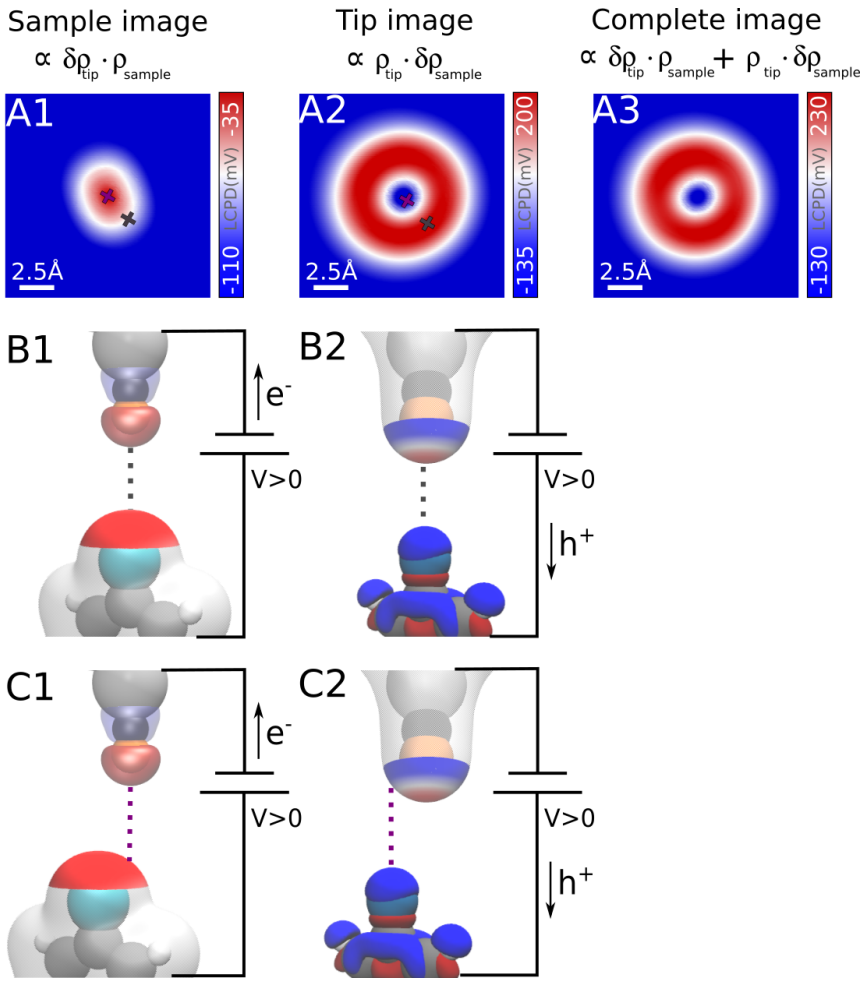

Figure 5.15: *(**A**) Simulated KPFM images of the 4FPhM molecule with a CO decorated tip. (**A1**) Image including only the 1^{st} term of equation 5.7, reflecting the electrostatic of the sample. (**A2**) Image including only the 2^{nd} term of equation 5.7, reflecting the electrostatic of the tip. (**A3**) Complete KPFM image including the two contributions of panels **A1** and **A2**. (**B**) Schematic description of the interaction in each case. (**B1**) Induced dipoles in the tip interacting with the intrinsic charge of the sample and (**B2**) induced dipoles in the sample interacting with the intrinsic charge of the tip, for the case of the tip centered above the halogen atom. (**C**) Schematic description of the interactions mentioned in the case of panels **B**, but laterally displaced. In **B** and **C**, positive charge is depicted in blue and the negative charge in red.*

5.4 Conclusions

In this work, we managed to obtain experimental images of anisotropic charge distributions at atomic scale using a KPFM set-up with the proper tip functionalization. We provided, for the first time, direct evidence of the existence of σ-holes in brominated tetraphenyl molecules deposited on a metallic substrate. We also obtained experimental profs of the electrostatic character of the CO terminated tip.

In order to understand the obtained experimental results, we have developed a new module of the probe particle model.[15] This new version of the code al-

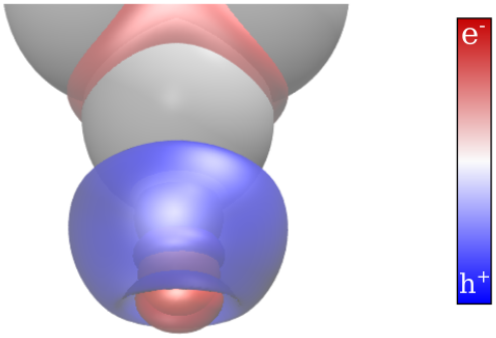

Figure 5.16: *Calculated differential charge density of the CO decorated silver [111] tip. The plotted isosurface is 0.02 a_0^{-3}. The blue lobes are positively charged and the red lobes are negatively charged.*

lows to carry out KPFM simulations, considering the changes in the tip-sample interaction force due to the bias-induced polarizations inside the junction.

We found the obtained KPFM images to be an interplay of two main contributions, one resembling the electrostatic landscape of the sample and other related with the electrostatic character of the probe apex. The performed simulations allowed us to separate the distinct contributions in computational experiments, so we could relate each aspect of the experimental images images to their true origin. In conclusion, the proposed model shows a very promising potential for the study of systems where the anisotropic distributions of charge play an important role.

6. Characterization of reactions on surfaces

The reactions that take place on surfaces are gathering large attention, due to their unusual reaction mechanisms, that could be for example conditioned by the reactants interaction with the substrate.[84–86] The use of the interaction between the molecules and the substrate to steer the reaction suppose an interesting tool for the solvent-free synthesis of nanostructures. Nevertheless, further developments of this methods can only be unleashed under a proper knowledge of the reaction mechanism. One extended option for the characterization of the reaction mechanism between organic molecules absorbed in metallic substrates are the DFT based methods.[87–90]

This chapter presents the work done to analyze the strain-induced isomerization of one-dimensional (1D) metal-organic chains (MOCs) on a Cu[111] substrate. This work offers an example of how SPM can be used to identify the reactants and products of reactions happening on planar surfaces. Using a combination of STM and AFM with a fuctionalized tip, it was possible to determine the structure and arrangement of the chains at atomic level before and after the reaction.

This project also allow us to show the potential of the QM/MM-based MD methods introduced in chapter 3 to characterize the reaction process considering the effect of temperature in the calculation. The QM/MM (quantum mechanics/molecular mechanics) allowed us to describe the system with a combination of DFT and classical force fields. Using this formalism, we could describe the large Cu[111] substrate with empirical force fields, while the bond breakage/formation was described by DFT. Using these methods, we managed to obtain the free energy barrier of the reaction, including the effect of vibrational modes and entropy in the studied process, rationalizing the experimental evidence.

6.1 Strain driven isomerization of metal-organic chains on a cooper [111] substrate

In this paper, we reported the isomerization of MOCs, driven by the internal strain induced by the interaction with the metallic substrate. First, 1,5-dibromo-2,6-dimethylnaphthalene (DBDMN) molecules were deposited on a Cu[111] substrate. Then, after the deposition, the C-Br bonds of the molecules broke, allowing them to create 1D chains via C-Cu-C links. Finally, after keeping the system at room temperature for a long time ($\sim$12h) the chains underwent to skeletal transformations. The C-Cu-C links enchanged positions with the C-H links, as it is shown in Figure 6.1, allowing the chains to adopt a new orientation with respect to the substrate. In the following it is commented how SPM experiments were combined with DFT, AFM and QM/MM-based MD simulations to identify the stages of the reaction and the isomerization mechanism.

First, we identified the skeleton and arrangement of the products and precursors of the reaction using the mentioned SPM experiments and simulations. To

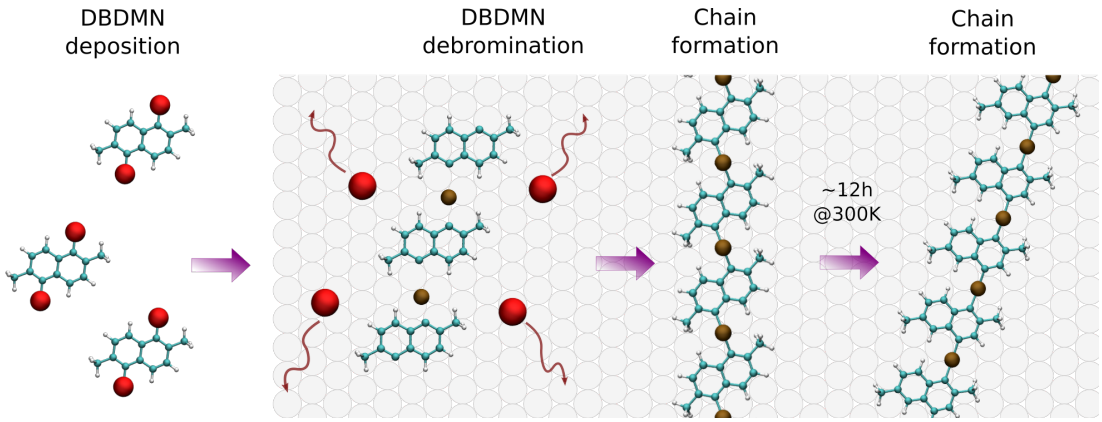

Figure 6.1: *Scheme of the formation and isomerization of one-dimensional (1D) metal-organic chains (MOCs) from 1,5-dibromo-2,6-dimethylnaphthalene (DBDMN) molecules on a Cu[111] substrate. First the DBDMN molecules were deposited in the substrate. Then the molecules lost the bromine termination to form MOCs along the [110] direction of the Cu[111] surface. Finally, after 12 hours at room temperature, the chains underwent a internal transformation.*

do so, AFM and STM images were obtained experimentally. Then, to confirm the interpretation of the experimental results, we also simulated AFM images using the probe particle (PP) model.[15] The obtained images can be found in the original publication[91] (see the 3^{rd} appended paper at the end of the thesis). We found the inner structure of the dimethylnaphthalene molecules (terminated with CH_3) that form the chain to be non-planar when they are absorbed in the substrate (see Figure 6.2a). The AFM images in this case showed only a few bright spots along the chain, that we identified as the methyl groups that terminate the molecules, pointing out of plane. To overcome this problem, the dehydrogenation of the methyl groups was induced by scanning with STM at high voltages ($\sim$2.0V). This new termination (CH_2) allowed the molecules to adopt a planar configuration (see Figure 6.2b) in which their complete skeleton could be imaged with AFM.

Then, it was found that when the chains were left to evolve for around 12 hours at room temperature before carry out the above described dehydrogenation process, the inner structure of the chains changed (as is indicated in Figure 6.3). During this time, an isomerization reaction occurred, changing the position of the C-Cu-C linkers inside the chains. We also noticed that, this isomerization was accompanied by a rotation of the chains with respect to the metallic substrate. The angle of rotation was experimentally determined by imaging the molecular structure of the chains and the cooper surface in the same session.

While the chains right after deposition were oriented along the high symmetry [110] direction of the substrate, the chains after the reaction were found to be rotated approximately 20° with respect to the initial direction (see Figure 6.3). The orientation acquired after the isomerization allowed the chains, in their new conformation, to adopt a lattice constant closer to the ideal one. According to our DFT calculations, the change in the registry after the isomerization releases around $0.28eV$ per molecule of mechanical strain energy.

To obtain a deeper insight of the reaction mechanism, we carried out QM/MM-

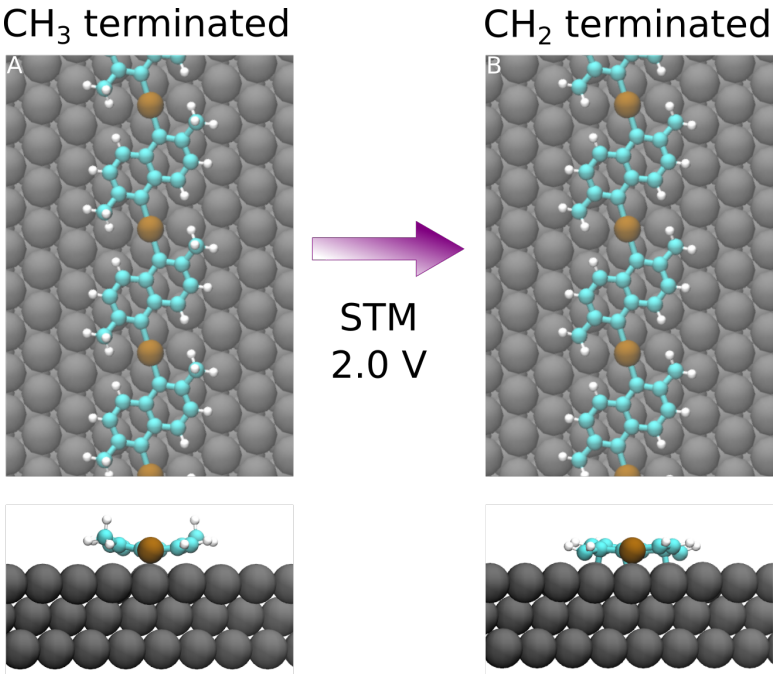

Figure 6.2: *DFT relaxed structure of the chains before and after the tip-induced dehydrogenation. (**A**) The chains right after the chain formation are terminated with CH_3 groups. This termination makes the molecules in the chain adopt a non-planar configuration. (**B**) After an STM scan using a bias of 2.0V the CH_3 terminals dehydrogenate, allowing the molecules to adopt a planar configuration. The different elements of the system are depicted as follows: cooper substrate in gray, cooper ad atoms in ochre, carbon atoms in blue and hydrogen atoms in white.*

based MD simulations to obtain the free energy barrier of the reaction, using the umbrella sampling algorithm. This method applies a series of constrains to the system, usually on the shape of external harmonic potentials, to drive it along the proposed reaction pathway. These potentials will force the system to overcome a given energy barrier in the direction of a so-called reaction coordinate. These coordinates could be, for example, the angle between two bonds or the distance between two atoms. Then, the weighted histogram analysis method (WHAM)[92] was used to extract the free energy barrier. This method analyze the results from a large enough number of MD calculations under each of the constrains set along the reaction path to calculate the free energy barrier.

For the QM/MM-based MD simulations of the reaction, we chose a MOC formed by 3 dimethylnaphthalene molecules linked by cooper atoms absorbed on a Cu [111] substrate with a thickness of 3 layers. As it was mentioned at the begining of this chapter, we chose to treat the system with the QM/MM method. This treatment allowed us to obtain a good description of the bond breakage/formation, while keepeing the simulation computationally afordable.

A proper definition of the QM and MM regions of the system is non trivial and it is worthy to discuss the aspects we considered for the choice. First, we decided to describe the MOCs (3 molecules and 3 Cu linker atoms) with QM methods, as it was necessary to describe the bond breakage/formation. Then, we found that the charge transference between the MOCs and the substrate during

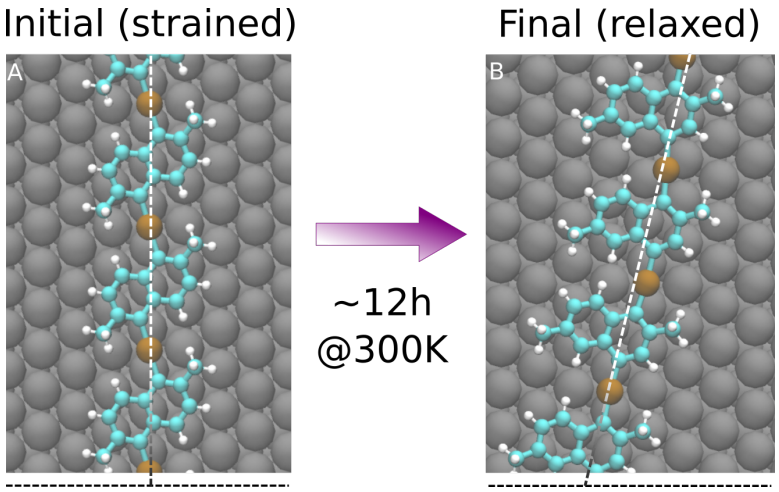

Figure 6.3: *Isomerization reaction scheme. DFT relaxed structures of the MOCs (**A**) before and (**B**) after the strain-driven reaction occurred after evolve at room temperature for 12 hours. The different elements of the system are depicted as follows: cooper substrate in gray, cooper ad atoms in ochre, carbon atoms in blue and hydrogen atoms in white.*

the reaction played an important role in the isomerization mechanism. Hence it was also necessary to include part of the Cu[111] substrate in the quantum region, specifically 28 atoms of the top layer of substrate inmediately behind the molecule. To finish the definition, the rest of the Cu[111] substrate was described with an empirical force field, obtaining a sufficient description of the Pauli and dispersion interactions at a very low computational cost.

We found the most favorable reaction pathway to be a two step process, where the Cu atom and the neighbouring hydrogen simultaneously exchange their bonds with the carbon atoms. The reaction process is briefly schematized in the Figure 6.4 and detailed in the original publication[91] that can be found in the appendix. First the hydrogen bonds with the cooper atom, weakening its interaction with the naphthalene molecule and the substrate (in Figure 6.4 the transition from A to B). Then, the Cu atom can form a new Cu-C bond and break the former one, allowing the chain to adopt its new configuration (in Figure 6.4 the transition from B to C).

Interestingly, our calculations predict that at high temperatures out-of-plane vibrational modes of the molecular chains are activated. This allows the molecules to oscillate around higher vertical distances with respect to the substrate. A comparison of the vertical oscillation of different parts of the chain at 50, 100 and 300 Kelvin can be found in the supplementary information of the paper. As an illustrative example, we found the Cu atoms inside the chain to oscillate at 300K around 0.5Å higher with respect to the substrate than in the same calculation at 50K. The access to these vibrational modes had a direct effect in the chain-substrate interaction, facilitating the movement of the atoms and lowering the activation barrier.

In summary, with this project we intended to contribute to the understanding of strain-driven reactions occurring on surfaces. We used a combined effort of experimental and theoretical work to deduce the initial and final stages of the process. Thanks to the results obtained with SPM methods, we could find

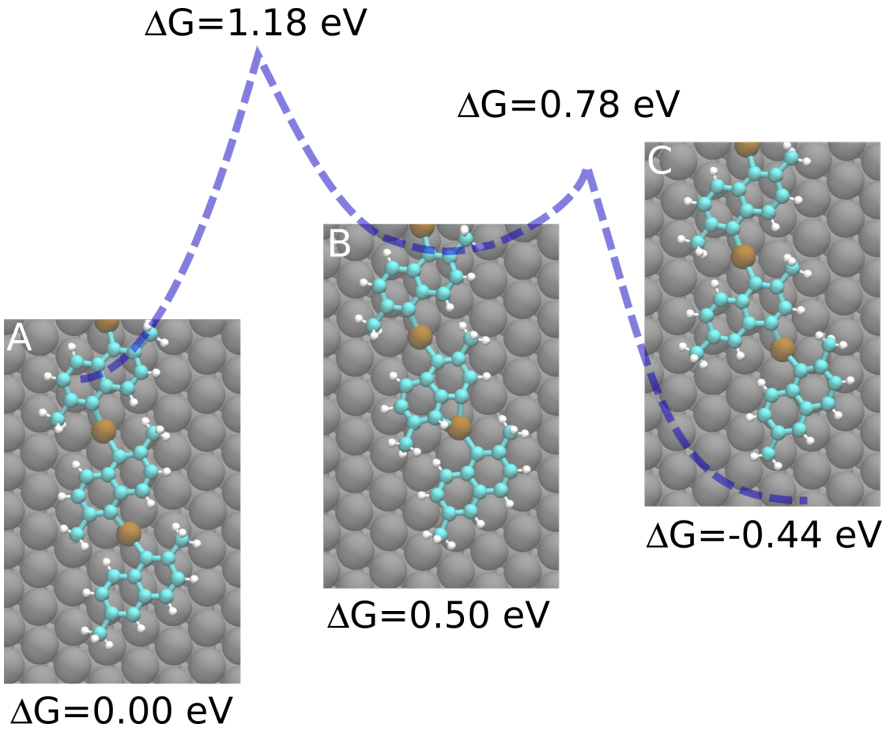

Figure 6.4: *Description of the reaction mechanism. First the hydrogen bonds with the cooper atom, weakening its interaction with the naphthalene molecule and the substrate. This process implies a free energy barrier of* $1.18eV$ *(transition from* ***A*** *to* ***B****). Then, the Cu-C bond beaks, allowing the chain to adopt its new configuration (transition from* ***B*** *to* ***C****). This second stage of the process implies a barrier of* $0.78eV$*, ending in a structure of* $0.44eV$ *lower free energy, compared with the initially considered configuration. The different elements of the system are depicted as follows: cooper substrate in gray, cooper ad atoms in ochre, carbon atoms in blue and hydrogen atoms in white.*

the implications of the chain-substrate interaction and confirm the role of the mechanical strain in the reaction process with DFT calculations.

We have also carried out QM/MM-based MD simulations to successfully describe the most probable reaction mechanism at atomic level. This kind of simulations are well-known in fields such as theoretical biology, where they have been used for decades, but remain relatively unexploited in the field of surface sciences. This project is, up to our knowledge, the first application of QM/MM-based MD simulations including temperature to the characterization of on-surface reactions occurring on metallic substrates. In this sense, deeper studies of the reaction process or the crucial parameters of the simulations in the context of surface sciences could be of high interest. It illustrates the potential of the QM/MM method to describe the reactions occurring on surfaces, setting a good starting point for further studies of on-surface reactions.

Conclusion

During the last four decades, the scanning probe microscopy (SPM) techniques have proven to be one of the most powerful tools for the study of the surfaces of solids and planar structures at the atomic level. At the same time, great efforts have been made in the development of theoretical models and computational tools in order to describe the underlying imaging mechanisms. To contribute to this effort, most of the work presented in this thesis focuses on the analysis of the interaction between tip and sample in different SPM experiments.

An important application of the SPM techniques is the characterization of the reactants and products of chemical reactions happening on surfaces, which have been gathering interest during the last decades. In order to characterize also the physical mechanism that rule the reaction itself, different theoretical approaches are available. This thesis presents the molecular dynamics (MD) calculations, using the quantum mechanics/molecular mechanics (QM/MM) formalism, carried out to describe the isomerization mechanism of metalorganic chains (MOCs).

Some of the most interesting results I have obtained during my PhD studies are collected in this thesis. In the following I recapitulate the main conclusions and future expectations of the discussed projects in descending order of scientific transcendence.

In chapter 5, I describe the combination of experiments and theoretical simulations carried out in order to demonstrate the until then only predicted existence of the σ-hole. This chapter details the implementation of a computational model developed to simulate Kelvin probe force microscope (KPFM) images. Using this model, we could relate each aspect of the experimental images with its true origin.

This computational model shows a very promising potential for the study of systems where the anisotropic distributions of charge play an important role. Recently, we used it to confirm the charge distribution of a diazahexabenzocoronene derivative deposited on a Au[111] substrate.[80] In this work, we used the developed KPFM computational model to corroborate the KPFM experimental findings that denote the positive charge state of the molecules.

Additionally, this KPFM model is currently being used not only by myself but also by other colleagues in various projects that are expected to be published during the following years. We believe that the developed model represents a solid theoretical framework for KPFM, helping the further proliferation of the technique. The agreement between the experimental and theoretical results suggest a good validity of the method. However, it will be its application to various systems what will reveal the limits of applicability of the model. We expect the results to be favorable for most systems where the chemical interaction between tip and sample is weak. Anyhow, it could be interesting to consider, for example, the charge reorganization due to the tip-sample interaction and its dependence with the applied bias in further developments of the model.

In chapter 6, I reviewed the work we carried out in order to characterize the strain-induced isomerization of metal-organic chains (MOCs) occurring on a metallic substrate. To do so, we used molecular dynamics (MD) calculations, with the atomic interaction described with a combination of density functional theory (DFT) and classical force fields. The obtained results demonstrated the great

efficacy of QM/MM based methods to study reactions happening in the frame of crystalline surfaces. The combination of quantum and classical mechanics to describe the system allows for a proper characterization of chemical transformations, inside a vast system under minimal computational cost. We found out that the charge transference between the studied MOCs and the cooper [111] surface in which they are deposited played an important role in the reaction. An interesting topic to investigate in this line could be the effect of different substrates in the reactions that take place on them. The different reactivity of the commonly used metallic substrates could affect or even completely change the mechanism of certain reactions. Because we found the vibrations of atoms in the system to play a role, we believe this study should be done including the thermal energy in the calculations to take the effect of vibrational modes into consideration. Also, given the size of the studied systems and the need of a proper description of the charge effects, our opinion is that the QM/MM methods are the most appropriated tool for the job.

An additional aspect of the MOCs isomerization that we would have liked to investigate in greater depth is the subsequent isomerization of molecules along the chains once the reaction have started. In the simulations performed in the work presented in the chapter 6, we have only studied the isomerization of one molecule at the end of a MOCs. We suspect that, as the following molecules undergo the reaction and adopt their new alignment with the substrate, additional strain forces could appear, enhancing the reaction.

In chapter 4, I discuss our work addressing the important topic of the extensively debated visualization of weak intermolecular interactions using SPM. The interpretation of certain aspects of high-resolution SPM images are still under debate. To tackle this topic we discuss the SPM imaging mechanism and provide a solid rationalization of the origin of the intermolecular sharp features often obtained experimentally. There, we relate the sharp edges obtained in inelastic electron tunnel spectroscopy (IETS) and AFM experiments with the probe bending at close tip-sample distances in the presence of saddle points of the potential energy. Then, we discuss the source of these saddle points for the case of covalent and non-covalent bonds in the sample.

Covalent bonding implies a strong rehibridization of the electronic states of the costituiting atoms. This gives rise to a strong localization of charge between the bonded atoms that can be easily related with the sharp edges observed experimentally. On the other hand, non-covalent interactions such as electrostatic and dispersion interactions have a non-local character. Therefore it is not straightforward to relate these kind of interactions with a very localized signal like the sharp edges observed experimentally.

We found the intermolecular features in the images to be the result of a proximity effect. The probe is deflected due to the saddle point created by the mere presence of two atoms in the sample close to each other and not by any bond-related physical phenomena. The obtained results brought out the importance of understanding the imaging mechanism in order to carry out a proper interpretation of the experimental images.

As final conclusions, the theoretical calculations and computational experiments have shown themselves as powerful research tools for surface sciences. To follow this line of research, this thesis intends to contribute to the development

of theoretical frameworks for the on-surface research. In closing, although much work has been done to contribute to the theoretical description of on-surface systems, much remains to be done.

Bibliography

[1] Y. Wakayama, "On-surface molecular nanoarchitectonics: From self-assembly to directed assembly," *Japanese Journal of Applied Physics*, vol. 55, no. 11, pp. 1102AA.1–1102AA.13, 2016.

[2] J. Elemans, S. Lei, and S. DeFeyter, "Molecular and supramolecular networks on surfaces: From two-dimensional crystal engineering to reactivity," *Angewandte Chemie International Edition*, vol. 48, no. 40, pp. 7298–7332, 2009.

[3] X. Bouju, C. Mattioli, G. Franc, A. Pujol, and A. Gourdon, "Bicomponent supramolecular architectures at the vacuum–solid interface," *Chemical Reviews*, vol. 117, no. 3, pp. 1407–1444, 2017.

[4] R. Otero, A. Vázquez de Parga, and J. Gallego, "Electronic, structural and chemical effects of charge-transfer at organic/inorganic interfaces," *Surface Science Reports*, vol. 72, no. 3, pp. 105–145, 2017.

[5] D. P. Goronzy, M. Ebrahimi, F. Rosei, Arramel, Y. Fang, S. De Feyter, S. L. Tait, C. Wang, P. H. Beton, A. T. S. Wee, P. S. Weiss, and D. F. Perepichka, "Supramolecular assemblies on surfaces: Nanopatterning, functionality, and reactivity," *ACS Nano*, vol. 12, no. 8, pp. 7445–7481, 2018.

[6] L. Talirz, P. Ruffieux, and R. Fasel, "On-surface synthesis of atomically precise graphene nanoribbons," *Advanced Materials*, vol. 28, no. 29, pp. 6222–6231, 2016.

[7] L. Lafferentz, F. Ample, H. Yu, S. Hecht, C. Joachim, and L. Grill, "Conductance of a single conjugated polymer as a continuous function of its length," *Science*, vol. 323, no. 5918, pp. 1193–1197, 2009.

[8] A. Sánchez-Grande, J. I. Urgel, A. Cahlík, J. Santos, S. Edalatmanesh, E. Rodríguez-Sánchez, K. Lauwaet, P. Mutombo, D. Nachtigallová, R. Nieman, H. Lischka, B. de la Torre, R. Miranda, O. Gröning, N. Martín, P. Jelínek, and D. Écija, "Diradical organic one-dimensional polymers synthesized on a metallic surface," *Angewandte Chemie International Edition*, vol. 59, no. 40, pp. 17594–17599, 2020.

[9] A. K. Geim and I. V. Grigorieva, "Van der waals heterostructures," *Nature*, vol. 499, no. 7459, pp. 419–425, 2013.

[10] M. Xu, T. Liang, M. Shi, and H. Chen, "Graphene-like two-dimensional materials," *Chemical Reviews*, vol. 113, no. 5, pp. 3766–3798, 2013.

[11] K. S. Novoselov, A. K. Geim, S. V. Morozov, D. Jiang, Y. Zhang, S. V. Dubonos, I. V. Grigorieva, and A. A. Firsov, "Electric field effect in atomically thin carbon films," *Science*, vol. 306, no. 5696, pp. 666–669, 2004.

[12] H. Lüth, *Solid Surfaces, Interfaces and Thin Films*. Springer Berlin Heidelberg, 2010.

[13] G. Binnig and H. Rohrer, "Scanning tunneling microscopy," *Surface Science*, vol. 126, no. 1, pp. 236–244, 1983.

[14] G. Binnig, C. F. Quate, and C. Gerber, "Atomic force microscope," *Physical Review Letters*, vol. 56, pp. 930–933, 1986.

[15] P. Hapala, G. Kichin, C. Wagner, F. S. Tautz, R. Temirov, and P. Jelínek, "Mechanism of high-resolution stm/afm imaging with functionalized tips," *Physical Review B*, vol. 90, pp. 085421.1–085421.9, 2014.

[16] O. Krejčí, P. Hapala, M. Ondráček, and P. Jelínek, "Principles and simulations of high-resolution stm imaging with a flexible tip apex," *Physical Review B*, vol. 95, pp. 045407.1–045407.9, 2017.

[17] S. Hämäläinen, N. van der Heijden, J. van der Lit, S. den Hartog, P. Liljeroth, and I. Swart, "Intermolecular Contrast in Atomic Force Microscopy Images without Intermolecular Bonds," *Physical Review Letters*, vol. 113, no. 18, pp. 186102.1–186102.5, 2014.

[18] C.-S. Guo, M. A. Van Hove, X. Ren, and Y. Zhao, "High-resolution model for noncontact atomic force microscopy with a flexible molecule on the tip apex," *The Journal of Physical Chemistry C*, vol. 119, no. 3, pp. 1483–1488, 2015.

[19] Y. Sakai, A. J. Lee, and J. R. Chelikowsky, "First-principles atomic force microscopy image simulations with density embedding theory," *Nano Letters*, vol. 16, no. 5, pp. 3242–3246, 2016.

[20] M. Ellner, P. Pou, and R. Pérez, "Atomic force microscopy contrast with co functionalized tips in hydrogen-bonded molecular layers: Does the real tip charge distribution play a role?," *Physical Review B*, vol. 96, pp. 075418.1–075418.9, 2017.

[21] N. W. Ashcroft and N. D. Mermin, *Solid State Physics*. Philadelphia, United States of America: Holt-Saunders, 1 ed., 1976.

[22] R. Dronskowski, *Computational chemistry of solid state materials: A guide for materials scientists, chemists, physicists and others*. Weinheim, Germany: Wiley-VCH Verlag, 1 ed., 2008.

[23] E. Engel and R. Dreizler, *Density Functional Theory: An Advanced Course*, vol. 1. Berlin, Germany: Springer, 1 ed., 2010.

[24] M. Tuckerman, *Statistical Mechanics: Theory And Molecular Simulation*. Oxford, United Kingdom: Oxford University Press, 1 ed., 2001.

[25] J. Björk, "Reaction mechanisms for on-surface synthesis of covalent nanostructures," *Journal of Physics: Condensed Matter*, vol. 28, no. 8, p. 083002, 2016.

[26] J. A. McCammon, B. R. Gelin, and M. Karplus, "Dynamics of folded proteins," *Nature*, vol. 267, no. 5612, pp. 585–590, 1977.

[27] G. Zhao, J. R. Perilla, E. L. Yufenyuy, X. Meng, B. Chen, J. Ning, J. Ahn, A. M. Gronenborn, K. Schulten, C. Aiken, and P. Zhang, "Mature hiv-1 capsid structure by cryo-electron microscopy and all-atom molecular dynamics," *Nature*, vol. 497, no. 7451, pp. 643–646, 2013.

[28] X. Liu, A. Matej, T. Kratky, J. I. Mendieta-Moreno, S. Günther, P. Mutombo, S. Decurtins, U. Aschauer, J. Repp, P. Jelinek, S.-X. Liu, and L. L. Patera, "Exploiting cooperative catalysis for the on-surface synthesis of linear heteroaromatic polymers via selective c–h activation," *Angewandte Chemie International Edition*, vol. 61, no. 5, pp. e202112798.1–e202112798.6, 2022.

[29] B. Mallada, B. de la Torre, J. I. Mendieta-Moreno, D. Nachtigallová, A. Matěj, M. Matoušek, P. Mutombo, J. Brabec, L. Veis, T. Cadart, M. Kotora, and P. Jelínek, "On-surface strain-driven synthesis of nonalternant nonbenzenoid aromatic compounds containing four- to eight-membered rings," *Journal of the American Chemical Society*, vol. 143, no. 36, pp. 14694–14702, 2021.

[30] J. Bardeen, "Tunnelling from a many-particle point of view," *Physical Review Letters*, vol. 6, pp. 57–59, 1961.

[31] B. Voigtländer, *Scanning Probe Microscopy*. Berlin, Germany: Springer, 1 ed., 2015.

[32] J. Chen, *Introduction to Scanning Tunneling Microscopy*. Oxford, United Kingdom: Oxford University Press, 2 ed., 2007.

[33] C. J. Chen, "Tunneling matrix elements in three-dimensional space: The derivative rule and the sum rule," *Physical Review B*, vol. 42, pp. 8841–8857, 1990.

[34] F. J. Giessibl, "Advances in atomic force microscopy," *Reviews of Modern Physics*, vol. 75, pp. 949–983, 2003.

[35] J. N. Israelachvili, *Intermolecular and surface forces*. San Diego, United States of America: Academic Press London, 2 ed., 1991.

[36] F. J. Giessibl, "Forces and frequency shifts in atomic-resolution dynamic-force microscopy," *Physical Review B*, vol. 56, pp. 16010–16015, 1997.

[37] L. Kelvin, "V. contact electricity of metals," *The London, Edinburgh, and Dublin Philosophical Magazine and Journal of Science*, vol. 46, no. 278, pp. 82–120, 1898.

[38] L. Gross, F. Mohn, N. Moll, P. Liljeroth, and G. Meyer, "The chemical structure of a molecule resolved by atomic force microscopy," *Science*, vol. 325, no. 5944, pp. 1110–1114, 2009.

[39] S. Morita, F. Giessibl, E. Meyer, and R. Wiesendanger, *Noncontact Atomic Force Microscopy Vol. 3*. Aargau, Switzerland: Springer NanoScience and Technology, 3 ed., 2015.

[40] L. Gross, F. Mohn, N. Moll, B. Schuler, A. Criado, E. Guitián, D. Peña, A. Gourdon, and G. Meyer, "Bond-order discrimination by atomic force microscopy," *Science*, vol. 337, no. 6100, pp. 1326–1329, 2012.

[41] J. Repp, G. Meyer, S. M. Stojković, A. Gourdon, and C. Joachim, "Molecules on insulating films: Scanning-tunneling microscopy imaging of individual molecular orbitals," *Physical Review Letters*, vol. 94, pp. 026803.1–026803.4, 2005.

[42] R. Temirov, S. Soubatch, O. Neucheva, A. C. Lassise, and F. S. Tautz, "A novel method achieving ultra-high geometrical resolution in scanning tunnelling microscopy," *New Journal of Physics*, vol. 10, no. 5, pp. 053012.1–053012.11, 2008.

[43] L. Gross, N. Moll, F. Mohn, A. Curioni, G. Meyer, F. Hanke, and M. Persson, "High-resolution molecular orbital imaging using a *p*-wave stm tip," *Physical Review Letters*, vol. 107, p. 086101, 2011.

[44] C. lun Chiang, C. Xu, Z. Han, and W. Ho, "Real-space imaging of molecular structure and chemical bonding by single-molecule inelastic tunneling probe," *Science*, vol. 344, no. 6186, pp. 885–888, 2014.

[45] B. C. Stipe, M. A. Rezaei, and W. Ho, "Single-molecule vibrational spectroscopy and microscopy," *Science*, vol. 280, no. 5370, pp. 1732–1735, 1998.

[46] P. Hapala, R. Temirov, F. S. Tautz, and P. Jelínek, "Origin of high-resolution iets-stm images of organic molecules with functionalized tips," *Physical Review Letters*, vol. 113, pp. 226101.1–226101.5, 2014.

[47] N. Pavliček, B. Fleury, M. Neu, J. Niedenführ, C. Herranz-Lancho, M. Ruben, and J. Repp, "Atomic force microscopy reveals bistable configurations of dibenzo[a,h]thianthrene and their interconversion pathway," *Physical Review Letters*, vol. 108, pp. 086101.1–086101.5, 2012.

[48] C. Møller and M. S. Plesset, "Note on an approximation treatment for many-electron systems," *Physical Review*, vol. 46, pp. 618–622, 1934.

[49] P. Hohenberg and W. Kohn, "Inhomogeneous electron gas," *Physical Review*, vol. 136, pp. B864–B871, 1964.

[50] J. P. Perdew and A. Zunger, "Self-interaction correction to density-functional approximations for many-electron systems," *Physical Review B*, vol. 23, pp. 5048–5079, 1981.

[51] A. D. Becke, "Density-functional exchange-energy approximation with correct asymptotic behavior," *Physical Review A*, vol. 38, pp. 3098–3100, 1988.

[52] C. Lee, W. Yang, and R. G. Parr, "Development of the colle-salvetti correlation-energy formula into a functional of the electron density," *Physical Review B*, vol. 37, pp. 785–789, 1988.

[53] J. P. Perdew, K. Burke, and M. Ernzerhof, "Generalized gradient approximation made simple," *Physical Review Letters*, vol. 77, pp. 3865–3868, 1996.

[54] J. P. Perdew, M. Ernzerhof, and K. Burke, "Rationale for mixing exact exchange with density functional approximations," *The Journal of Chemical Physics*, vol. 105, no. 22, pp. 9982–9985, 1996.

[55] A. D. Becke, "A new mixing of hartree–fock and local density-functional theories," *The Journal of Chemical Physics*, vol. 98, no. 2, pp. 1372–1377, 1993.

[56] S. Grimme, J. Antony, S. Ehrlich, and H. Krieg, "A consistent and accurate ab initio parametrization of density functional dispersion correction (dft-d) for the 94 elements h-pu," *The Journal of Chemical Physics*, vol. 132, no. 15, pp. 154104.1–154104.19, 2010.

[57] A. Tkatchenko and M. Scheffler, "Accurate molecular van der waals interactions from ground-state electron density and free-atom reference data," *Physical Review Letters*, vol. 102, pp. 073005.1–073005.4, 2009.

[58] G. Román-Pérez and J. M. Soler, "Efficient implementation of a van der waals density functional: Application to double-wall carbon nanotubes," *Physical Review Letters*, vol. 103, pp. 096102.1–096102.4, 2009.

[59] A. Tkatchenko, R. A. DiStasio, R. Car, and M. Scheffler, "Accurate and efficient method for many-body van der waals interactions," *Physical Review Letters*, vol. 108, pp. 236402.1–236402.5, 2012.

[60] J. Klimeš and A. Michaelides, "Perspective: Advances and challenges in treating van der waals dispersion forces in density functional theory," *The Journal of Chemical Physics*, vol. 137, no. 12, pp. 120901.1–120901.12, 2012.

[61] L. Verlet, "Computer "experiments" on classical fluids. i. thermodynamical properties of lennard-jones molecules," *Physical Review*, vol. 159, pp. 98–103, 1967.

[62] A. Warshel and M. Levitt, "Theoretical studies of enzymic reactions: Dielectric, electrostatic and steric stabilization of the carbonium ion in the reaction of lysozyme," *Journal of Molecular Biology*, vol. 103, no. 2, pp. 227–249, 1976.

[63] M. J. Field, P. A. Bash, and M. Karplus, "A combined quantum mechanical and molecular mechanical potential for molecular dynamics simulations," *Journal of Computational Chemistry*, vol. 11, no. 6, pp. 700–733, 1990.

[64] D. A. Pearlman, D. A. Case, J. W. Caldwell, W. S. Ross, T. E. Cheatham, S. DeBolt, D. Ferguson, G. Seibel, and P. Kollman, "Amber, a package of computer programs for applying molecular mechanics, normal mode analysis, molecular dynamics and free energy calculations to simulate the structural and energetic properties of molecules," *Computer Physics Communications*, vol. 91, no. 1, pp. 1–41, 1995.

[65] R. P. Feynman, "Forces in molecules," *Physical Review*, vol. 56, pp. 340–343, 1939.

[66] J. I. Mendieta-Moreno, R. C. Walker, J. P. Lewis, P. Gómez-Puertas, J. Mendieta, and J. Ortega, "fireball/amber: An efficient local-orbital dft qm/mm method for biomolecular systems," *Journal of Chemical Theory and Computation*, vol. 10, no. 5, pp. 2185–2193, 2014.

[67] M. H. Kolář and P. Hobza, "Computer modeling of halogen bonds and other σ-hole interactions," *Chemical Reviews*, vol. 116, no. 9, pp. 5155–5187, 2016.

[68] P. Politzer, P. Lane, M. C. Concha, Y. Ma, and J. S. Murray, "An Overview of Halogen Bonding," *Journal of Molecular Modeling*, vol. 13, no. 2, pp. 305–311, 2007.

[69] P. Politzer, J. S. Murray, and M. C. Concha, "σ-Hole Bonding Between like Atoms; a Fallacy of Atomic Charges," *Journal of Molecular Modeling*, vol. 14, no. 8, pp. 659–665, 2008.

[70] J. S. Murray, P. Lane, and P. Politzer, "A Predicted New Type of Directional Noncovalent Interaction," *International Journal of Quantum Chemistry*, vol. 107, no. 12, pp. 2286–2292, 2007.

[71] J. S. Murray, P. Lane, and P. Politzer, "Expansion of the σ-Hole Concept," *Journal of Molecular Modeling*, vol. 15, no. 6, pp. 723–729, 2009.

[72] T. Clark, M. Hennemann, J. S. Murray, and P. Politzer, "Halogen Bonding: The σ-Hole," *Journal of Molecular Modeling*, vol. 13, no. 2, pp. 291–296, 2007.

[73] Z. Han, G. Czap, C.-l. Chiang, C. Xu, P. J. Wagner, X. Wei, Y. Zhang, R. Wu, and W. Ho, "Imaging the Halogen Bond in Self-Assembled Halogenbenzenes on Silver," *Science*, vol. 358, no. 6360, pp. 206–210, 2017.

[74] J. Zhang, P. Chen, B. Yuan, W. Ji, Z. Cheng, and X. Qiu, "Real-Space Identification of Intermolecular Bonding with Atomic Force Microscopy," *Science*, vol. 342, no. 6158, pp. 611–614, 2013.

[75] S. Kawai, A. Sadeghi, F. Xu, L. Peng, A. Orita, J. Otera, S. Goedecker, and E. Meyer, "Extended Halogen Bonding between Fully Fluorinated Aromatic Molecules," *ACS Nano*, vol. 9, no. 3, pp. 2574–2583, 2015.

[76] F. Mohn, L. Gross, N. Moll, and G. Meyer, "Imaging the charge distribution within a single molecule," *Nature Nanotechnology*, vol. 7, pp. 227–231, 2012.

[77] L. Nony, A. S. Foster, F. Bocquet, and C. Loppacher, "Understanding the atomic-scale contrast in kelvin probe force microscopy," *Physical Review Letters*, vol. 103, pp. 036802–036805, 2009.

[78] B. Mallada, S. Edalatmanesh, P. Lazar, J. Redondo, A. Gallardo, R. Zbořil, P. Jelínek, M. Švec, and B. de la Torre, "Atomic-scale charge distribution mapping of single substitutional p- and n-type dopants in graphene," *ACS Sustainable Chemistry & Engineering*, vol. 8, no. 8, pp. 3437–3444, 2020.

[79] S. Sadewasser and T. Glatzel, *Kelvin probe force microscopy: measuring and compensating electrostatic forces*, vol. 65. Aargau, Switzerland: Springer Surface Science, 1 ed., 2011.

[80] K. Biswas, J. I. Urgel, K. Xu, J. Ma, A. Sánchez-Grande, P. Mutombo, A. Gallardo, K. Lauwaet, B. Mallada, B. de la Torre, A. Matěj, J. M. Gallego, R. Miranda, P. Jelínek, X. Feng, and D. Écija, "On-surface synthesis of a dicationic diazahexabenzocoronene derivative on the au(111) surface," *Angewandte Chemie International Edition*, vol. 60, no. 48, pp. 25551–25556, 2021.

[81] S. Hudlet, M. Saint Jean, C. Guthmann, and J. Berger, "Evaluation of the capacitive force between an atomic force microscopy tip and a metallic surface," *The European Physical Journal B - Condensed Matter and Complex Systems*, vol. 2, no. 1, pp. 5–10, 1998.

[82] B. Mallada, A. Gallardo, M. Lamanec, B. de la Torre, V. Špirko, P. Hobza, and P. Jelinek, "Real-space imaging of anisotropic charge of σ-hole by means of kelvin probe force microscopy," *Science*, vol. 374, no. 6569, pp. 863–867, 2021.

[83] M. Ellner, N. Pavliček, P. Pou, B. Schuler, N. Moll, G. Meyer, L. Gross, and R. Peréz, "The electric field of co tips and its relevance for atomic force microscopy," *Nano Letters*, vol. 16, no. 3, pp. 1974–1980, 2016.

[84] S. Clair and D. G. de Oteyza, "Controlling a chemical coupling reaction on a surface: Tools and strategies for on-surface synthesis," *Chemical Reviews*, vol. 119, no. 7, pp. 4717–4776, 2019.

[85] M. Treier, C. A. Pignedoli, T. Laino, R. Rieger, K. Müllen, D. Passerone, and R. Fasel, "Surface-assisted cyclodehydrogenation provides a synthetic route towards easily processable and chemically tailored nanographenes," *Nature Chemistry*, vol. 3, no. 1, pp. 61–67, 2010.

[86] A. Shiotari, T. Nakae, K. Iwata, S. Mori, T. Okujima, H. Uno, H. Sakaguchi, and Y. Sugimoto, "Strain-induced skeletal rearrangement of a polycyclic aromatic hydrocarbon on a copper surface," *Nature Communications*, vol. 8, no. 1, pp. 16089.1–16089.8, 2017.

[87] M. Bieri, M.-T. Nguyen, O. Gröning, J. Cai, M. Treier, K. Aït-Mansour, P. Ruffieux, C. A. Pignedoli, D. Passerone, M. Kastler, K. Müllen, and R. Fasel, "Two-dimensional polymer formation on surfaces: Insight into the roles of precursor mobility and reactivity," *Journal of the American Chemical Society*, vol. 132, no. 46, pp. 16669–16676, 2010.

[88] J. Björk, F. Hanke, and S. Stafström, "Mechanisms of halogen-based covalent self-assembly on metal surfaces," *Journal of the American Chemical Society*, vol. 135, no. 15, pp. 5768–5775, 2013.

[89] Y.-Q. Zhang, N. Kepčija, M. Kleinschrodt, K. Diller, S. Fischer, A. C. Papageorgiou, F. Allegretti, J. Björk, S. Klyatskaya, F. Klappenberger, M. Ruben,

and J. V. Barth, "Homo-coupling of terminal alkynes on a noble metal surface," *Nature Communications*, vol. 3, no. 1, pp. 1286.1–1286.8, 2012.

[90] M. Treier, C. A. Pignedoli, T. Laino, R. Rieger, K. Müllen, D. Passerone, and R. Fasel, "Surface-assisted cyclodehydrogenation provides a synthetic route towards easily processable and chemically tailored nanographenes," *Nature Chemistry*, vol. 3, pp. 61–67, 2011.

[91] M. Telychko, J. Su, A. Gallardo, Y. Gu, J. I. Mendieta-Moreno, D. Qi, A. Tadich, S. Song, P. Lyu, Z. Qiu, H. Fang, M. J. Koh, J. Wu, P. Jelínek, and J. Lu, "Strain-induced isomerization in one-dimensional metal–organic chains," *Angewandte Chemie International Edition*, vol. 58, no. 51, pp. 18591–18597, 2019.

[92] S. Kumar, J. M. Rosenberg, D. Bouzida, R. H. Swendsen, and P. A. Kollman, "The weighted histogram analysis method for free-energy calculations on biomolecules. i. the method," *Journal of Computational Chemistry*, vol. 13, no. 8, pp. 1011–1021, 1992.

List of Figures

List of Abbreviations

In alphabetical order

1D: One-dimensional

2D: Two-dimensional

4BrPhM: Tetrakis(4-bromophenyl) methane

4FPhM: Tetrakis(4-fluorophenyl) methane

AFM: Atomic force microscope

AM-AFM: Amplitude modulation atomic force microscope

CO: Carbon monoxide

CPD: Contact potential difference

DBDMN: 1,5-dibromo-2,6-dimethylnaphthalene

DFT: Density functional theory

DFT-D: Dispersion corrected density functional theory

DOS: Densities of states

EPS: Electrostatic potential surfaces

FM-AFM: Frequency modulation atomic force microscope

GGA: General gradient approximation

HEG: Homogeneous electron gas

HF: Hartree-Fock

HK: Hohenberg–Kohn

IETS: Inelastic electron tunnel microscopy

KPFM: Kelvin probe force microscopy

KS: Kohn-Sham

LCPD: Local contact potential diference

LDA: Local density approximation

LEED: Low energy electron diffraction

LJ: Lennard-Jones

LR: Long range

MD: Molecular dynamics

MM: Molecular mechanic

MOCs: Metal-organic chains

nc-AFM: Non-contact atomic force microscope

PP: Probe particle

PPAFM: Probe particle atomic force microscopy

QM: Quantum mechanic

QM/MM: Quantum mechanic/molecular mechanic

SPM: Scanning probe microscope

SR: Short range

STM: Scanning tunnel microscope

UHV: Ultra-high vacuum

WHAM: Weighted histogram analysis method

XC: Exchange and correlation

XPS: X-ray photoelectron spectroscopy

List of publications

- H. Fang †, **A. Gallardo** †, D. Dulal, Z. Qiu, J. Su, M. Telychko, H. Mahalingam, P. Lyu, Y. Han, Y. Zheng, Y. Cai, A. Rodin, P. Jelínek, J. Lu; Electronic Self-passivation of Single Vacancy in Black Phosphorus via a Controlled Ionization. *Accepted in Physical Review Letters*, 2022, available as: arXiv preprint arXiv:2107.03296.

  † These authors contributed equally to this work.

- K. Biswas, José I Urgel, Kun Xu, Ji Ma, A. Sánchez-Grande, P. Mutombo, **A. Gallardo**, K. Lauwaet, B. Mallada, B. de la Torre, A. Matěj, J. M. Gallego, R. Miranda, P. Jelínek, X. Feng, D. Écija; On-Surface Synthesis of a Dicationic Diazahexabenzocoronene Derivative on the Au (111) Surface. *Angewandte Chemie* 133 (48), 25755-25760, 2021.

- B. Mallada †, **A. Gallardo** †, M. Lamanec †, B. de la Torre, V. Špirko, P. Hobza, P. Jelinek; Real-space imaging of anisotropic charge of -hole by means of Kelvin probe force microscopy. *Science*, 374, 863-867, 2021.

  † These authors contributed equally to this work.

- Ch. Wäckerlin, **A. Gallardo**, A. Mairena, M. Baljozović, A. Cahlík, A. Antalík, J. Brabec, L. Veis, D. Nachtigallová, P. Jelínek, and K.-H. Ernst; On-Surface Hydrogenation of Buckybowls: From Curved Aromatic Molecules to Planar Non-Kekule Aromatic Hydrocarbons. *ACS Nano*, 14 (12), 16735–16742, 2020.

- P Procházka, M. A. Gosalvez, L. Kormoš, B. de la Torre, **A. Gallardo**, J. Alberdi-Rodriguez, T. Chutora, A. O. Makoveev, A. Shahsavar, A. Arnau, P. Jelínek, and J. Čechal; Multiscale Analysis of Phase Transformations in Self-Assembled Layers of 4, 4-Biphenyl Dicarboxylic Acid on the Ag (001) Surface. *ACS Nano*, 14 (6), 7269–7279, 2020.

- B. Mallada, Sh. Edalatmanesh, P. Lazar, J. Redondo, **A. Gallardo**, R. Zbořil, P. Jelínek, M. Švec, B. de la Torre; Atomic-Scale Charge Distribution Mapping of Single Substitutional p- and n-Type Dopants in Graphene. *ACS Sustain. Chem. Eng.*, 8 (8), 3437-3444 2020.

- Mohammed SG. Mohammed, L. Colazzo, **A. Gallardo**, J. A. Pomposo, P. Jelínek, D. G. de Oteyza; Steering alkyne homocoupling with on-surface synthesized metal–organic complexes. *Chemical Communications*, 56 (61), 8659-8662, 2020.

- M. Telychko †, J. Su †, **A. Gallardo** †, Y. Gu, J. I. Mendieta-Moreno, D. Qi, A. Tadich, S. Song, P. Lyu, Z. Qiu, H. Fang, M. J. Koh, J. Wu, P. Jelínek, J. Lu; Strain-Induced Isomerization in One-Dimensional Metal–Organic Chains. *Angewandte Chemie* 131 (51), 18764-18770, 2019.

  † These authors contributed equally to this work.

- L. Colazzo, M. SG. Mohammed, **A. Gallardo**, Z. M. Abd El-Fattah, J. A. Pomposo, P. Jelínek, D. G. de Oteyza; Controlling the stereospecific bonding motif of Au–thiolate links. *Nanoscale*, 11 (33), 15567-15575, 2019.

- **A. Gallardo**, J. Fanfrlík, P. Hobza, P. Jelínek; Nature of Binding in Planar Halogen–Benzene Assemblies and Their Possible Visualization in Scanning Probe Microscopy. *The Journal of Physical Chemistry C*, 123 (13), 8379–8386, 2018.

Appendix

Appended papers

1. Nature of binding in planar halogenbenzene assemblies and their possible visualization in scanning probe microscopy.

2. Real-space imaging of anisotropic charge of σ-hole by means of Kelvin probe force microscopy.

3. Strain-induced isomerization in one-dimensional metal–organic chains.

THE JOURNAL OF PHYSICAL CHEMISTRY C

Article

Cite This: J. Phys. Chem. C 2019, 123, 8379−8386

pubs.acs.org/JPCC

Nature of Binding in Planar Halogen−Benzene Assemblies and Their Possible Visualization in Scanning Probe Microscopy

Aurelio Gallardo,[†,‡] Jindrich Fanfrlík,[¶] Pavel Hobza,*[,¶,§] and Pavel Jelínek*[,†,§]

[†]Institute of Physics of the Czech Academy of Sciences, Cukrovarnická 10, 162 00 Prague, Czech Republic

[‡]Faculty of Mathematics and Physics, Charles University, V Holešovičkách 2, 180 00 Prague, Czech Republic

[¶]Institute of Organic Chemistry and Biochemistry of the Czech Academy of Sciences, Flemingovo nam. 2, 166 10 Prague, Czech Republic

[§]Regional Centre of Advanced Technologies and Materials, Palacký University, Šlechtitelů 27, 78371 Olomouc, Czech Republic

ABSTRACT: High-resolution scanning probe imaging of molecular structures on surfaces with functionalized tips provided the unprecedented spatial resolution. However, the origin of sharp intermolecular features often presented in high-resolution images of molecular assemblies is still under intensive debate. Originally, such features were considered as a direct observation of weak noncovalent bonds between molecules. Nevertheless, this interpretation was challenged and ascribed to an experimental artifact. To address this long-standing controversy, we provided theoretical analysis of intermolecular interaction and high-resolution imaging of halogen-substituted benzene assemblies deposited on metallic substrates, which were extensively studied experimentally. First, we show that formation of molecular assemblies made of C_6Br_6 and C_6F_6 on surfaces is driven by interplay between halogen and dispersive interaction. Next, for the C_6Br_6 and C_6F_6 assemblies on surface we analyze simulated high-resolution inelastic electron tunneling spectroscopy (IETS) and atomic force microscopy (AFM) images acquired with a CO-tip. Very good agreement with the experimental evidence allows us to unambiguously determine that the lateral bending of CO-tip due to Pauli repulsion is responsible for the intermolecular sharp edges. In addition, we discuss, why such sharp features should not be interpreted as the direct evidence of the signature of weak noncovalent bonds.

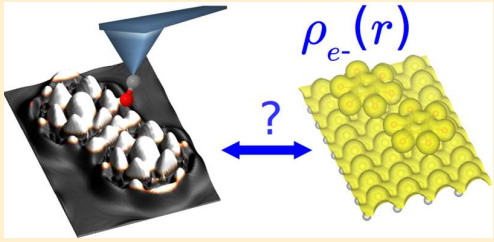

Halogen (X) bonding is a noncovalent interaction between two electronegative atoms, the halogen atom and an electron donor. The explanation of this counterintuitive interaction is based on the concept of σ-hole at halogen atom developed by Politzer and co-workers.[1−5] Electron density around halogen atom that is covalently bound to the more electronegative atom, mostly carbon, is not distributed uniformly. Besides the expected negative potential at the belt of the atom there exists also a narrow fragment of positive electrostatic potential called σ-hole. The σ-hole is localized at the top of the halogen[2] opposite to the covalent bond. The deficiency of electrons in the p orbital (sp hybridization does not exist in halogen atoms in a molecule) causes the presence of σ-hole and its magnitude increases with halogen atomic number. According to this concept, fluorine mostly does not have a σ-hole, while iodine has a significant σ-hole. Originally it was believed that electrostatic interactions represent the major source of attraction in X-bonding, but it was also claimed that the orbital mixing (charge transfer) was prominent contribution to this stabilization as well. It was recently shown that the reduced electron density in the region of σ-hole leads to a smaller Pauli repulsion (so-called polar flattening), which allows the interacting atoms to come closer than their sum of van der Waals radii. Such a close contact between two heavy atoms with high polarizabilities leads to strong dispersion interaction, representing one of the most important stabilizing component in weaker X-bonds.[6,7] It is worth to emphasized that σ-hole can be characterized by maximum of molecular electrostatic potential in the 0.001 au density isosurface ($V_{s,max}$). The $V_{s,max}$ value of the σ-hole can be tuned by substitution of the electron-withdrawing group near the X atom or switching X by a more polarizable (less electronegative) atom to gain the enhancement of the σ-hole.[8] Introduction of electron-donating group or less polarizable X atom gives the opposite effect.

Introduction to SPM Imaging. A discovery of a proper functionalization of scanning probe with a flexible moiety allowed to reach the unprecedented spatial resolution of individual molecules in ultrahigh vacuum (UHV) atomic force microscopy (AFM),[9] scanning tunneling microscopy (STM)[10] and also inelastic tunneling electron spectroscopy (IETS).[11] Namely, it enabled to resolve unambiguously distinct molecular structures on surfaces[12] revealing bond order of individual covalent carbon−carbon bonds,[13] identification of

Special Issue: Hans-Joachim Freund and Joachim Sauer Festschrift

Received: October 2, 2018
Revised: November 16, 2018
Published: December 5, 2018

DOI: 10.1021/acs.jpcc.8b09631
J. Phys. Chem. C 2019, 123, 8379−8386

different products of chemical on-surface reactions,[14−18] reconstruction of the electrostatic potential of individual molecules[19] or discrimination of distinct molecular spin states.[20] In such high-resolution images, skeleton of organic molecules is represented by a network of sharp edges mimicking the strong covalent or dative bonds between atoms of given molecule.[12,21,22] Besides that, sharp edges are sometimes also observed in between molecules forming closed packed molecular assemblies.[10,23,24]

It has been shown that the high-resolution contrast can be achieved simultaneously in all three AFM/STM/IETS modes, demonstrating the common underlying imaging mechanism.[25] Even more, the mechanism of the sharp contrast is theoretically well understood now in terms of a lateral relaxation of a so-called flexible probe particle attached to a metallic tip. This lateral bending resulting from combination of dispersion, electrostatic, and Pauli repulsion acting between probe and sample is the main factor providing the high spatial resolution in all three channels: AFM,[21,26,27] STM,[28] and IETS.[25,29] In far tip−sample distances, the submolecular contrast is never observed, because interaction between CO-tip and sample is driven by attractive dispersion and electrostatic forces. These interactions are typically weak causing negligible lateral distortion of CO-tip.[21,22] To achieve the submolecular resolution of molecules on surface one has to bring CO-tip in very close to surface. Sharp intermolecular and intramolecular edges presented in high-resolution AFM images always accompanied by enhancement of the frequency shift. This means that the functionalized CO-tip experiences repulsive forces because of the Pauli repulsion. Therefore, the sharp intermolecular and intramolecular edges are intimately connected to the repulsive forces acting between CO-tip and sample.

Nowadays, there is common consensus on one-to-one correspondence between intramolecular sharp edges and strong covalent bonds forming molecular skeleton. On the other hand, there is ongoing discussion about the interpretation of the origin of intermolecular sharp edges frequently observed in between molecules. Originally, these sharp intermolecular features were assigned to the direct visualization of weak intermolecular hydrogen[23] or halogen[30] bonds. However, this interpretation to directly visualize hydrogen bonds has been subject of an extended discussion in the community, as the sharp edges were also observed in places where there should not be any hydrogen bonds formed.[21,31−33] This dispute helps the community to advance in detailed understanding of the imaging mechanism of the technique.[22] On the basis of the probe particle model,[21,29] it has been demonstrated that the sharp edges can result from lateral bending of flexible probe at saddle points of the potential energy surfaces. The shape of the potential energy surface is defined by interaction energy between the chemically inert probe and inspected molecule on surface including dispersion, electrostatic and Pauli repulsion.

Despite these advances in our understanding of the imaging mechanism, there are still some tendencies to interpret the intermolecular sharp edges as the direct visualization of the intermolecular bonds.[11,23,30,34] The possibility of the direct visualization of noncovalent bonds may create high expectation in different fields including chemistry and biology. Namely, this interpretation may be seen as a direct proof of the covalent character of halogen[35−38] or hydrogen[39−43] bonds, which is under an intensive discussion in chemical community. Thus, we think that it deserves detailed explanation of the bonding mechanism and its imaging.

The aim of this manuscript is to address the fundamental question: Can these weak intermolecular bonds be seen by scanning probe microscopy? For this, we will provide an extensive theoretical analysis of interaction and imaging mechanism of molecular assemblies of C_6Br_6 and C_6F_6 on metallic substrate, which has been investigated experimentally in details by Han et al.[30] We believe that the direct comparison between theoretical and experimental evidence allows us to provide conclusive evidence about the origin of the sharp intermolecular features and solve the long-standing question.

This paper is organized in the following way. First, we will discuss the character of the interaction between free-standing C_6Br_6 or C_6F_6 dimers with accurate but computationally demanding quantum chemistry methods. We critically compare such high-level calculations with standard density functional theory (DFT) calculations. The good agreement between the methods justifies usage of the DFT calculations in more realistic systems including metallic surface. Next, we will present simulations of high resolution AFM/IETS images of selected molecular systems on surface and compare them critically with the experimental evidence. The good agreement allows us to unambiguously identify the imaging mechanism responsible for the presence of intermolecular sharp edges. Finally, we will bring an argument which rules out the possibility of direct visualization of the noncovalent bonds.

METHODS

DFT Calculations. DFT calculations were performed using the Fritz Haber Institute *ab initio* molecular simulations package (FHI-AIMS).[44] We carried out all-electron, full-potential calculations with the hybrid *hse03* potential.[45] Van der Waals corrections were included by means of the Tkatchenko−Scheffler method.[46] In all the calculations, a vacuum section thicker than 30 Å was included in the direction perpendicular to the surface or the molecule plane. To make the hybrid DFT calculations tractable, we employ light wave functions and a gamma point, checking first that it does not implies a loose of precision. Namely, we checked that there is no significant difference between results (binding energies, geometries etc.) obtained with light and tight basis sets using a standard GGA-PBE functional. The energy convergence criteria was set on 10^{-5} eV, and the interaction energy was calculated as the energy difference of the dimer and two times the monomer:

DFT-SAPT. The interaction energy was decomposed by using the density functional theory-based symmetry-adapted perturbation theory (DFT-SAPT).[47] The DFT part was treated using the LPBE0AC functional and the aug-cc-pVDZ basis set. This combination of the functional and the basis set has been shown to provide a reasonably good description of electrostatic and induction energies, but the dispersion term is underestimated by approximately 10−20%. We have thus calculated DFT-SAPT/CBS (using two-point extrapolation methods with the aug-cc-pVDZ and aug-cc-pVTZ basis sets) for the C_6Br_6 dimer and the resulting scaling factor of 1.137 was used for the dispersion energy in all studied systems in order to obtain results comparable with CBS data. The calculations were done by Molpro 10.

MP2.5. MP2.5[48] with the complete basis set (CBS) was calculated as the sum of the MP2/CBS and the scaled MP3 energy contribution (the scaling factor of 0.5) with the aug-cc-

DOI: 10.1021/acs.jpcc.8b09631
J. Phys. Chem. C 2019, 123, 8379−8386

pVDZ basis set. For MP2/CBS, an extrapolation from cc-pVTZ to cc-pVQZ was used.[49] Counterpoise corrections for the basis set superposition error (BSSE) and resolution of identity (RI) approximations were used. Computations were performed by Turbomole (7.0)[50] and Cuby4.[51]

Simulations of SPM Images. The AFM/IETS images were simulated using the probe particle model.[21,29] Parameters of a probe particle were mimicking a CO-tip, represented as a monopole, with a stiffness of 0.24 N·m^{-1} and a charge of −0.05 e. The electrostatic force was included in the calculation, using the Hartree potential calculated with the DFT techniques already described in subsection. The IETS images where simulated at a bias of 1.5 mV. We used a value of the cutoff radii for the Lenard-Jones potential of 1.908 for the carbon, 1.750 for the fluorine and 2.100 for the bromine. The AFM images are calculated with a typical qPlus sensor parameters, oscillation amplitude A = 100 pm, sensor stiffness k = 3600 N/m, and eigenfrequency f_o = 30 kHz.

RESULTS AND DISCUSSION

First we performed high-level quantum chemistry calculations only for free-standing dimers, i.e., without considering the surface. We believe that surface affects various dimers in a systematic way what means that relative values of dimer interaction energies as well as their energy components will not be influenced. In the DFT simulations the Ag surface was, however, fully considered. We compared different dimer configurations of C_6Br_6 and C_6F_6 molecules in gas phase to understand the origin of the weak intermolecular interactions driven by dispersion and halogen bond interactions. To determine the presence of halogen bonds originated by existence of the σ-holes, we first computed the electrostatic potential (ESP) projected on the density surfaces of the C_6F_6 (Figure 1a) and C_6Br_6 (Figure 1b) gas phase molecules. The

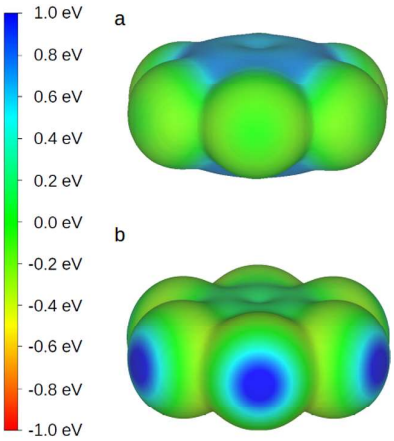

Figure 1. Computed ESP on 0.001 bohr^{-3} density isosurface for (a) C_6F_6 and (b) C_6Br_6 molecules.

Br atoms in the C_6Br_6 molecule presents a strong σ-hole, with a maximum value of the potential ($V_{s,max}$) of 1.17 eV. The maximum value of the potential in the density isosurface is a well-known figure of merit in the study of the halogen compounds. In contrast, the F atoms in the C_6F_6 molecule do not show any positive σ-hole but only a region that is slightly less negative ($V_{s,max}$ = −0.04 eV) that the surrounding belt ($V_{s,min}$ = −0.15 eV). This is not surprising since the σ-hole at an halogen atom is diminished by the electronegativity difference with the atom that it is covalently bonded with. Therefore, we can conclude that only in the case of C_6Br_6 molecules can the halogen bond play a significant role.

To clarify further the interaction mechanism between the molecules, we studied different configurations of the C_6F_6 and C_6Br_6 dimers that are shown in Figure 2. First, the

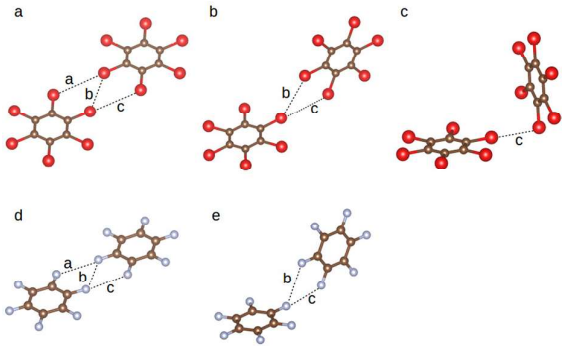

Figure 2. Structures of the gas phase dimers studied: (a) planar C_6Br_6 dimer, (b) rotated C_6Br_6 dimer, (c) T-shape C_6Br_6 dimer, (d) planar C_6F_6 dimer, and (e) rotated C_6F_6 dimer.

performance of the DFT technique should be investigated. Table 1 shows that the relative values of DFT interaction energies (3rd column) agree reasonably well with benchmark MP2.5 and DFT-SAPT (2nd and 5th column) values. The energy decomposition, which is essential for explaining the nature of halogen bonding, will be in the next part based on DFT-SAPT energies.

The rotated structures (Figure 2, parts b and e) were considered because the original planar dimers had symmetrical dihalogen bonds. In the case of C_6Br_6, we also included the one we call T-shape dimer (Figure 2c) as an example of a perfectly oriented halogen bond. In the case of C_6Br_6, the most stable configuration is the T-shape. Indeed, looking at energy decomposition performed with DFT-SAPT technique, we see that the interaction is mainly dispersion and electrostatic (i.e., 68 and 24% of the sum of attractive energy terms, respectively). The electrostatic/dispersion energy ratio slightly decreases when going from T-shape to planar, because the halogen bonding is weaker in the last one. In the case of the C_6F_6, the electrostatic energy plays a considerably less important role than in the bromine compounds (i.e., bellow 15% of the total attractive energy). This means that, as we expected because of the absence of σ-hole in the monomer, C_6F_6 polymers do not show halogen bonds.

Geometrically, we observe that Br···Br distance in the planar structure is larger than twice the van der Waals radius of the Br atom. Also the C−X−X angles, where X is a halogen atom, are far from the 180° and 90° expected for a perfect halogen bond. The bond geometry and energy decomposition make us think that the interactions of the planar C_6Br_6 dimer should be instead defined as nonspecific dispersion-driven contacts than specific halogen-bonding interactions. Distances for the dimers are given in Table 2.

In the case of C_6F_6 dimer, the decomposition of the DFT-SAPT interaction energies, see Table 1, reveals the dominance of the dispersion energy, which is 1 order of magnitude larger than the electrostatic interaction. So we can conclude that the halogen bonding does not play a significant role in molecular

DOI: 10.1021/acs.jpcc.8b09631
J. Phys. Chem. C 2019, 123, 8379−8386

Table 1. Energy Decomposition of the Dimers Described in Figure 2

	MP2.5/CBS	DFT-HSE03	DFT-SAPT				
dimer	ΔE (eV)	ΔE (eV)	ΔE (eV)	E_{elec} (eV)	E_{ind} (eV)	E_{disp} (eV)	E_{exch} (eV)
planar C_6Br_6	−0.1376	−0.0917	−0.1243	−0.0576	−0.0189	−0.1832	0.1354
rotated C_6Br_6	−0.1023	−0.0707	−0.0946	−0.0482	−0.0133	−0.1393	0.1062
T-shape C_6Br_6	−0.1432	−0.1082	−0.1286	−0.0649	−0.0224	−0.1793	0.1385
planar C_6F_6	−0.0305	−0.0383	−0.0322	−0.0069	−0.0013	−0.0714	0.0473
rotated C_6F_6	−0.0301	−0.0395	−0.0318	−0.0095	−0.0009	−0.0563	0.0353

Table 2. Distances Described in Figure 2

dimer	a (Å)	b (Å)	c (Å)
planar C_6Br_6	4.26	3.91	4.27
rotated C_6Br_6	–	3.91	4.27
T-shape C_6Br_6	–	–	3.51
planar C_6F_6	3.02	3.11	3.01
rotated C_6F_6	–	3.11	3.01

assemblies of C_6F_6. This directly puts in question the interpretation of intermolecular features observed in C_6F_6 molecular assemblies such as the evidence of the presence of the halogen bonding.[30]

Next, we will discuss the origin of the intermolecular high-resolution contrast observed experimentally in C_6F_6 and C_6Br_6 molecular assemblies on metallic surface by Han et al.[30] We carried out total energy DFT simulations of planar monomers and dimers of C_6Br_6 on a Ag(110) surface. Additionally, we also considered a cluster consisting of seven C_6F_6 molecules in gas phase to make the calculations computationally tractable. To better understand the character of the interaction between molecules in the planar configuration, we can look at the charge density distribution on the ESP surface (Figure 3 and

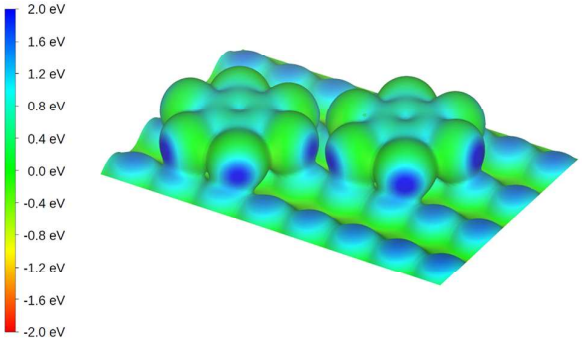

Figure 3. Computed ESP on 0.001 bohr^{-3} density isosurface for the C_6Br_6 dimer on a Ag(110) substrate.

4). In both cases, we do not observe formation of bond charge in between individual molecules as expected from the previous theoretical analysis of the free-standing dimers. Figure 5 displays the differential densities of C_6Br_6 dimer on Ag(110) surface revealing a slight polarization of individual molecules C_6Br_6 after deposition on Ag(110) surface but, more importantly, the absence of induced bonding charge between C_6Br_6 molecules forming a dimer on Ag(110) surface. However, this is an important point for the discussion of the origin of the sharp intermolecular edges. We will extend this argument later, when we will discuss the possibility of the direct imaging of weak noncovalent bonds by scanning probe microscopy.

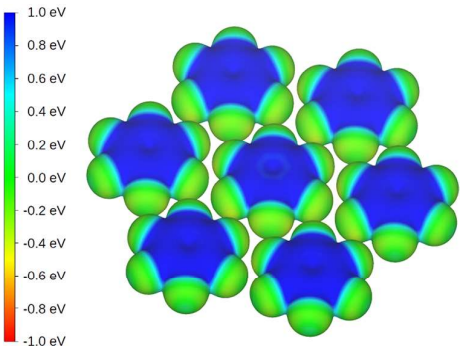

Figure 4. Computed ESP on 0.001 bohr^{-3} density isosurface for a seven C_6F_6 molecule cluster in the gas phase.

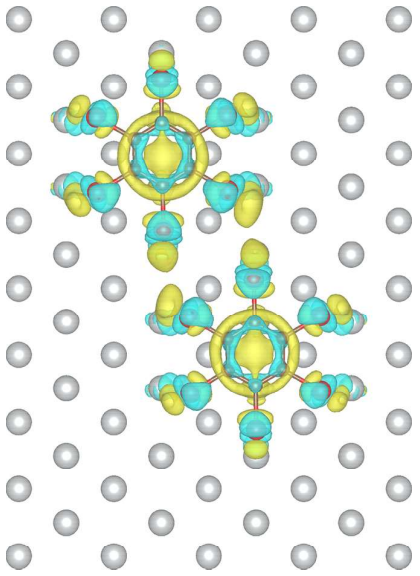

Figure 5. Computed differential density isosurface plotted at 0.006 bohr^{-3} of the C_6Br_6 dimer on a Ag(110) substrate. The differential density has been obtained by subtracting from the total density of the whole system the densities of clean Ag(110) substrate and the two individual C_6Br_6 molecules.

We simulated AFM and IETS images of a C_6F_6 cluster and C_6Br_6 monomer and dimer on silver using the probe particle code.[21,29] The results are displayed in Figures 6, 7, 8, and 9, showing IETS and AFM images together with a corresponding map of the probe particle lateral position due to the lateral bending for particular tip−sample distance. The simulated IETS images match very well the experimental results obtained by Han et al.[30] In the case of a single C_6Br_6 molecule, we reproduce sharp edges located in between individual bromine atoms, which were also observed experimentally. Apparently

DOI: 10.1021/acs.jpcc.8b09631
J. Phys. Chem. C 2019, 123, 8379−8386

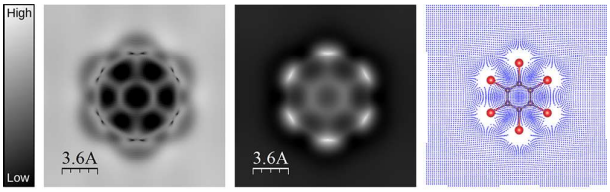

Figure 6. Simulated images of IETS (a) and Δf (b) and CO-tip position (c) of AFM operation of a C_6Br_6 molecule on a Ag(110) substrate. Q_{tip} = −0.05 e, and A = 100 pm.

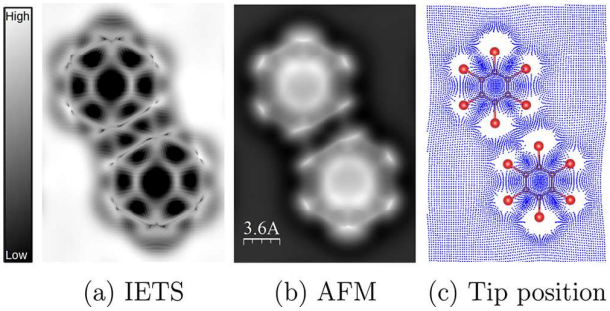

Figure 7. Simulated images of IETS (a) and Δf (b) and CO-tip position (c) of AFM operation of a C_6Br_6 dimer on a Ag(110) substrate. Q_{tip} = 0.5 e, and A = 100 pm.

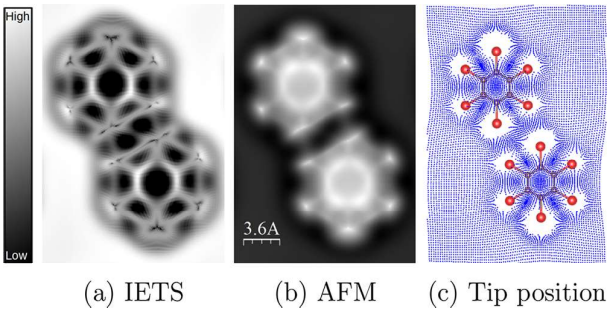

Figure 8. Simulated images of IETS (a) and Δf (b) and CO-tip position (c) of AFM operation of a C_6Br_6 dimer on a Ag(110) substrate. Q_{tip} = 0.0 e, and A = 100 pm.

these sharp edges are not related to any intermolecular bond, but they are a consequence of the saddle point of the potential energy surface feeling by the probe particle when it approaches close to the molecule.

In the case of the C_6Br_6 dimer (Figure 7, parts a and b), we found three sharp edges presented in between the molecules in perfect agreement with the experiments, which were originally ascribed to the presence of the halogen bonds. But analyzing carefully the probe particle position (Figure 7c) we find that the position of sharp edges corresponds to places where the probe particle suffers substantial lateral relaxation.[21,22] Now the question is what is the origin of this pronounced lateral relaxation of the probe particle in these particular places. The lateral displacement is the result of efforts to minimize potential energy of the probe particle when interacts with the sample;[21] i.e., the probe particle located in a saddle point of the potential energy surface tends to slide laterally to decreases its potential energy. The lateral movement is transduced in a abrupt change in observable signal, giving rise to the sharp feature in resulting image. On the other hand, the absence of the bond charge in between the molecules, see Figure 3, rules out the possibility that the sharp edges are direct consequence of the Pauli repulsion between the bond charge and density of the probe particle. Still, one can argue that the presence of electrostatic interaction such as halogen bonding, can push the probe particle away of that region, giving rise to a saddle point. Consequently, this behavior will be reflected in the SPM images as a sharp line too, similar to features ascribed to covalent bonds.

To rule out this hypothesis first, we calculated the same IETS image, but excluding the electrostatic interaction from the interaction between the probe particle and the dimer, see Figure 8. The contrast almost does not change showing very similar intermolecular sharp edges. We can see that the appearance of the intermolecular sharp edges in the dimer are independent of the electrostatic interaction.

Second, we also calculated images of the C_6F_6 cluster (Figure 9), where the binding mechanism is mostly driven by dispersion interaction and σ-hole electrostatic interaction is negligible, as discussed above (Table 1). In both AFM and IETS images of the C_6F_6 cluster, we observe the same kind of sharp intermolecular edges, which coincide exactly with places where the probe particle undergoes substantial lateral bending. These two observations clearly indicates that the local electrostatic forces between the probe particle and σ-hole or

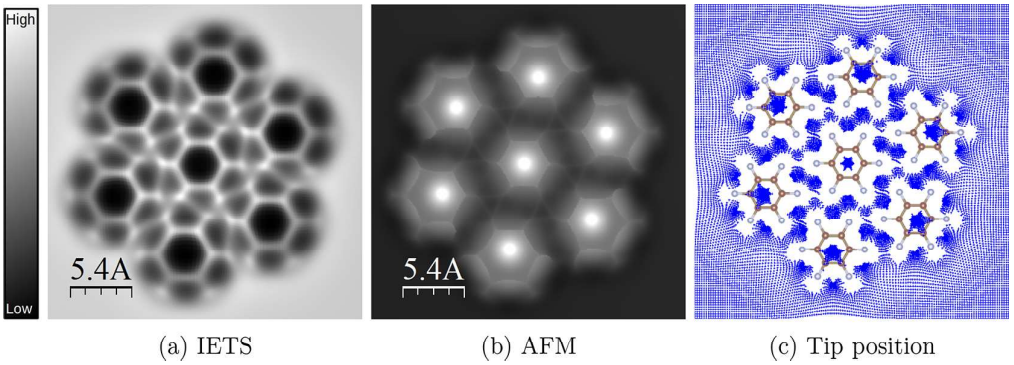

Figure 9. Simulated images of IETS (a) and Δf (b) and CO-tip position (c) of AFM operation of a C_6F_6 molecules cluster in the gas phase. Q_{tip} = −0.05, and A = 100 pm.

DOI: 10.1021/acs.jpcc.8b09631
J. Phys. Chem. C 2019, 123, 8379−8386

induced charge density cannot explain the origin of the intermolecular sharp edges. Instead, they can be ascribed to proximity effect of nearest atoms, where the lateral bending of the probe particle is driven by Pauli repulsion between electron densities of probe particle and the nearest frontier atoms of adjacent molecules. Similarly, the sharp edges can be observed without presence of any apparent bond, as it was already pointed out by Pavliček et al.[33] Consequently, the appearance of the intermolecular sharp edges only reflects saddle points in the potential energy surfaces, but it is not the direct evidence of any noncovalent bond.

One can also argue that the proximity of CO-tip may cause additional density polarization in the tunneling junction and consequently slightly changes the potential energy landscape. The effect of the polarization by the proximity of CO-tip is not included in the probe particle model. To capture this effect on the AFM imaging, it would require one to carry out a large number of fully converged total energy DFT calculations mimicking the CO-tip approach toward the surface. Such simulations carried on distinct molecular system[52] revealed only small induced charge densities on CO-tip and molecule deposited on metallic surface, order of magnitudes lower than in the case of the covalent bonding. Even more, the induced electrostatic interaction between functionalized tip and molecule on surface will be always attractive, by definition, having the same character as dispersive forces. However, the sharp intermolecular edges appear in very close distances, where the Pauli repulsion dominates. It means that the induced polarization by the proximity of CO-tip cannot substantially influence the high-resolution imaging. Indeed, very good agreement between simulated and experimental AFM images using PP-AFM model indicates that this effect is negligible. On the basis of these arguments, we think, that effect can be omitted in interpretation of high-resolution imaging mechanism.

Let us now discuss the general possibility to image weak intermolecular bonds in high-resolution SPM images with functionalized tips. First, we should highlight the difference between strong covalent/dative bonds and weak intermolecular hydrogen, halogen, and dispersion bonding. The formation of covalent and dative bonds is accompanied by strong rehybridization of electronic states of the constituting atoms, establishing resonance bonding and antibonding states in between the atoms. This gives rise to strong localization of electron density, a bond charge, in between the atoms. This bond charge can be biased toward one of the atoms with larger electronegativity, but always strongly localized in between two atoms. This strong localization of the bond charge makes the bond very directional and rigid.

The strongly spatially localized bond charge has also very important consequences on the high-resolution scanning probe imaging. The presence of the bond charge enhances locally the Pauli repulsion and also the electrostatic interaction acting on the probe particle. Consequently, a saddle point in the potential energy surface is locally formed in the place of the bond charge. This gives rise in close tip−sample distances to a lateral bending of the probe particle, which is manifested by the presence of sharp edges in the signal detected by the microscope. From this point of view, one-to-one correspondence between a sharp edge and covalent/dative bond is well justified.

However, the same argument of the localized charge bond cannot be adopted for noncovalent intermolecular interactions, because of completely different binding mechanism. The origin of noncovalent hydrogen, halogen, or dispersion interactions is attributed to electrostatic force with a negligible contribution of hybridization of electronic states. In the case of the hydrogen bond, the electrostatic force originates from positively polarized hydrogen atoms interacting with negative charge (frequently represented by a lone pair electronic cloud) residing on different atom involved in the hydrogen bonding.[53] In the case of the halogen bond, the electrostatic force is originated by presence of positively charged σ-hole region placed on halogen atom.[2,3] The distance and strength of the σ-hole electrostatic interaction results of reorganization of halogen electron density induced by covalent bond between halogen and electronegative atom. Consequently the positive σ-hole attracts the negatively charged electron clouds on different atoms, giving rise to so-called halogen bonds.

Both hydrogen and halogen interactions are accompanied by omnipresent always attractive dispersion forces, which originate from coulombic interaction of correlated fluctuating densities on neighbor atoms. The dispersion interaction is typically stronger in halogen interactions than in hydrogen interactions. This is simply because of the fact that in halogen bond two heavy atoms with high polarizability are in close contact. This finding is supported by a recently published paper,[35] where it is shown that there is no need to involve the charge transfer term in explaining the bonding in the halogen bond.

Importantly, the formation of the localized bond charge between atoms involved in the bonding is negligible in all noncovalent interactions. Therefore, these interactions have nonlocal character driven by the electrostatic field created by the charge density polarization of the atoms involved in the bonding with negligible bond charge. From this point, it is very difficult to justify the direct correspondence to highly localized sharp edges to nonlocal electrostatic interaction. Instead these sharp edges result from a proximity effect, which can be seen as problem of penetration of the hard sphere (probe particle on tip) in between two other spheres (surface atom involved in a noncovalent bonding). When the probe scans an intermolecular region in close distances in between two atoms interacting via hydrogen/halogen, it senses a repulsive Pauli interaction due to the overlap of wave functions. This repulsion can be further enhanced by electrostatic interaction if the probe particle on tip apex and surface atoms have the same charge. This repulsion is released quickly, when the tip moves from region connecting two surface atoms, because of the exponential decay of Pauli repulsion with distance. This gives rise to a saddle point in potential energy surface, which appears as a sharp edge in the high-resolution scanning probe images. However, this very local feature does not have any relation to nonlocal electrostatic fields driving noncovalent interactions.

AUTHOR INFORMATION

Corresponding Authors

*(P.J.) E-mail: jelinekp@fzu.cz.

*(P.H.) E-mail: pavel.hobza@uochb.cas.cz.

ORCID

Aurelio Gallardo: 0000-0001-6544-7637

Pavel Hobza: 0000-0001-5292-6719

Pavel Jelínek: 0000-0002-5645-8542

DOI: 10.1021/acs.jpcc.8b09631
J. Phys. Chem. C 2019, 123, 8379−8386

Notes

The authors declare no competing financial interest.

■ ACKNOWLEDGMENTS

P.J. and A.G. acknowledge the support by GAČR, Grant No. 18-09914S, the Ministry of Education of the Czech Republic, Grant LM2015087, and the Czech Academy of Sciences through a Praemium Academiae award. This work was supported by Operational Programme Research, Development and Education financed by European Structural and Investment Funds and the Czech Ministry of Education, Youth and Sports (Projects No. SOLID21 - CZ.02.1.01/0.0/0.0/16_019/0000760). This work was part of the Research Project RVO: 61388963 of the Institute of Organic Chemistry and Biochemistry, Czech Academy of Sciences (J.F., P.H.) This work was also supported by the Ministry of Education, Youth and Sports for the Large Infrastructures for Research, experimental Development and Innovations project "IT4Innovations National Supercomputing Center - LM2015070" as well as Project LO1305.

■ REFERENCES

(1) Murray, J. S.; Lane, P.; Politzer, P. A Predicted New Type of Directional Noncovalent Interaction. *Int. J. Quantum Chem.* **2007**, *107*, 2286−2292.
(2) Clark, T.; Hennemann, M.; Murray, J. S.; Politzer, P. Halogen Bonding: The σ-Hole. *J. Mol. Model.* **2007**, *13*, 291−296.
(3) Politzer, P.; Lane, P.; Concha, M. C.; Ma, Y.; Murray, J. S. An Overview of Halogen Bonding. *J. Mol. Model.* **2007**, *13*, 305−311.
(4) Politzer, P.; Murray, J. S.; Concha, M. C. σ-Hole Bonding Between like Atoms; a Fallacy of Atomic Charges. *J. Mol. Model.* **2008**, *14*, 659−665.
(5) Murray, J. S.; Lane, P.; Politzer, P. Expansion of the σ-Hole Concept. *J. Mol. Model.* **2009**, *15*, 723−729.
(6) Tsuzuki, S.; Sato, N. Origin of Attraction in Chalgogen-Nitrogen Interaction of 1,2,5- Chalcogenadiazole Dimers. *J. Phys. Chem. B* **2013**, *117*, 6849−6855.
(7) Řezáč, J.; de la Lande, A. On the Role of Charge Transfer in Halogen Bonding. *Phys. Chem. Chem. Phys.* **2017**, *19*, 791−803.
(8) Riley, K. E.; Murray, J. S.; Fanfrlík, J.; Řezáč, J.; Solá, R. J.; Concha, M. C.; Ramos, F. M.; Politzer, P. Halogen Bond Tunability I: The Effects of Aromatic Fluorine Substitution on the Strengths of Halogen-Bonding Interactions Involving Chlorine, Bromine, and Iodine. *J. Mol. Model.* **2011**, *17*, 3309−3318.
(9) Gross, L.; Mohn, F.; Moll, N.; Liljeroth, P.; Meyer, G. The Chemical Structure of a Molecule Resolved by Atomic Force Microscopy. *Science* **2009**, *325*, 1110−1114.
(10) Kichin, G.; Weiss, C.; Wagner, C.; Tautz, F.; Temirov, R. Single Molecule and Single Atom Sensors for Atomic Resolution Imaging of Chemically Complex Surfaces. *J. Am. Chem. Soc.* **2011**, *133*, 16847−16851.
(11) Chiang, C.; Xu, C.; Han, Z.; Ho, W. Real-Space Imaging of Molecular Structure and Chemical Bonding by Single-Molecule Inelastic Tunneling Probe. *Science* **2014**, *344*, 885−888.
(12) Gross, L.; Moll, N.; Meyer, G.; Ebel, R.; Abdel-Mageed, W.; Jaspars, M.; et al. Organic Structure Determination Using Atomic-resolution Scanning Probe Microscopy. *Nat. Chem.* **2010**, *2*, 821−825.
(13) Gross, L.; Mohn, F.; Moll, N.; Schuler, B.; Criado, A.; Guitian, E.; Pena, D.; Gour- don, A.; Meyer, G. Bond-Order Discrimination by Atomic Force Microscopy. *Science* **2012**, *337*, 1326−1329.
(14) de Oteyza, D.; Gorman, P.; Chen, Y.-C.; Wickenburg, S.; Riss, A.; Mowbray, D.; Etkin, G.; Pedramrazi, Z.; Tsai, H.-Z.; Rubio, A.; et al. Direct Imaging of Covalent Bond Structure in Single-Molecule Chemical Reactions. *Science* **2013**, *340*, 1434−1437.
(15) Ruffieux, P.; Wang, S.; Yang, B.; Sánchez-Sánchez, C.; Liu, J.; Dienel, T.; Talirz, L.; Shinde, P.; Pignedoli, C.; Passerone, D.; et al. On-Surface Synthesis of Graphene Nanoribbons with Zigzag Edge Topology. *Nature* **2016**, *531*, 489−492.
(16) Kocić, N.; Liu, X.; Chen, S.; Decurtins, S.; Krejčí, O.; Jelínek, P.; Repp, J.; Liu, S.-X. Control of Reactivity and Regioselectivity for On-Surface Dehydrogenative Aryl−Aryl Bond Formation. *J. Am. Chem. Soc.* **2016**, *138*, 5585−5593.
(17) Schuler, B.; Fatayer, S.; Mohn, F.; Moll, N.; Pavliček, N.; Meyer, G.; Pena, D.; Gross, L. Reversible Bergman Cyclization by Atomic Manipulation. *Nat. Chem.* **2016**, *8*, 220−224.
(18) Stetsovych, O.; Švec, M.; Vacek, J.; Chocholoušová, J. V.; Jančařík, A.; Rybáček, J.; Kosmider, K.; Stará, I. G.; Jelínek, P.; Starý, S. From Helical to Planar Chirality by OnSurface Chemistry. *Nat. Chem.* **2017**, *9*, 213−218.
(19) Hapala, P.; Švec, M.; Stetsovych, O.; van der Heijden, N.; Ondracek, M.; van der Lit, J.; Mutombo, P.; Swart, I.; Jelínek, P. Mapping the Electrostatic Force Field of Single Molecules from High-Resolution Scanning Probe Images. *Nat. Commun.* **2016**, *7*, 11560.
(20) de la Torre, B.; Švec, M.; Hapala, P.; Redondo, J.; Krejčí, O. c. v.; Lo, R.; Manna, D.; Nachtigallova, D.; Tuček, J.; Blonski, P.; et al. Non-covalent Control of Spin-state in Metal-organic Complex by Positioning on N-doped Graphene. *Nat. Commun.* **2018**, *9*, 2831.
(21) Hapala, P.; Kichin, G.; Wagner, C.; Tautz, F. S.; Temirov, R.; Jelínek, P. Mechanism of High-Resolution STM/AFM Imaging with Functionalized Tips. *Phys. Rev. B: Condens. Matter Mater. Phys.* **2014**, *90*, No. 085421.
(22) Jelínek, P. High Resolution SPM Imaging of Organic Molecules With Functionalized Tips. *J. Phys.: Condens. Matter* **2017**, *29*, 343002.
(23) Zhang, J.; Chen, P.; Yuan, B.; Ji, W.; Cheng, Z.; Qiu, X. Real-Space Identification of Intermolecular Bonding with Atomic Force Microscopy. *Science* **2013**, *342*, 611−614.
(24) Sweetman, A.; Jarvis, S.; Sang, H.; Lekkas, I.; Rahe, P.; Wang, Y.; Wang, J.; Champ- ness, N.; Kantorovich, L.; Moriarty, P. Mapping the Force Field of a Hydrogen-Bonded Assembly. *Nat. Commun.* **2014**, *5*, 3931.
(25) de la Torre, B.; Švec, M.; Foti, G.; Krejčí, O.; Hapala, P.; Garcia-Lekue, A.; Frederiksen, T.; Zbořil, R.; Arnau, A.; Vázquez, H.; et al. Submolecular Resolution by Variation of the Inelastic Electron Tunneling Spectroscopy Amplitude and its Relation to the AFM/STM Signal. *Phys. Rev. Lett.* **2017**, *119*, 166001.
(26) Moll, N.; Gross, L.; Mohn, F.; Curioni, A.; Meyer, G. A Simple Model of Molecular Imaging With Noncontact Atomic Force Microscopy. *New J. Phys.* **2012**, *14*, No. 083023.
(27) Guo, C.-S.; Van Hove, M. A.; Ren, X.; Zhao, Y. High-Resolution Model for Noncontact Atomic Force Microscopy with a Flexible Molecule on the Tip Apex. *J. Phys. Chem. C* **2015**, *119*, 1483−1488.
(28) Krejčí, O.; Hapala, P.; Ondráček, M.; Jelínek, P. Principles and Simulations of High-Resolution STM Imaging With a Flexible Tip Apex. *Phys. Rev. B: Condens. Matter Mater. Phys.* **2017**, *95*, No. 045407.
(29) Hapala, P.; Temirov, R.; Tautz, F. S.; Jelínek, P. Origin of High-Resolution IETS-STM Images of Organic Molecules with Functionalized Tips. *Phys. Rev. Lett.* **2014**, *113*, 226101.
(30) Han, Z.; Czap, G.; Chiang, C.-l.; Xu, C.; Wagner, P. J.; Wei, X.; Zhang, Y.; Wu, R.; Ho, W. Imaging the Halogen Bond in Self-Assembled Halogenbenzenes on Silver. *Science* **2017**, *358*, 206−210.
(31) Hämäläinen, S.; van der Heijden, N.; van der Lit, J.; den Hartog, S.; Liljeroth, P.; Swart, I. Intermolecular Contrast in Atomic Force Microscopy Images without Intermolecular Bonds. *Phys. Rev. Lett.* **2014**, *113*, 186102.
(32) Kawai, S.; Sadeghi, A.; Xu, F.; Peng, L.; Orita, A.; Otera, J.; Goedecker, S.; Meyer, E. Extended Halogen Bonding between Fully Fluorinated Aromatic Molecules. *ACS Nano* **2015**, *9*, 2574−2583.
(33) Pavliček, N.; Herranz-Lancho, C.; Fleury, B.; Neu, M.; Niedenführ, J.; Ruben, M.; Repp, J. High-Resolution Scanning Tunneling and Atomic Force Microscopy of Stereochemically Resolved Dibenzo[a,h]thianthrene Molecules. *Phys. Status Solidi B* **2013**, *250*, 2424−2430.

DOI: 10.1021/acs.jpcc.8b09631
J. Phys. Chem. C 2019, 123, 8379−8386

(34) Monig, H.; Amirjalayer, S.; Timmer, A.; Hu, Z.; Liu, L.; Díaz Arado, O.; Cnudde, M.; Strassert, C. A.; Ji, W.; Rohlfing, M.; et al. Quantitative Assessment of Intermolecular Interactions by Atomic Force Microscopy Imaging Using Copper Oxide Tips. *Nat. Nanotechnol.* **2018**, *13*, 371−375.
(35) Clark, T.; Heßelmann, A. The Coulombic σ-Hole Model Describes Bonding in $CX_3I\cdots Y^-$ Complexes Completely. *Phys. Chem. Chem. Phys.* **2018**, *20*, 22849−22855.
(36) Robinson, S. W.; Mustoe, C. L.; White, N. G.; Brown, A.; Thompson, A. L.; Kennepohl, P.; Beer, P. D. Evidence for Halogen Bond Covalency in Acyclic and Interlocked Halogen-Bonding Receptor Anion Recognition. *J. Am. Chem. Soc.* **2015**, *137*, 499−507.
(37) Huber, S. M.; Jimenez-Izal, E.; Ugalde, J. M.; Infante, I. Unexpected Trends in Halogen-Bond Based Noncovalent Adducts. *Chem. Commun.* **2012**, *48*, 7708−7710.
(38) Thirman, J.; Engelage, E.; Huber, S. M.; Head-Gordon, M. Characterizing the Interplay of Pauli Repulsion, Electrostatics, Dispersion and Charge Transfer in Halogen Bonding With Energy Decomposition Analysis. *Phys. Chem. Chem. Phys.* **2018**, *20*, 905−915.
(39) Dannenberg, J. J.; Haskamp, L.; Masunov, A. Are Hydrogen Bonds Covalent or Electrostatic? A Molecular Orbital Comparison of Molecules in Electric Fields and H-Bonding Environments. *J. Phys. Chem. A* **1999**, *103*, 7083−7086.
(40) Shahi, A.; Arunan, E. Hydrogen Bonding, Halogen Bonding and Lithium Bonding: An Atoms in Molecules and Natural Bond Orbital Perspective Towards Conservation of Total Bond Order, Inter- and Intra-molecular Bonding. *Phys. Chem. Chem. Phys.* **2014**, *16*, 22935−22952.
(41) Stone, A. J. Natural Bond Orbitals and the Nature of the Hydrogen Bond. *J. Phys. Chem. A* **2017**, *121*, 1531−1534.
(42) Grabowski, S. J. What Is the Covalency of Hydrogen Bonding? *Chem. Rev.* **2011**, *111*, 2597−2625.
(43) Elgabarty, H.; Khaliullin, R. Z.; Kühne, T. D. Covalency of Hydrogen Bonds in Liquid Water can be Probed by Proton Nuclear Magnetic Resonance Experiments. *Nat. Commun.* **2015**, *6*, 8318.
(44) Blum, V.; Gehrke, R.; Hanke, F.; Havu, P.; Havu, V.; Ren, X.; Reuter, K.; Scheffler, M. Ab Initio Molecular Simulations With Numeric Atom-Centered Orbitals. *Comput. Phys. Commun.* **2009**, *180*, 2175−2196.
(45) Ren, X.; Rinke, P.; Blum, V.; Wieferink, J.; Tkatchenko, A.; Sanfilippo, A.; Reuter, K.; Scheffler, M. Resolution-of-Identity Approach to Hartree-Fock, Hybrid Density Functionals, RPA, MP2 and GW with Numeric Atom-Centered Orbital Basis Functions. *New J. Phys.* **2012**, *14*, No. 053020.
(46) Tkatchenko, A.; Scheffler, M. Accurate Molecular Van Der Waals Interactions from Ground-State Electron Density and Free-Atom Reference Data. *Phys. Rev. Lett.* **2009**, *102*, No. 073005.
(47) Misquitta, A. J.; Podeszwa, R.; Jeziorski, B.; Szalewicz, K. Intermolecular Potentials Based on Symmetry-Adapted Perturbation Theory with Dispersion Energies from Time-Dependent Density-Functional Calculations. *J. Chem. Phys.* **2005**, *123*, 214103.
(48) Pitoňák, M.; Neogrády, P.; Černý, J.; Grimme, S.; Hobza, P. Scaled MP3 Non-Covalent Interaction Energies Agree Closely with Accurate CCSD(T) Benchmark Data. *ChemPhysChem* **2009**, *10*, 282−289.
(49) Halkier, A.; Helgaker, T.; Jørgensen, P.; Klopper, W.; Koch, H.; Olsen, J.; Wilson, A. K. Basis-Set Convergence in Correlated Calculations on Ne, N_2, and H_2O. *Chem. Phys. Lett.* **1998**, *286*, 243−252.
(50) Ahlrichs, R.; Bär, M.; Häser, M.; Horn, H.; Kölmel, C. Electronic Structure Calculations on Workstation Computers: The Program System Turbomole. *Chem. Phys. Lett.* **1989**, *162*, 165−169.
(51) Řezáč, J. Cuby: An Integrative Framework for Computational Chemistry. *J. Comput. Chem.* **2016**, *37*, 1230−1237.
(52) Corso, M.; Ondráček, M.; Lotze, C.; Hapala, P.; Franke, K.; Jelínek, P.; Pascual, J. I. Charge Redistribution and Transport in Molecular Contacts. *Phys. Rev. Lett.* **2015**, *115*, 136101.
(53) Arunan, E.; Desiraju, G.; Klein, R.; Sadlej, J.; Scheiner, S.; Alkorta, I.; Clary, D. C.; Crabtree, R.; Dannenberg, J.; Hobza, P.; et al. Defining the Hydrogen Bond: An Account (IUPAC Technical Report). *Pure Appl. Chem.* **2011**, *83*, 1637−1641.

DOI: 10.1021/acs.jpcc.8b09631
J. Phys. Chem. C 2019, 123, 8379−8386

SPECTROSCOPY

Real-space imaging of anisotropic charge of σ-hole by means of Kelvin probe force microscopy

B. Mallada[1,2,3]†, A. Gallardo[2,4]†, M. Lamanec[3,5]†, B. de la Torre[1,2], V. Špirko[5,6], P. Hobza[5,7]*, P. Jelinek[1,2]*

An anisotropic charge distribution on individual atoms, such as σ-holes, may strongly affect the material and structural properties of systems. However, the spatial resolution of such anisotropic charge distributions on an atom represents a long-standing experimental challenge. In particular, the existence of the σ-hole on halogen atoms has been demonstrated only indirectly through the determination of the crystal structures of organic molecules containing halogens or with theoretical calculations, consequently calling for its direct experimental visualization. We show that Kelvin probe force microscopy with a properly functionalized probe can image the anisotropic charge of the σ-hole and the quadrupolar charge of a carbon monoxide molecule. This opens a new way to characterize biological and chemical systems in which anisotropic atomic charges play a decisive role.

The observation of molecular structures with the unusual atomic arrangement of possessing two adjacent halogens or a pair of halogen atoms and electron donor motifs (oxygen, nitrogen, sulfur, ...), found in different crystals in the second half of the 20th century (*1*–*4*), represented a long-standing puzzle in supramolecular chemistry. Both halogens and electron donors are electronegative elements that carry a negative charge. Thus, close contacts of these atoms should theoretically cause highly repulsive electrostatic interaction. Counterintuitively, such atoms are frequently found to form intermolecular bonds, called latter halogen bonds, that stabilize the molecular crystal structure. An elegant solution offered by Auffinger *et al.* (*5*), Clark *et al.* (*6*), and Politzer *et al.* (*7*, *8*) showed that the formation of a covalent bond between certain halogen atoms (chlorine, bromine, and iodine) and a more electronegative atom (such as carbon) gives rise to a so-called σ-hole that has an anisotropic charge distribution on the halogen atom. Thus, a physical observable corresponding electrostatic potential around the halogen atom is not uniform (as considered within all empirical force fields) but exhibits an electropositive distal to covalently bound carbon crown surrounded by an electronegative belt (Fig. 1A).

Consequently, halogen bonding is attributed to attractive electrostatic interaction between a halogen's electropositive σ-hole and an electronegative belt of the other halogen or an electronegative atom with negative charge. The International Union of Pure and Applied Chemistry (IUPAC) definition of a halogen bond (*9*) states that a halogen bond "occurs when there is evidence of a net attractive interaction between an electrophilic region associated with a halogen atom in a molecular entity and a nucleophilic region in another, or the same, molecular entity." Stability of the σ-hole bonding is comparable with that of hydrogen-bonded complexes, and attraction in both types of noncovalent complexes was originally assigned to electrostatic interaction. Although this scenario is basically true for H-bonded complexes, in the case of halogen-bonded systems, the importance of dispersion interaction (*10*) was highlighted. The importance of the dispersion interaction is not surprising because close contact takes place between two heavy atoms with high polarizability in halogen-bonded complexes.

The concept of halogen bonding was later generalized to a σ-hole bonding concept. In particular, the halogen (group 17), chalcogen (group 16), pnicogen (group 15), tetrel (group 14), and aerogen bonding (group 18) were established according to the name of the electronegative atom bearing the positive σ-hole. The existence of a σ-hole in atoms of the mentioned groups of elements has a common origin in the unequal occupation of valence orbitals.

The σ-hole bonding plays a key role in supramolecular chemistry (*11*), including the engineering of molecular crystals or in biological macromolecular systems (*5*). Despite its relevance and intensive research devoted to σ-hole bonding, the existence of the σ-hole itself was confirmed only indirectly with quantum calculations (*5*–*8*) or crystal structures of complexes containing σ-hole donors and electron acceptors (*11*–*15*). However, a direct visualization of this entity allowing for the resolution of its peculiar shape has thus far been missing.

The cause of the σ-hole is the anisotropic distribution of the atomic charge on a halogen atom. The imaging of anisotropic atomic charge represents an unfulfilled challenge for experimental techniques, including scanning probe microscopy (SPM), electron microscopy, and diffraction methods. Thus, we sought a technique in which the imaging mechanism relies on the electrostatic force to facilitate the visualization of the anisotropic charge distribution on a halogen atom with a sub-ångstrom spatial resolution. We show that real-space visualization of the σ-hole can be achieved through Kelvin probe force microscopy (KPFM) under ultrahigh vacuum (UHV) conditions (*16*, *17*) with unprecedented spatial resolution.

KPFM belongs to a family of SPM techniques that routinely provide real-space atomic resolution of surfaces. In the KPFM technique, the variation of the frequency shift Δf of an oscillating probe on applied bias voltage V with the quadratic form $\Delta f \sim V^2$ is recorded (*18*). The vertex of the Kelvin parabola $\Delta f(V)$ determines the difference between work functions of tip and sample, also called the contact potential difference V_{CPD}. Moreover, the spatial variation of the contact potential difference V_{CPD} across the surface allows the mapping of local variation of surface dipole on the sample (V_{LCPD}) (*17*). Recent developments of the KPFM technique operating in UHV conditions made it possible to reach true atomic resolution on surfaces (*19*, *20*) to image intramolecular charge distribution (*21*), to control single-electron charge states (*22*), to resolve bond polarity (*23*), or to discriminate charge (*24*).

The atomic contrast in KPFM images originates from a microscopic electrostatic force between static (ρ_0) and polarized charge densities ($\delta\rho$) located on frontier atoms from the tip apex and sample when an external bias is applied (*17*). There are two dominant components of this force: the interaction between the polarized charge on the apex $\delta\rho_t$, which is linearly proportional to the applied bias voltage (V), and the static charge on sample ρ_s^0. The second term consists of the electrostatic interaction between the polarized charge on the sample $\delta\rho_s$ and the static charge on tip ρ_t^0. Consequently, these two components cause local variation of the contact potential difference V_{LCPD} (a detailed description of the mechanism is provided in the supplementary materials), thus providing atomic-scale contrast.

Results

Consequently, KPFM appears to be the tool of choice for imaging anisotropic charge distribution within a single atom, such as the

[1]Regional Centre of Advanced Technologies and Materials, Czech Advanced Technology and Research Institute (CATRIN), Palacký University Olomouc, 78371 Olomouc, Czech Republic. [2]Institute of Physics, Academy of Sciences of the Czech Republic, Prague, Czech Republic. [3]Department of Physical Chemistry, Palacký University Olomouc, tr. 17. listopadu 12, 771 46 Olomouc, Czech Republic. [4]Department of Condensed Matter Physics, Faculty of Mathematics and Physics, Charles University, V Holešovičkách 2, 180 00 Prague, Czech Republic. [5]Institute of Organic Chemistry and Biochemistry, Czech Academy of Sciences, Flemingovo Náměstí 542/2, 16000 Prague, Czech Republic. [6]Department of Chemical Physics and Optics, Faculty of Mathematics and Physics, Charles University in Prague, Ke Karlovu 3, 12116 Prague, Czech Republic. [7]IT4Innovations, VŠB-Technical University of Ostrava, 17. listopadu 2172/15, 70800 Ostrava-Poruba, Czech Republic.
*Corresponding author. Email: pavel.hobza@uochb.cas.cz (P.H.); jelinekp@fzu.cz (P.J.)
†These authors contributed equally to this work.

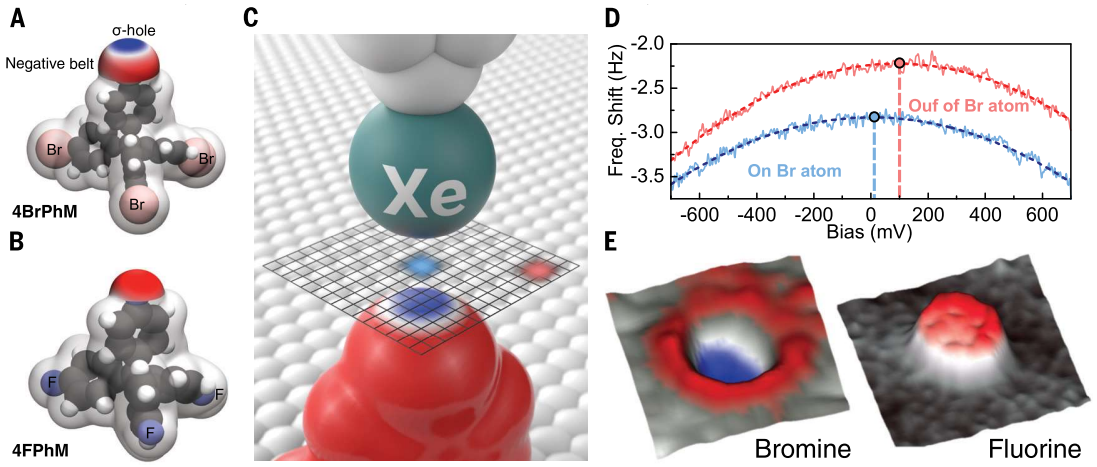

Fig. 1. Schematic view of the KPFM measurements to image a σ-hole. (**A** and **B**) Models of 4BrPhM and 4FPhM molecules, including corresponding electrostatic potential map on outermost Br/F atom. They reveal the presence of the σ-hole on a Br atom, and there is an isotropic negative charge on the F atom. (**C**) Schematic view of the acquisition method of the KPFM measurement with a functionalized Xe-tip on a 2D grid. (**D**) Corresponding $\Delta f(V)$ parabolas acquired in the central part (blue) of the 2D grid and on the periphery (red). Vertical dashed lines indicate the value of V_{LCPD} for the given $\Delta f(V)$ parabola, which forms the 2D KPFM image. (**E**) 3D representation of the KPFM images (V_{LCPD} maps) acquired with an Xe-tip over bromide and fluoride atoms of 4BrPhM and 4FPhM molecules. Blue indicates low values of V_{LCPD}, and red indicates high values of V_{LCPD}.

σ-hole. To test this hypothesis, we deliberately chose tetrakis(4-bromophenyl) methane (4BrPhM) and tetrakis(4-fluorophenyl) methane (4FPhM) compounds (Fig. 1, A and B).The skeleton arrangement of these compounds facilitates a tripodal configuration once deposited onto a surface with a single bromine-fluor atom oriented outward from the surface (fig. S1). This arrangement facilitated direct inspection of the σ-hole on a halogen atom by the front-most atom of a scanning probe, (Fig. 1C). Deposition of the molecules in low coverage (less than 1 monolayer) on the Ag(111) surface held at room temperature under UHV conditions led to the formation of well-ordered, self-assembled molecular arrangements in a rectangular formation (Fig. 2, A and B). Bromine atoms of the 4BrPhM molecule have a substantial positive σ-hole (Fig. 1A), and fluorine atoms possess an isotropic negative charge (Fig. 1B). This enabled us to perform comparative measurements on similar systems with and without the presence of the σ-hole.

Shown in Fig. 2, C and D, is a substantial contrast between two-dimensional (2D) constant-height KPFM maps acquired over Br and F front-most atoms of the molecular compounds with an Xe-decorated tip. In the case of the 4FPhM molecule, we observed a monotonous elliptical increase of the V_{LCPD} signal over the fluorine atom. In comparison, the KPFM image over the 4BrPhM molecule featured a notable ring-like shape. The 2D KPFM maps were recorded in the attractive tip-sample interaction regime near the minimum of the Δf-z curve (fig. S2) to avoid undesired topographic cross-talk (fig. S3 and supplementary text) or the effect of lateral bending of the functionalized probe due to repulsive forces (*25*) that could cause image distortions. Evolution of the contrast of the KPFM image of the σ-hole

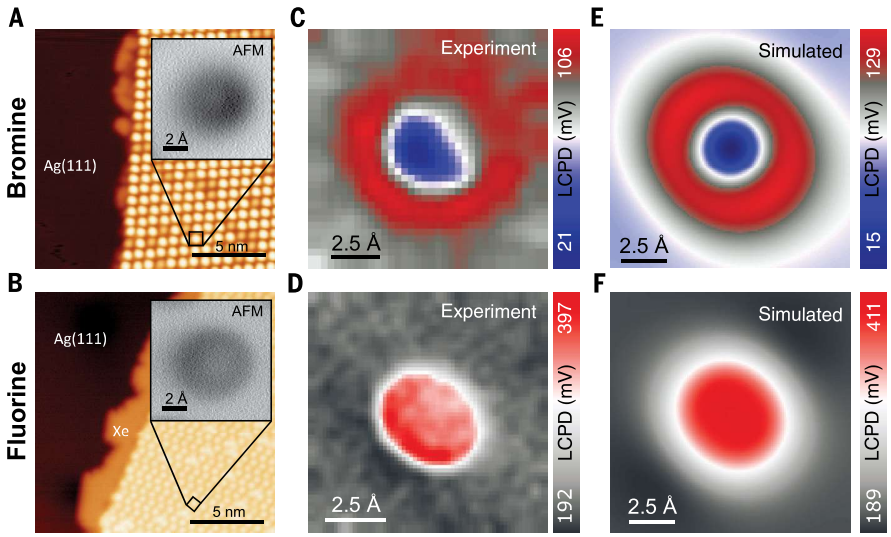

Fig. 2. KPFM imaging of 4BrPhM and 4FPhM molecules with an Xe-tip. (**A** and **B**) STM images of a molecular self-assembled submonolayer of 4BrPhM and 4FPhM molecules on an Ag(111) surface. (Insets) AFM images acquired on a single molecule with a Xe tip at the minima of the frequency shift. (**C** and **D**) Experimental KPFM images obtained with a functionalized Xe tip over bromide and fluoride atoms of single 4BrPhM and 4FPhM molecules. (**E** and **F**) Calculated KPFM images with a functionalized Xe tip of single 4BrPhM and 4FPhM molecules. Blue indicates low values of V_{LCPD} and red indicates high values of V_{LCPD}).

on the front-most Br atom with the tip-sample distance is shown in fig. S4.

Discussion

To confirm the origin of the anisotropic contrast observed experimentally on the Br atom, we carried out KPFM simulations using static ρ_0 and polarized $\delta\rho$ charges of Br and F-terminated molecules and Xe-tip models obtained from density functional theory (DFT) calculations (fig. S5). Simulated KPFM images that are perfectly matched to the experimental maps are shown in Fig. 2, E and F. Our theoretical model allowed us to decompose the two leading contributions: the electrostatic interaction of the polarized charge on tip $\delta\rho_t$ with the static charge on the molecule and the counterpart term of the electrostatic interaction between the polarized charge on molecule $\delta\rho_s$ with the ρ_t^0 static charge of the tip (fig. S5). We found that the anisotropic contrast obtained on the Br-terminated molecule can be rationalized from a variation of the microscopic electrostatic interaction between

atomic-scale charges of tip and sample. On the periphery of the Br atom, the positive shift of V_{CPD} is given by the electrostatic interaction of the spherical polarized charge, $\delta\rho_t$ of the Xe-tip apex, with the belt of negative charge surrounding the positive σ-hole. By contrast, in the central part, the electrostatic interaction with the positive crown of the σ-hole turned the V_{LCPD} value with respect to that on the peripheral region. In the case of the 4FPhM molecule, both terms provided a trivial contrast with a positive shift of the V_{LCPD} over the atom. The term corresponding to the static charge ρ_s^0 on the molecule revealed an elliptical shape originating from neighbor positively charged hydrogen atoms in the underlying phenyl group of the 4FPhM molecule. Therefore, the shape of the feature presented in the KPFM image provided additional information about the internal arrangement of the molecule on the surface.

We deliberately used a single Xe atom to functionalize the tip apex instead of the more commonly used carbon monoxide (CO). As discussed above, the Xe tip allowed us to optimize the imaging conditions of the σ-hole because static charge density ρ_0 on the apex of the CO-tip had a strong quadrupolar character (Fig. 3A), and the charge on the Xe tip was highly spherical (fig. S5). This choice eliminated spurious spatial variation of the V_{LCPD} signal, which did not belong directly to the σ-hole. In particular, a component of the microscopic electrostatic interaction between static charge ρ_t^0 of the tip and polarized charge on sample $\delta\rho_s$ needs to be abolished. In the case of the Xe-tip, the spatial variation of the local V_{CPD} was dominated by the component that includes the interaction of a spherically polarized charge on the Xe atom $\delta\rho_t$ with the anisotropic electrostatic field of the σ-hole. This enabled a direct mapping of the spatial charge distribution of the σ-hole by means of the KPFM technique.

Thus, it is instructive to look at the KPFM images acquired with the CO tip on the 4FPhM molecule as well. Despite the frontier fluorine atom of the 4FPhM molecule having an isotropic charge distribution, the experimental KPFM image (Fig. 3B) features a nontrivial ringlike shape with lower values of the V_{LCPD} signal on the center of the fluorine atom. Our KPFM simulation using a CO-tip (Fig. 3C) coincided qualitatively with the experimental counterpart. From a detailed analysis of the electrostatic components (fig. S6), we found that the contrast arose from the interaction of the spherical polarized charge $\delta\rho_s$ on a fluorine atom with the static quadrupole charge on a CO tip, composed of a negative crown of density on an oxygen atom surrounded by a positive charge belt (Fig. 3A). Thus, the KPFM features resolved on the 4FPhM molecule reflected the quadrupolar charge distribution of the CO tip. Thus, from the spatial variation of the V_{LCPD} signal, we could determine the sign of the quadrupole of the CO molecule on the tip. The shift of V_{LCPD} toward lower values in the central part of the KPFM image was caused by the negative charge crown of the quadrupole charge localized at oxygen (Fig. 3A). The enhanced V_{LCPD} value on the periphery reflects the positively charged belt of the quadrupole charge of the CO molecule. This reverse shift of V_{LCPD} with respect to the previous case of the σ-hole was caused by our inspection of the anisotropic charge on the tip instead of the sample. A detailed explanation of the origin and sign of V_{LCPD} shift is available in the supplementary materials.

Alternatively, some works reported subatomic features in noncontact atomic force microscopy (nc-AFM) (*26*) images with CO functionalized tips (*27*). However, the origin of such contrast and their interpretation of the physical meaning are under debate (*28*, *29*). Additionally, nc-AFM has demonstrated unprecedented chemical resolution of single molecules (*30*) or their charge distribution (*31*). Thus, we were intrigued by the possibility of imaging the σ-hole by means of nc-AFM with functionalized tips (*27*).

A series of high-resolution nc-AFM images acquired at a wide range of tip-sample distances are shown in fig. S7 with a CO tip and Xe tip, respectively. At the onset of the atomic contrast in nc-AFM mode, the tip-sample interaction was dominated by an attractive dispersion. The resulting AFM contrast for both 4FPhM and 4BrPhM molecules had a similar spherical character that lacks any subatomic feature. Also, in close tip-sample distances, the AFM contrast remained similar for both molecular compounds, featuring a bright spot in the center caused by the Pauli repulsion. Thus, we found that the AFM images did not reveal any signature of the σ-hole in the whole range of tip-sample distances covering both an attractive and repulsive interaction regime.

To understand in detail this experimental observation, we performed theoretical analysis of the nc-AFM images with a CO tip using the probe particle SPM model (*25*). Shown in figs. S8 and S9 are lateral cross sections of different force components of the interaction energy acting between the CO tip and the outermost F and Br atoms of the 4FPhM and 4BrPhM molecules, respectively. The calculated AFM images showed similar atomic contrast, ruling out the possibility to image the σ-hole with a CO tip. From the analysis, we inferred that the AFM contrast was dominated by dispersive and Pauli interaction, both of which have a highly spherical character. On the other hand, the electrostatic interaction possesses an anisotropic character caused by the presence of both a σ-hole on the Br atom and a quadrupolar charge distribution on the apex of the CO-tip (Fig. 3A). Nevertheless, the magnitude of the electrostatic interaction was about one order smaller than the competing dispersion and Pauli interactions, which made the σ-hole hard to image in the AFM technique. From this analysis, we could conclude that the resolution of anisotropic atomic charges requires a technique such as KPFM, whose contrast mechanism is mastered by the electrostatic interaction that maps the charge distribution on the forefront atoms.

Next, we investigated the influence of the σ-hole on the noncovalent intermolecular interaction energies. The nc-AFM technique provided the distinctive possibility to explore interaction energies between individual atoms and molecules placed on the tip apex and sample by means of site-specific force spectroscopies (*32*–*35*). Apart from a quantitative evaluation of the interaction energies between well-defined entities, the nc-AFM

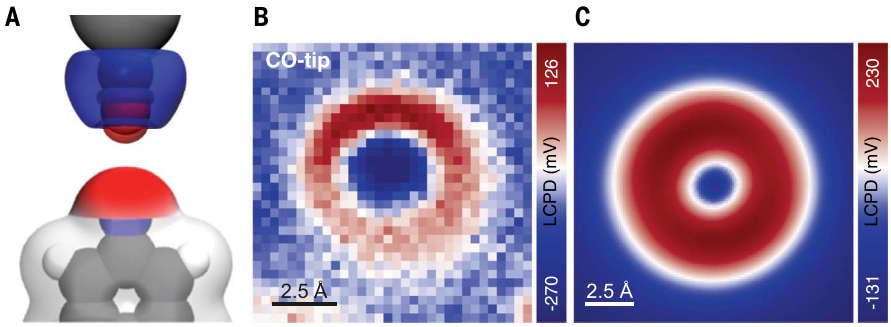

Fig. 3. KPFM imaging of a 4FPhM molecule with a CO tip. (**A**) Schematic view of a CO tip above a 4FPhM molecule with a superimposed calculated differential charge density of the CO tip, revealing (top) a quadrupole charge of a CO-tip model and (bottom) calculated electrostatic potential of 4FPhM molecule showing an isotropic negative charge on the frontier fluorine atom in 4FPhM. (**B**) Experimental KPFM image acquired over the frontier fluorine atom with a CO tip. (**C**) Simulated KPFM image of a 4FPhM molecule with a CO tip. Blue indicates low values of V_{LCPD}, and red indicates high values of V_{LCPD}).

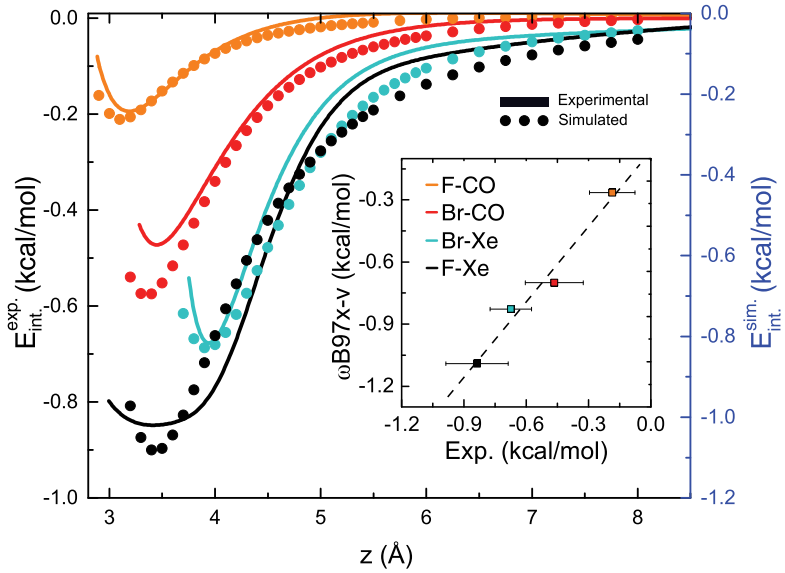

Fig. 4. Comparison of experimental and theoretical interaction energies of four complexes. Experimental (solid curves) and calculated (dots, obtained with DFT/ωB97X-V) energy curves versus tip-sample distance between 4FPhM and 4BrPhM molecules and Xe and CO tips. (Inset) The correlation between experimental and theoretical values [coefficient of determination (R^2) = 0.98] of the energy minima for all complexes. Bars indicate an estimated experimental error of the energy minima calculated as the difference between a polynomial fit and the experimental energy (fig. S12).

technique also gave an invaluable opportunity to benchmark the accuracy of different theoretical methods to describe these weak noncovalent interactions (*34*–*36*).

Tip functionalization offered an opportunity to explore distinct scenarios of the interaction mechanisms with molecular complexes. The Xe tip has a positive net charge and large polarizability, but the CO tip possesses a quadrupolar charge (O and C carry negative and positive net charge, respectively) and a relatively small polarizability. Their interaction energies are shown in Fig. 4, with the 4FPhM and 4BrPhM molecules as a function of the tip-sample distance. Small values of the maximum energies of 0.2 to 0.83 kcal/mol revealed a noncovalent bonding mechanism. In general, the complexes with an Xe-tip are more stable than the complexes with a CO tip, which may be rationalized by a larger dispersion interaction caused by an Xe tip. We observed that the Xe-4BrPhM complex was less stable than the Xe-4FPhM complex (by 0.67 and 0.83 kcal/mol, respectively) despite the larger polarizability of Br that determines the magnitude of the polarization interaction. This effect was caused by the presence of the repulsive electrostatic interaction between the positive σ-hole on a Br atom and the positively charged Xe tip, which partially cancelled the attractive dispersive interaction in the Xe-4BrPhM complex. On the other hand, the dispersive and electrostatic forces are both attractive in the case of the Xe-4FPhM complex, resulting in a larger total interaction energy. This observation not only supported the presence of the positive σ-hole on the Br atom, it also explained the origin of a peculiar intermolecular orientation of halogen-bonded molecular systems (*12*–*15*).

Recently, a vigorous effort has been devoted to the development of computational methods based on DFT with dispersion correction that are able to reliably describe intermolecular interactions in noncovalent complexes (*37*). But their transferability is still limited owing to adopted approximations, and thus, careful benchmarking is desired. From this perspective, the above-described complexes represent interesting noncovalent systems for benchmarks with a complex interplay between the dispersion and the electrostatic interaction. The maximum interaction energies measured were below 1 kcal/mol, which used to be considered as the limit of chemical accuracy, further strengthening the benchmark.

Accurate interaction energies for different types of noncovalent complexes could be obtained from a nonempirical coupled-cluster method covering triple-excitations [CCSD(T)]. Unfortunately, its large computational demands made it impossible to apply this method to a system of the size of the molecules we investigated in the present work.

To circumvent this problem, we performed the CCSD(T) calculations on smaller reference model systems consisting of F- and Br-benzene, exhibiting similar characteristics as 4BrPhM and 4FPhM molecules (supplementary materials). We compared the calculated CCSD(T) interaction energies to interaction energies obtained with several popular DFT functionals (table S3). We found that the range-separated ωB97X-V functional (*38*) that implicitly covers dispersion energy provided good agreement with the benchmarked dataset (table S3). Because this functional was also shown to provide the best results among other popular DFT functionals for various types of systems with noncovalent interactions (*38*), we selected this functional for further use.

To check its transferability to our larger molecular systems, we calculated the interaction energies between 4FPhM and 4BrPhM molecules and Xe- and CO-tip models. Excellent agreement between the ωB97X-V interaction energies and the experimental data results is shown in Fig. 4. The calculated energy minima for all complexes fit the measured values perfectly within the experimental error (Fig. 4, inset). The PBE0 functional (*39*) with the D3 correction (*40*) reproduced the CCSD(T) results on small-model systems as well (table S3 and fig. S10). However, its transferability on the large systems was no longer as good as the range-separated ωB97X-V functional (fig. S11).

The ωB97X-V functional describes well the interaction trend for all considered systems (Fig. 4, inset), with the caveat that it systematically slightly overestimates the interaction energy by ~0.1 kcal/mol. The perfect agreement between theoretical and experimental values could not be expected because calculations were limited to free-standing 4FPhM and 4BrPhM molecules interacting with Xe- and CO-tip model, and in the experiment, 4FPhM and 4BrPhM molecules were adsorbed at Ag(111) surface. The results confirmed good transferability of the ωB97X-V functional toward larger systems. Moreover, the good agreement between calculated and experimental datasets obtained for all four complexes also gave confidence in the multiscale benchmark technique that uses small-model complexes with the Xe-tip model. Therefore, this approach makes it possible to accurately describe systems whose size does not allow for the direct application of the accurate coupled-cluster technique (or a similar technique), or when other direct experimental measurements are currently not feasible.

Conclusions

We report the possibility of achieving the spatial resolution of anisotropic atomic charge with the KPFM technique, which not only provided direct evidence of the existence of σ-holes but is expected to substantially extend the possibility to characterize charge distribution in complex molecular systems and on surfaces. We anticipate that this technique could

be further extended to provide invaluable information about the local inhomogeneous polarizability of individual atoms on surfaces or within molecules with unprecedented spatial resolution in chemical and biologically relevant systems.

REFERENCES AND NOTES

1. N. Ramasubbu, R. Parthasarathy, P. Murray-Rust, *J. Am. Chem. Soc.* **108**, 4308–4314 (1986).
2. O. Hassel, J. Hvoslef, E. H. Vihovde, N. A. Sörensen, *Acta Chem. Scand.* **8**, 873–873 (1954).
3. O. Hassel *et al.*, *Acta Chem. Scand.* **13**, 275–280 (1959).
4. O. Hassel *et al.*, *Acta Chem. Scand.* **12**, 1146–1146 (1958).
5. P. Auffinger, F. A. Hays, E. Westhof, P. S. Ho, *Proc. Natl. Acad. Sci. U.S.A.* **101**, 16789–16794 (2004).
6. T. Clark, M. Hennemann, J. S. Murray, P. Politzer, *J. Mol. Model.* **13**, 291–296 (2007).
7. T. Brinck, J. S. Murray, P. Politzer, *Int. J. Quantum Chem.* **44** (S19), 57–64 (1992).
8. P. Politzer, P. Lane, M. C. Concha, Y. Ma, J. S. Murray, *J. Mol. Model.* **13**, 305–311 (2007).
9. G. R. Desiraju *et al.*, *Pure Appl. Chem.* **85**, 1711–1713 (2013).
10. K. E. Riley, P. Hobza, *Phys. Chem. Chem. Phys.* **15**, 17742–17751 (2013).
11. L. C. Gilday *et al.*, *Chem. Rev.* **115**, 7118–7195 (2015).
12. Z. Han *et al.*, *Science* **358**, 206–210 (2017).
13. J. Tschakert *et al.*, *Nat. Commun.* **11**, 5630 (2020).
14. S. Kawai *et al.*, *ACS Nano* **9**, 2574–2583 (2015).
15. H. Huang *et al.*, *ACS Nano* **10**, 3198–3205 (2016).
16. M. Nonnenmacher, M. P. O'Boyle, H. K. Wickramasinghe, *Appl. Phys. Lett.* **58**, 2921–2923 (1991).
17. T. Glatzel, S. Sadewasser, Eds., *Kelvin Probe Force Microscopy* (Springer, 2018), vol. 65.
18. W. Melitz, J. Shen, A. C. Kummel, S. Lee, *Surf. Sci. Rep.* **66**, 1–27 (2011).
19. L. Nony, A. S. Foster, F. Bocquet, C. Loppacher, *Phys. Rev. Lett.* **103**, 036802 (2009).
20. S. Sadewasser *et al.*, *Phys. Rev. Lett.* **103**, 266103 (2009).
21. F. Mohn, L. Gross, N. Moll, G. Meyer, *Nat. Nanotechnol.* **7**, 227–231 (2012).
22. L. Gross *et al.*, *Science* **324**, 1428–1431 (2009).
23. F. Albrecht *et al.*, *Phys. Rev. Lett.* **115**, 076101 (2015).
24. B. Mallada *et al.*, *ACS Sustain. Chem. Eng.* **8**, 3437–3444 (2020).
25. P. Hapala *et al.*, *Phys. Rev. B Condens. Matter Mater. Phys.* **90**, 085421 (2014).
26. T. R. Albrecht, P. Grütter, D. Horne, D. Rugar, *J. Appl. Phys.* **69**, 668–673 (1991).
27. P. Jelínek, *J. Phys. Condens. Matter* **29**, 343002 (2017).
28. F. Huber *et al.*, *Science* **366**, 235–238 (2019).
29. M. Emmrich *et al.*, *Science* **348**, 308–311 (2015).
30. L. Gross, F. Mohn, N. Moll, P. Liljeroth, G. Meyer, *Science* **325**, 1110–1114 (2009).
31. P. Hapala *et al.*, *Nat. Commun.* **7**, 11560 (2016).
32. M. A. Lantz *et al.*, *Science* **291**, 2580–2583 (2001).
33. Y. Sugimoto *et al.*, *Nature* **446**, 64–67 (2007).
34. S. Kawai *et al.*, *Nat. Commun.* **7**, 11559 (2016).
35. Z. Sun, M. P. Boneschanscher, I. Swart, D. Vanmaekelbergh, P. Liljeroth, *Phys. Rev. Lett.* **106**, 046104 (2011).
36. C. Wagner *et al.*, *Nat. Commun.* **5**, 5568 (2014).
37. S. Grimme, A. Hansen, J. G. Brandenburg, C. Bannwarth, *Chem. Rev.* **116**, 5105–5154 (2016).
38. N. Mardirossian, M. Head-Gordon, *Phys. Chem. Chem. Phys.* **16**, 9904–9924 (2014).
39. C. Adamo, V. Barone, *J. Chem. Phys.* **110**, 6158–6170 (1999).
40. S. Grimme, J. Antony, S. Ehrlich, H. Krieg, *J. Chem. Phys.* **132**, 154104 (2010).
41. B. Mallada *et al.*, Data for "Real-space imaging of anisotropic charge of σ-hole by means of Kelvin probe force microscopy". *Zenodo* (2020); doi:10.5281/zenodo.5172233.

ACKNOWLEDGMENTS

We acknowledge fruitful discussions with A. Růžička and P. Hapala. M.L. acknowledges inspirational advice from his previous supervisor, J. Kuchár. P.J. and B.d.l.T. dedicate this manuscript to the memory of J. M. Gómez-Rodríguez. **Funding:** This work was supported by the Czech Science Foundation GACR 20-13692X (A.G., B.M., and P.J.) and 19-27454X (P.H.); Praemium Academie of the Academy of Science of the Czech Republic (A.G.); Palacký University Internal Grant Association IGA_PrF_2021_031 (M.L.); Palacký University Internal Grant Association IGA_PrF_2021_034 (B.M.); and CzechNanoLab Research Infrastructure, supported by MEYS CR (LM2018110). **Author contributions:** Conceptualization: P.J. Methodology: B.M., A.G., B.d.l.T., and P.J. Theoretical calculations: A.G., M.L., V.Š., P.J., and P.H. Experimental: B.M. and B.d.l.T. Funding acquisition: P.H. and P.J. Supervision: B.d.l.T., P.H., and P.J. Writing, original draft: B.M., A.G., B.d.l.T., P.H., and P.J. **Competing interests:** The authors declare that they have no competing interests. **Data and materials availability:** All data needed to evaluate the conclusions in the paper are present in the paper or the supplementary materials. Data can be found at Zenodo (*41*).

SUPPLEMENTARY MATERIALS

science.org/doi/10.1126/science.abk1479
Materials and Methods
Supplementary Text
Figs. S1 to S20
Tables S1 to S3
References (*42*–*55*)

24 June 2021; resubmitted 28 July 2021
Accepted 20 September 2021
10.1126/science.abk1479

On-Surface Synthesis Hot Paper

Deutsche Ausgabe: DOI: 10.1002/ange.201909074
Internationale Ausgabe: DOI: 10.1002/anie.201909074

Strain-Induced Isomerization in One-Dimensional Metal–Organic Chains

Mykola Telychko[+], Jie Su[+], Aurelio Gallardo[+], Yanwei Gu, Jesús I. Mendieta-Moreno, Dongchen Qi, Anton Tadich, Shaotang Song, Pin Lyu, Zhizhan Qiu, Hanyan Fang, Ming Joo Koh, Jishan Wu, Pavel Jelínek* und Jiong Lu**

Abstract: *The ability to use mechanical strain to steer chemical reactions creates completely new opportunities for solution- and solid-phase synthesis of functional molecules and materials. However, this strategy is not readily applied in the bottom-up on-surface synthesis of well-defined nanostructures. We report an internal strain-induced skeletal rearrangement of one-dimensional (1D) metal–organic chains (MOCs) via a concurrent atom shift and bond cleavage on Cu(111) at room temperature. The process involves Cu-catalyzed debromination of organic monomers to generate 1,5-dimethylnaphthalene diradicals that coordinate to Cu adatoms, forming MOCs with both homochiral and heterochiral naphthalene backbone arrangements. Bond-resolved non-contact atomic force microscopy imaging combined with density functional theory calculations showed that the relief of substrate-induced internal strain drives the skeletal rearrangement of MOCs via 1,3-H shifts and shift of Cu adatoms that enable migration of the monomer backbone toward an energetically favorable registry with the Cu(111) substrate. Our findings on this strain-induced structural rearrangement in 1D systems will enrich the toolbox for on-surface synthesis of novel functional materials and quantum nanostructures.*

Introduction

On-surface synthesis of functional nanomaterials has attracted tremendous research interest because of its great potential for creating atomically precise functional nanostructures with tailored electronic and magnetic properties.[1–6] A common on-surface synthetic strategy involves thermal- or phototriggered chemical transformation of rationally designed molecular precursors on an appropriately chosen substrate.[7] The future development in this field will hinge on the exploration of conceptually new toolkits that will enable precise steering of surface reactions under mild conditions to fabricate novel nanostructures with multiple functionalities.

Mechanochemical syntheses driven by the application of an external force or strain have emerged as promising and straightforward alternatives to traditional synthetic methods for fabricating functional organic molecules and nanomaterials. In addition to enabling advantageous solvent-free synthesis, mechanochemistry offers a completely new and efficient method for obtaining valuable products with high yield and selectivity.[8] It would therefore be desirable to use mechanochemistry in bottom-up on-surface synthesis. Unfortunately, this is not straightforward because conventional methods for applying mechanical force, such as ball milling and cavity grinding, cannot be directly used with reactants adsorbed on surfaces.

As an alternative to standard mechanochemical methods, internal strain in molecular systems induced by interactions with a substrate could be used to mimic external mechanical stimuli. Recent studies have shown that substrate-induced structural distortion of molecular systems can facilitate their intra- and intermolecular cyclodehydrogenation as well as

[*] Dr. M. Telychko,[+] J. Su,[+] Y. Gu, S. Song, P. Lyu, Z. Qiu, H. Fang, Prof. M. J. Koh, Prof. J. Wu, Prof. J. Lu
Department of Chemistry, National University of Singapore
3 Science Drive 3, Singapore 117543 (Singapore)
E-Mail: chmwuj@nus.edu.sg
chmluj@nus.edu.sg
Dr. M. Telychko,[+] J. Su,[+] Prof. J. Lu
Centre for Advanced 2D Materials (CA2DM)
National University of Singapore
6 Science Drive 2, Singapore 117546 (Singapore)
A. Gallardo[+]
Faculty of Mathematics and Physics, Charles University
V Holešovičkách 2, 180 00 Prague (Czech Republic)
A. Gallardo,[+] J. I. Mendieta-Moreno, P. Jelínek
Institute of Physics, The Czech Academy of Sciences
162 00 Prague (Czech Republic)
E-Mail: jelinekp@fzu.cz
A. Gallardo,[+] P. Jelínek
Regional Centre of Advanced Technologies and Materials
Palacký University
78371 Olomouc (Czech Republic)
D. Qi
School of Chemistry, Physics and Mechanical Engineering
Queensland University of Technology
Brisbane, Queensland 4001 (Australia)
Dr. A. Tadich
Australian Synchrotron
800 Blackburn Road, Clayton, Victoria 3168 (Australia)
Z. Qiu
NUS Graduate School for Integrative Sciences and Engineering
National University of Singapore
28 Medical Drive, Singapore 117456 (Singapore)
[+] These authors contributed equally to this work.
Supporting information and the ORCID identification number(s) for the author(s) of this article can be found under: https://doi.org/10.1002/anie.201909074.

skeletal rearrangements.[9,10] Treirer et al. showed that van der Waals interactions between a polyphenylene precursor and a Cu(111) substrate tend to increase intramolecular strain, facilitating intramolecular cyclodehydrogenation and nanographene formation at elevated temperatures.[9] Furthermore, Shiotari et al. found that the adsorption of a non-planar polycyclic hydrocarbon on Cu(100) induces the accumulation of internal strain, and that the relief of this strain at elevated temperatures promotes diverse skeletal rearrangements.[10] It has also been reported that the substrate-binding affinity of equivalent chemical groups in organic molecules varies depending on their local adsorption geometries, enabling site-selective bond functionalization.[11]

It is thus well established that strain energy stored in molecular systems on metallic substrates can be exploited to drive their chemical conversion into desired products. However, this phenomenon has primarily been studied in the context of chemical transformations of individual molecules. The use of substrate-induced internal strain to promote on-surface synthesis of extended nanostructures has not yet been studied systematically.

Herein, we demonstrate that strain relief in an extended 1D metal–organic chain (MOC) can drive extensive skeletal transformations at room temperature. The 1,5-dibromo-2,6-dimethylnaphthalene (DBDMN) precursor used in this work undergoes debromination upon deposition on a Cu(111) surface at room temperature, followed by the coordination of the resulting radicals to Cu adatoms to form self-assembled MOCs (Figure 1 a). Submolecular resolution imaging of these MOCs before and after strain relaxation was achieved using qPlus-based non-contact atomic force microscopy (nc-AFM) with a carbon monoxide (CO)-functionalized tip. This showed that the strain-induced skeletal rearrangement of the MOCs involves a concurrent shift of Cu adatoms and H atoms accompanied by the migration of the monomer backbone toward an energetically favorable registry with the Cu(111) substrate. Theoretical calculations revealed the optimal reaction pathways for this process and the importance of entropic effects in the strain-driven skeletal transformations of 1D MOCs.

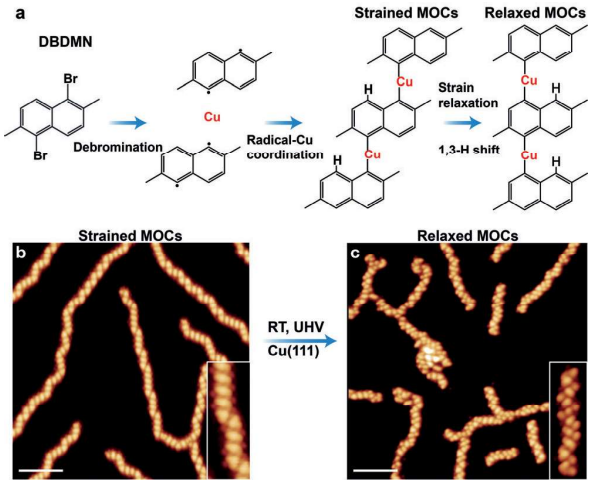

Figure 1. The skeletal rearrangement of MOCs on Cu(111). a) An illustration of the synthesis of MOCs and their structural relaxation on Cu(111). As-deposited DBDMN molecules undergo debromination and self-assemble into 1D MOCs. RT annealing leads to skeletal rearrangement of the MOC lattice. b,c) Large-scale STM topography images of 1D MOCs grown on Cu(111) before (b) and after (c) prolonged annealing under UHV at RT. The inset images show magnified views of representative strained and relaxed MOCs. Both images were acquired using tunneling parameters of 1 V, 1 nA; scale bars = 5 nm.

Results and Discussion

The DBDMN monomer was chosen as a precursor for MOC formation by deposition on a Cu(111) substrate. The synthesis and characterization of the purified DBDMN monomer are presented in the Supporting Information. As shown schematically in Figure 1 a, DBDMN has a naphthalene backbone with methyl groups at the 2 and 6 positions, and bromine atoms at the 1 and 5 positions. Adsorption on the Cu(111) surface was expected to induce facile cleavage of the C–Br bonds, forming σ-radicals (C(Br) radicals) that could coordinate with Cu adatoms to form MOCs. To test this hypothesis, we performed scanning tunneling microscopy (STM) on a Cu(111) surface after the deposition of DBDMN monomers at room temperature; this revealed the formation of 1D chain-like structures on Cu(111) (Figure 1 b). These 1D chains were often decorated by round protrusions, presumably because of the presence of Br adatoms released upon debromination and in keeping with previous results.[12] Photoelectron spectroscopy experiments showed that the debromination of the DBDMN monomers occurred at room temperature and was accompanied by Cu–C bond formation and the emergence of MOCs (Supporting Information, Note 1, Figure S2). Room-temperature cleavage of the C–Br bonds of DBDMN on Cu(111) thus leads to the formation of 1D MOCs. Close-up STM images of representative MOCs showed that they contain only junctions formed by the heterochiral or homochiral coordination of neighboring DBDMN monomers (Figures 2 d,h). Conversely, samples subjected to prolonged (ca. 12 h) room-temperature annealing under ultrahigh vacuum (UHV) conditions formed a new type of 1D chain with distinct dumbbell-shaped junctions (Figure 1 c). This suggests that the initially formed MOCs underwent structural rearrangement during annealing—presumably because of substrate-induced strain. Throughout the manuscript, we refer to the MOCs obtained before and after room-temperature annealing as the „strained“ and „relaxed“ MOC isomers, respectively.

Structural characterization of strained MOCs. We initially probed the structures of the strained MOCs using STM and nc-AFM with a qPlus sensor. The nc-AFM imaging strategy used in this work relies on the functionalization of the tip with a CO molecule and the operation of the microscope in constant height mode in the short-range Pauli repulsion regime.[13] The strongest Pauli repulsion occurs over regions of high electron density (for example, chemical bonds), which allows organic and metal–organic nanostructures to be imaged with submolecular resolution.[14–17] Figure 2 shows

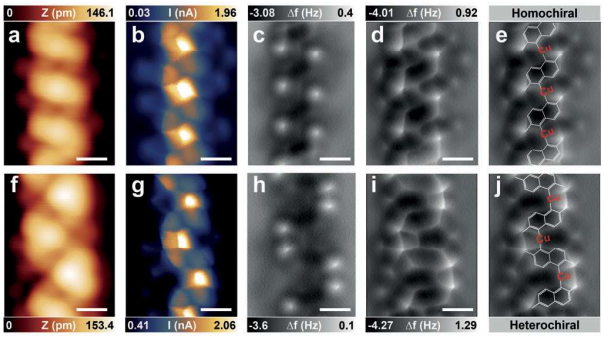

Figure 2. Structural characterization of strained MOCs. STM topography, constant height STM current, and nc-AFM images of a–e) homochiral and f–j) heterochiral MOC segments acquired using a CO tip. Tunneling parameters for STM topography images: 1 V, 1 nA. Constant height images were collected at tip-sample distances of +50 pm (d,i) and +100 pm (c,h) with respect to the set point of 50 mV, 1 nA; scale bars = 500 pm. Panel (e) and (j): the chemical structures of the MOCs superimposed over the nc-AFM images shown in (d) and (i).

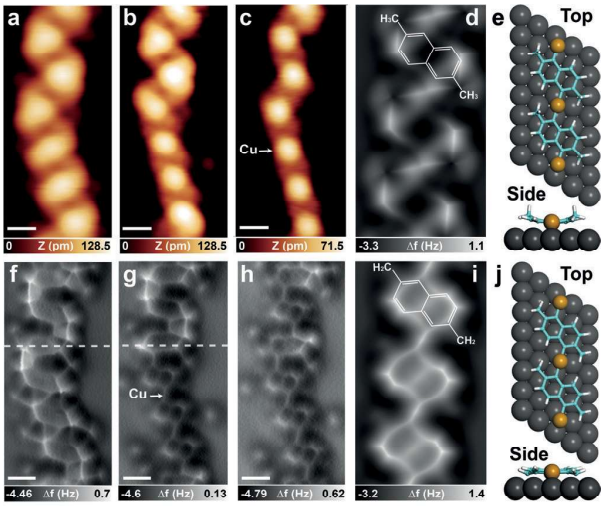

Figure 3. Tip-assisted dehydrogenation of methyl groups. STM topography and the corresponding constant height nc-AFM images of a,f) the strained MOC and the same MOC with b,g) partially and c,h) fully dehydrogenated methyl groups. d,i) Simulated nc-AFM images of a homochiral MOC with and without dehydrogenated methyl groups, respectively. e,j) DFT-optimized models showing the conformations of two adjacent DBDMN backbones before and after tip-assisted dehydrogenation of their methyl groups, respectively. STM topography images were acquired using tunneling parameters of 1 V, 1 nA. Constant height images were collected at tip-sample distances of +50 pm (f), +70 pm (g), and +50 pm (h) with respect to a setpoint of 20 mV, 1 nA.

STM topography, constant height current, and nc-AFM images of the strained homochiral (Figures 2a–e) and heterochiral (Figures 2f,j) MOC junctions. The bond-resolved nc-AFM images show a series of interconnected rectangular features with two bright apexes, which were assigned to the backbone of the individual DBDMN monomers and their methyl groups.

Nc-AFM images acquired with a larger tip–sample distance indicated that the methyl groups exhibited the strongest Pauli repulsion (Figures 2c,h). The faint lines linking adjacent molecules via the carbon atoms originally bound to Br (1 and 5) exhibit the highest STM contrast. Similar enhancements of STM contrast over coordinated adatoms have been reported for multiple metal–organic systems.[18–20] These observations indicate that σ-radicals formed by cleaving the C–Br bonds in DBDMN coordinate to Cu adatoms, forming 1D MOCs. We also resolved the Cu(111) lattice around the MOCs, revealing the adsorption geometry of the Cu adatoms in the chains. The Cu adatoms predominantly occupy bridge sites along the high-symmetry [110] lattice direction (Supporting Information, Note 3, Figure S6).

We performed DFT calculations to better understand the structures of the strained MOCs. These calculations indicated that the DBDMN monomers lie approximately 2.25 Å above the Cu(111) surface. Moreover, each DBDMN monomer adopts a bent configuration such that its methyl groups are lifted above the naphthalene backbone (Figure 3e). To enable direct comparison between the DFT results and experimental data, we generated simulated nc-AFM images of the DFT-relaxed models using a modified probe–particle model developed by Hapala et al.[21–23] The out-of-plane bending of the DBDMN monomer precludes direct visualization of the naphthalene rings' internal structure. Nevertheless, the calculated nc-AFM image (Figure 3d) exhibits all the characteristic features of our experimental images, including the bright features related to methyl groups. Additionally, the C–Cu–C coordination bonds are visible as distinct line features in the simulated nc-AFM images, and in good agreement with the experimental data. All these observations support the proposed model of the strained MOCs. AFM images of heterochiral MOCs also exhibited sharp line features linking methyl groups of adjacent DBDMN molecules. These line features are not attributed to the presence of chemical bonds but to the close proximity of the -CH_3 groups, which create sharp ridges in the potential energy landscape that induce bending of the CO probe–particle.[21]

Tip-induced dehydrogenation of methyl groups. Multiple STM imaging sessions involving scanning at a bias voltage (V_S) of $V_S \geq 1.6$ V induced irreversible structural changes in the MOCs. By acquiring a series of STM and nc-AFM images, we were able to capture the structural evolution of individual MOCs after stepwise scanning at $V_S = 2$ V (Figure 3). We first performed STM imaging of the lower part of a strained MOC at $V_S = 2$ V to trigger tip-induced structural change. We then switched to a constant height nc-AFM imaging to capture structural changes in the MOCs (Figures 3b,g).

The naphthalene rings of each DBDMN monomer become well resolved in the nc-AFM images of the partially dehydrogenated MOC (Figure 3g), and the line feature (indicated by a white arrow) associated with the C–Cu–C bond was more clearly visible than in the corresponding image of the parent strained MOC. Applying the same imaging protocol (scanning at $V_S = 2$ V) to the upper part of this MOC caused the STM and nc-AFM contrast to become uniform over the entire MOC backbone (Figures 3c,h). These

observations indicate that the methyl groups (-CH_3) of the DBDMN monomers underwent monodehydrogenation to produce -CH_2 radicals, leading to changes in both STM and nc-AFM contrast. We therefore performed DFT calculations for a new MOC structure in which the DBDMN monomers have monodehydrogenated methyl groups (-CH_2) and a planar molecular adsorption geometry (Figure 3j).

The experimental nc-AFM images of the dehydrogenated homochiral MOC are reproduced well by their simulated counterpart (Figure 3i). Interestingly, dehydrogenation has no appreciable effect on the spatial locations of intramolecular features and therefore clearly does not induce intermolecular rearrangements or affect the C–Cu–C bonding motif. Moreover, the dehydrogenation of -CH_3 groups enables direct visualization of the C–Cu–C bond, as evidenced by the sharp lines connecting the DBDMN backbone units. We could thus use this tip-controlled dehydrogenation technique to elucidate the mechanism of the isomeric transformation of the MOCs.

Structural characterization of relaxed MOCs. After prolonged room-temperature annealing under UHV conditions, the MOCs undergo a structural rearrangement and adopt a new relaxed isomeric form. To illustrate the structural rearrangements that occur during this process, we conducted STM and nc-AFM imaging of a partially relaxed MOC before (Figures 4a–c) and after (Figures 4d,e) dehydrogenation of methyl groups. The lower part of this MOC consists predominantly of strained homochiral junctions, while the upper part features a series of dumbbell-shaped junctions (indicated by white arrows in Figure 4a), presumably because of the presence of a distinct C–Cu–C coordination bonding motif. Bond-resolved nc-AFM images (Figure 4e) of the same dehydrogenated MOC show that each dumbbell-shaped junction consists of one Cu adatom coordinated to one C(Br) σ-radical site and one C(H) σ-radical site. Conversely, in the strained homochiral MOC junctions each Cu adatom is coordinated to two C(Br) σ-radical sites. These different coordination motifs can be seen by examining representative homochiral MOC junctions in the strained (Figure 4f) and relaxed isomeric configurations (Figure 4g; for an image of a representative MOC with a higher degree of relaxation see the Supporting Information, Note 4).

Our bond-resolved nc-AFM images provided several deep insights into the structural transformation that relaxes the strained MOC upon room-temperature annealing. First, they showed that the relaxed MOC junctions could be derived from the strained homochiral or heterochiral MOCs by a shift of the Cu coordination center from C(Br) to an adjacent C(H) site together with the shift of a H atom from the C(H) to the formerly Cu-bound C(Br) site (Figure 1a). Second, the strained and relaxed MOCs exhibit different registries with respect to the Cu(111) lattice. The Cu adatoms in the strained MOC are aligned along the [110] direction whereas those in the relaxed MOCs align with a twist angle of about 20° relative to the strained MOC. The alignments of the two MOC types are indicated by the dashed white lines in Figure 4e. Third, the average separations between adjacent Cu coordination centers (that is, the Cu–Cu distances) were 7.6 ± 0.093 Å and 6.91 ± 0.085 Å for the strained and relaxed MOCs, respectively. The Cu adatoms tended to occupy the bridge sites of Cu(111). Therefore, the difference in the Cu–Cu distances observed for the two MOC types is tentatively attributed to the different interstitial separations of bridge sites along distinct lattice directions.

The substantial difference in the separation of nearest neighbor Cu atoms in the two MOC types indicates that the strain in the initial MOC may be the driving force of its isomeric transformation. To test this hypothesis, we used DFT to compute the total energies of the two MOC isomers with and without the Cu(111) substrate. The total energy difference between strained and relaxed freestanding MOC isomers is negligible (ca. 15 meV; Supporting Information, Note 6). Therefore, the energy gain as a consequence of electronic effects arising from the change in the binding configuration of the Cu adatoms and the naphthalene skeleton does not contribute significantly to the induction of isomerization. We also analyzed the Cu–Cu distances between nearest neighbor Cu adatoms in the optimized free-standing and surface-supported homochiral MOCs. This revealed that the Cu–Cu distance increases from 7.2 Å in the freestanding strained isomer to 7.67 Å in the surface-supported MOC. Conversely, the Cu–Cu distances in the freestanding and surface-supported relaxed MOC are 6.73 Å and 6.99 Å, respectively. Surface adsorption thus substantially increases the Cu–Cu distance in the strained MOC isomer (by 0.47 Å), indicating that the strain energy is probably stored in the elongated C–Cu–C coordination bonds. The calculations also show that the total energy of the relaxed MOC isomer on Cu(111) is approximately 0.28 eV lower than that of its strained counterpart. The transformation into the relaxed MOC isomeric configuration

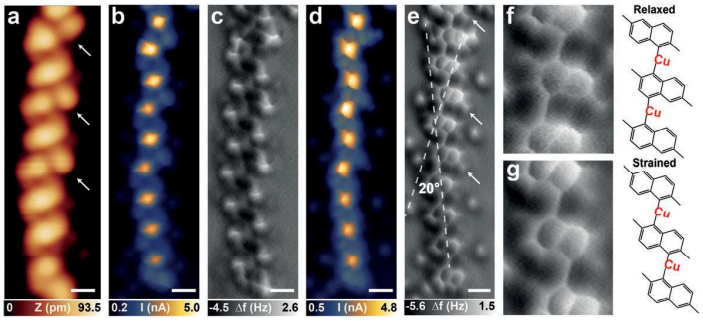

Figure 4. Probing strain-induced MOC relaxation. a) STM topography image of a partially relaxed MOC. b,c) Constant height STM current and nc-AFM images of the same MOC. d,e) Constant height STM current and nc-AFM images of the same MOC after methyl group dehydrogenation. f,g) Magnified view of the relaxed and strained homochiral MOC segments with the corresponding atomic models. The dashed white lines in image (e) indicate the differing registration of the relaxed and strained MOC segments with respect to the Cu(111) substrate. The STM topography image (a) was recorded using tunneling parameters of 1 V, 1 nA. Constant height images were collected at tip-sample distances of +100 pm (b,d) and +50 pm (c,e) with respect to a setpoint of 50 mV, 1 nA.

is thus favored because it minimizes the system's total energy.

Isomerization pathway. We explored multiple pathways for the isomerization process (Supporting Information, Note 6, Figure S11). A process involving a 1,3-H atom shift with a concomitant reorganization of the coordinate bonding from C(Br)–Cu–C(Br) to C(Br)–Cu–C(H) was found to be the most feasible of the considered possibilities. To obtain deeper insights into the reaction mechanism, we performed quantum mechanics/molecular mechanics (QM/MM) molecular dynamics (MD) simulations[24] to determine the free energy profile of reaction steps that might contribute to these skeletal rearrangements (Figure 5). These calculations also provided insight into the effect of temperature on the transformation mechanism, which was important (Supporting Information, Note 5). To identify the most feasible pathway, we considered various reaction coordinates for the first step of the process (for other possible pathways see the Supporting Information, Figure S11). Because the calculations were computationally expensive, only homochiral MOC junctions were considered. Figure 5 shows the reaction pathway for the isomeric relaxation of MOCs with the lowest activation energy according to our simulations. This pathway involves a two-step process with two activation barriers (Figure 5g). The first step is a rapid 1,3-H shift described by the $\delta H = h_3 - h_1$ reaction coordinate (Figure 5f). The shift presumably proceeds by translocation of the H atom on C3 onto the Cu adatom followed by addition across the C1–Cu bond via the transient structure depicted in Figure 5b; this process has a computed activation barrier of 1.18 eV. It may seem difficult to overcome such a barrier at 300 K. However, the reaction rate Γ is given by the expression $\Gamma = \nu e^{-\Delta F/kT}$, where ΔF is the free energy barrier, T is the temperature, k is Boltzmann's constant, and ν is the effective frequency associated with the vibrations in the direction of the reaction path.[25] In our case, the catalytic effect of the mechanical strain enhances these vibrational modes and thus increases the transition rate, facilitating the reaction. The subsequent rearomatization of the naphthalene backbone is accompanied by weakening of the C1–Cu bond and the formation of a new C3–Cu bond (Figure 5c). The energy of the resulting system is 0.5 eV higher than that of the initial state. Notably, the 1,3-H migration and formation of the C3–Cu bond are facilitated by thermal fluctuations in the vertical position of the Cu adatom (see the red curve in Figure 5h), which reduces the free energy barrier. During this step, the Cu adatom also migrates to an adjacent bridge site on the Cu(111) surface (Figures 5c,d). The isomerization is completed by the dissociation of the bond between the Cu adatom and the C1 atom (Supporting Information, Figure S9). Using this bond distance as a reaction coordinate, Δ(Cu–C), we traced the system's transformation to its final state (Figure 5e) and showed that it involves overcoming an activation barrier of 0.78 eV (Figure 5d). The dissociation of this bond allows the system to reach the relaxed configuration by releasing the stress of the intermediate structure. Importantly, our calculations also reveal a vertical movement of approximately 0.4 Å of the whole naphthalene unit as a consequence of the activation of out-of-plane molecular vibration modes at elevated temperatures. The temperature-induced vertical movement facilitates the reaction greatly by lowering the activation barrier. This clearly illustrates the importance of performing free energy calculations at elevated temperatures when seeking to correctly describe on-surface reaction mechanisms and the associated entropic effects.

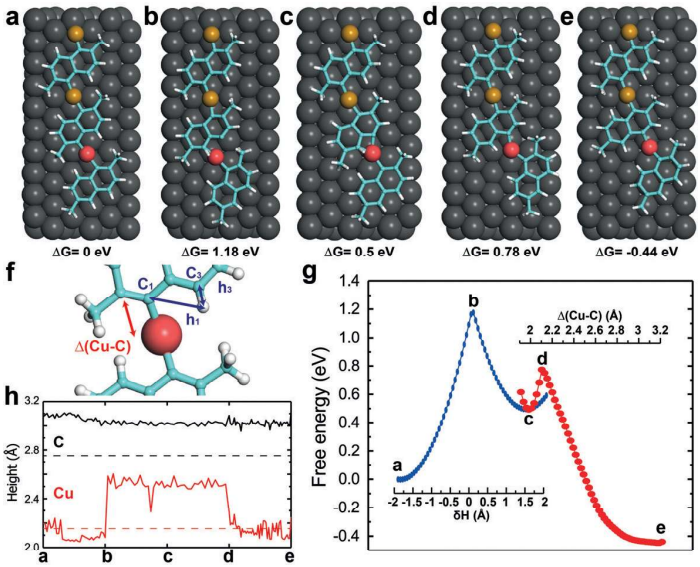

Figure 5. Free energy calculation for the proposed reaction pathways. a–e) Top view of the structures at different stages of the reaction. f) A depiction of important distances and the atoms participating in the reaction. h) Height of the Cu adatom (red) and average heights of the C atoms (black) during the reaction at 300 K; the heights of the corresponding atoms in the relaxed structure at 0 K are shown by the dashed lines. g) Free energy profile of the two-step reaction. The first part goes through the reaction coordinate $\delta H = h3 - h2$ and the second part through Δ(Cu–C).

C–Cu–C bond cleavage and C–H bond activation on catalytically active substrates typically require thermal treatment at over 400 K.[26–29] They are often followed by direct C–C coupling, leading to the formation of graphene-like nanostructures.[5,6] However, unlike the 2D MOC networks reported previously, the 1D strained MOCs studied here undergo C–Cu–C bond cleavage at room temperature as part of a complex reaction driven by the relief of substrate-induced strain.

Conclusion

In summary, we have demonstrated a strain-induced structural rearrangement of 1D MOCs on a Cu(111) surface at room temperature. Our results show that strain relief drives the skeletal rearrangement of MOCs, which involves concurrent rearrangements of Cu adatoms and H atoms together with the migration of monomers toward an energetically favorable registry on the Cu(111) substrate. This process is facilitated at elevated

temperatures by the vertical displacement of the MOC's organic backbone because of the activation of the out-of-plane vibrational modes. Theoretical calculations showed that the optimal reaction pathway is highly sensitive to entropic effects, illustrating the importance of performing free energy calculations at elevated temperatures when studying on-surface reaction mechanisms. These results may support the development of new strategies for fabricating functional materials and quantum nanostructures to be used in both fundamental research and new technologies.

Experimental Section

STM/nc-AFM measurements were performed on a commercial Omicron machine using a qPlus sensor with a resonant frequency of 28.2 kHz, quality factor of Q = 10500 and oscillation amplitude of 100 pm, operated in frequency-modulation mode.[30] DFT calculations were performed using the FHI-AIMS code.[31] All geometric optimizations were performed at the GGA-PBE[32] level, using light wave functions and the Tkatchenko–Scheffler[33] treatment of van der Waals interactions. We also used a QM/MM method, Fireball/Amber,[24] that combines classical force field techniques as implemented in Amber[34] with local orbital DFT calculations performed with Fireball.[35] The MM computations were performed using the interface force-field[36] and the DFT calculations used the BLYP exchange-correlation functional[37,38] with D3 corrections[39] and norm-conserving pseudopotentials together with a basis set of optimized numerical atomic-like orbitals.[40] The free energy profile was generated using the WHAM method.[41] Extended experimental and computational details are presented in the Supporting Information.

Acknowledgements

J.L. acknowledges the support from MOE Tier 2 grants (R-143-000-A06-112, R-143-000-682-112, and R-143-000-A75-114). P.J. acknowledges support from Praemium Academie of the Czech Academy of Sciences, the Ministry of Education of the Czech Republic Grant LM2015087 and GACR project No. 18–09914S. J.W. acknowledges financial support from the MOE Tier 3 program (MOE2014-T3-1–004). D.Q. acknowledges the support of the Australian Research Council (Grant No. FT160100207). Part of this research was undertaken on the Soft X-ray spectroscopy beamline at the Australian Synchrotron, part of ANSTO.

Conflict of interest

The authors declare no conflict of interest.

Stichwörter: Debromiierung · Isomerisierung · Metall-organische Strukturen · Rasterkraftmikroskopie · Rastertunnelmikroskopie

Zitierweise: *Angew. Chem. Int. Ed.* **2019**, *58*, 18591 – 18597
Angew. Chem. **2019**, *131*, 18764 – 18770

[1] C. Janiak, J. K. Vieth, *New J. Chem.* **2010**, *34*, 2366.
[2] S. Stepanow, N. Lin, J. V. Barth, *J. Phys. Condens. Matter* **2008**, *20*, 184002.
[3] M. Di Giovannantonio, M. El Garah, J. Lipton-Duffin, V. Meunier, L. Cardenas, Y. Fagot Revurat, A. Cossaro, A. Verdini, D. F. Perepichka, F. Rosei, G. Contini, *ACS Nano* **2013**, *7*, 8190.
[4] L. Grill, M. Dyer, L. Lafferentz, M. Persson, M. V. Peters, S. Hecht, *Nat. Nanotechnol.* **2007**, *2*, 687.
[5] J. Cai, P. Ruffieux, R. Jaafar, M. Bieri, T. Braun, S. Blankenburg, M. Muoth, A. P. Seitsonen, M. Saleh, X. Feng, K. Müllen, R. Fasel, *Nature* **2010**, *466*, 470.
[6] L. Talirz, P. Ruffieux, R. Fasel, *Adv. Mater.* **2016**, *28*, 6222.
[7] S. Clair, D. G. de Oteyza, *Chem. Rev.* **2019**, *119*, 4717.
[8] J. L. Howard, Q. Cao, D. L. Browne, *Chem. Sci.* **2018**, *9*, 3080.
[9] M. Treier, C. A. Pignedoli, T. Laino, R. Rieger, K. Müllen, D. Passerone, R. Fasel, *Nat. Chem.* **2011**, *3*, 61.
[10] A. Shiotari, T. Nakae, K. Iwata, S. Mori, T. Okujima, H. Uno, H. Sakaguchi, Y. Sugimoto, *Nat. Commun.* **2017**, *8*, 16089.
[11] Q. Zhong, D. Ebeling, J. Tschakert, Y. Gao, D. Bao, S. Du, C. Li, L. Chi, A. Schirmeisen, *Nat. Commun.* **2018**, *9*, 3277.
[12] J. Liu, B. Xia, H. Xu, N. Lin, *J. Phys. Chem. C* **2018**, *122*, 13001.
[13] L. Gross, F. Mohn, N. Moll, P. Liljeroth, G. Meyer, *Science* **2009**, *325*, 1110.
[14] D. G. de Oteyza, P. Gorman, Y.-C. Chen, S. Wickenburg, A. Riss, D. J. Mowbray, G. Etkin, Z. Pedramrazi, H.-Z. Tsai, A. Rubio, M. F. Crommie, F. R. Fischer, *Science* **2013**, *340*, 1434.
[15] S. Kawai, A. Sadeghi, T. Okamoto, C. Mitsui, R. Pawlak, T. Meier, J. Takeya, S. Goedecker, E. Meyer, *Small* **2016**, *12*, 5303.
[16] N. Kocić, X. Liu, S. Chen, S. Decurtins, O. Krejčí, P. Jelínek, J. Repp, S.-X. Liu, *J. Am. Chem. Soc.* **2016**, *138*, 5585.
[17] F. Queck, O. Krejčí, P. Scheuerer, F. Bolland, M. Otyepka, P. Jelínek, J. Repp, *J. Am. Chem. Soc.* **2018**, *140*, 12884.
[18] W. Wang, X. Shi, S. Wang, M. A. Van Hove, N. Lin, *J. Am. Chem. Soc.* **2011**, *133*, 13264.
[19] Q. Sun, L. Cai, S. Wang, R. Widmer, H. Ju, J. Zhu, L. Li, Y. He, P. Ruffieux, R. Fasel, W. Xu, *J. Am. Chem. Soc.* **2016**, *138*, 1106.
[20] J. Liu, Q. Chen, K. Cai, J. Li, Y. Li, X. Yang, Y. Zhang, Y. Wang, H. Tang, D. Zhao, K. Wu, *Nat. Commun.* **2019**, *10*, 2545.
[21] P. Hapala, G. Kichin, C. Wagner, F. S. Tautz, R. Temirov, P. Jelínek, *Phys. Rev. B* **2014**, *90*, 085421.
[22] P. Hapala, M. Švec, O. Stetsovych, N. J. van der Heijden, M. Ondráček, J. van der Lit, P. Mutombo, I. Swart, P. Jelínek, *Nat. Commun.* **2016**, *7*, 11560.
[23] O. Krejčí, P. Hapala, M. Ondráček, P. Jelínek, *Phys. Rev. B* **2017**, *95*, 045407.
[24] J. I. Mendieta-Moreno, R. C. Walker, J. P. Lewis, P. Gómez-Puertas, J. Mendieta, J. Ortega, *J. Chem. Theory Comput.* **2014**, *10*, 2185.
[25] G. H. Vineyard, *J. Phys. Chem. Solids* **1957**, *3*, 121.
[26] Q. Li, B. Yang, J. Björk, Q. Zhong, H. Ju, J. Zhang, N. Cao, Z. Shi, H. Zhang, D. Ebeling, A. Schirmeisen, J. Zhu, L. Chi, *J. Am. Chem. Soc.* **2018**, *140*, 6076.
[27] L. Ferrighi, I. Píš, T. H. Nguyen, M. Cattelan, S. Nappini, A. Basagni, M. Parravicini, A. Papagni, F. Sedona, E. Magnano, F. Bondino, C. Di Valentin, S. Agnoli, *Chem. Eur. J.* **2015**, *21*, 5826.
[28] Q. Fan, S. Werner, J. Tschakert, D. Ebeling, A. Schirmeisen, G. Hilt, W. Hieringer, J. M. Gottfried, *J. Am. Chem. Soc.* **2018**, *140*, 7526.
[29] M. Fritton, K. Otte, J. Björk, P. K. Biswas, W. M. Heckl, M. Schmittel, M. Lackinger, *Chem. Commun.* **2018**, *54*, 9745.
[30] F. J. Giessibl, *Appl. Phys. Lett.* **1998**, *73*, 3956.
[31] V. Blum, R. Gehrke, F. Hanke, P. Havu, V. Havu, X. Ren, K. Reuter, M. Scheffler, *Comput. Phys. Commun.* **2009**, *180*, 2175.
[32] J. P. Perdew, K. Burke, M. Ernzerhof, *Phys. Rev. Lett.* **1996**, *77*, 3865.
[33] A. Tkatchenko, M. Scheffler, *Phys. Rev. Lett.* **2009**, *102*, 073005.

[34] D. A. Case, I. Y. Ben-Shalom, S. R. Brozell, D. S. Cerutti, T. E. Cheatham III, V. W. D. Cruzeiro, T. A. Darden, R. E. Duke, D. Ghoreishi, M. K. Gilson, et al., AMBER **2018**, University of California, San Francisco 2018.
[35] J. P. Lewis, P. Jelínek, J. Ortega, A. A. Demkov, D. G. Trabada, B. Haycock, H. Wang, G. Adams, J. K. Tomfohr, E. Abad, H. Wang, D. A. Drabold, *Phys. Status Solidi B* **2011**, *248*, 1989.
[36] H. Heinz, T. J. Lin, R. Kishore Mishra, F. S. Emami, *Langmuir* **2013**, *29*, 1754.
[37] A. D. Becke, *Phys. Rev. A* **1988**, *38*, 3098.
[38] C. Lee, W. Yang, R. G. Parr, *Phys. Rev. B* **1988**, *37*, 785.
[39] S. Grimme, S. Ehrlich, L. Goerigk, *J. Comput. Chem.* **2011**, *32*, 1456.
[40] M. Basanta, Y. Dappe, P. Jelínek, J. Ortega, *Comput. Mater. Sci.* **2007**, *39*, 759.
[41] S. Kumar, J. M. Rosenberg, D. Bouzida, R. H. Swendsen, P. A. Kollman, *J. Comput. Chem.* **1992**, *13*, 1011.

Manuskript erhalten: 20. Juli 2019
Veränderte Fassung erhalten: 21. September 2019
Akzeptierte Fassung online: 13. Oktober 2019
Endgültige Fassung online: 4. November 2019

Angewandte Chemie
Eine Zeitschrift der Gesellschaft Deutscher Chemiker

Supporting Information

Strain-Induced Isomerization in One-Dimensional Metal–Organic Chains

Mykola Telychko[+], Jie Su[+], Aurelio Gallardo[+], Yanwei Gu, Jesús I. Mendieta-Moreno, Dongchen Qi, Anton Tadich, Shaotang Song, Pin Lyu, Zhizhan Qiu, Hanyan Fang, Ming Joo Koh, Jishan Wu, Pavel Jelínek,* and Jiong Lu**

ange_201909074_sm_miscellaneous_information.pdf
ange_201909074_sm_movie_reac.mpg

Table of Contents

Experimental Procedures

Synthesis and characterization of organic precursor:

A solution of bromine (0.33 mL, 6.5 mmol) in anhydrous DCM (10 mL) was added dropwise to a solution of compound 2,6-dimethylnaphthalene (0.5 g, 3.2 mmol) and iodine (0.1g) in anhydrous DCM (50 mL) at 0 ℃ in the darkness. The resulting mixture was stirred for extra 1.5 h. Br_2 was neutralized with $Na_2S_2O_3$ solution. The organic layer was extracted with DCM (20 mL*3), dried over Na2SO4, filtered and evaporated to dryness. The residue was purified by column chromatography (silica gel, hexane) to give the compound DBDMN as white solid in 48% yield (0.481 g). 1H NMR (400 MHz, Chloroform-d): δ 8.19 (d, J = 8.6 Hz, 2H), 7.42 (d, J = 8.6 Hz, 2H), 2.62 (s, 6H). The purity of resulting compound DBDMN was verified by nuclear magnetic resonance (NMR) spectroscopy presented in Figure S1.

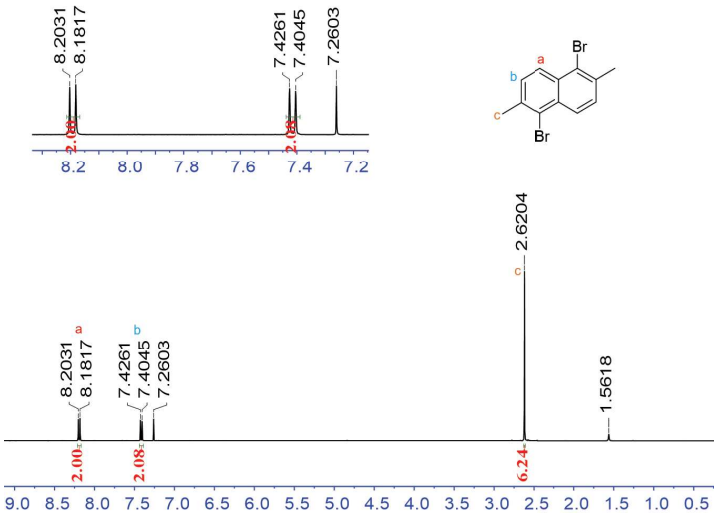

Figure S1. NMR characterization of the resulting DBDMN compound.

STM/nc-AFM measurements: The STM and nc-AFM experiments were performed in ultra-high vacuum conditions (base pressure > 1×10−10 mbar) at temperature 4.4 K using a commercial Omicron low temperature STM/AFM system. The Cu(111) single crystal (MaTeck GmbH) was cleaned by multiple cycles of Ar^+ sputtering and annealing. We used the qPlus sensor with a resonant frequency of 28.2 kHz, quality factor of Q=10500 and oscillation amplitude of 100 pm, operated in frequency-modulation mode.[1] The DBDMN precursor was deposited at room temperature from quartz crucible onto freshly prepared Cu(111) surface.

AFM simulations: The AFM images were calculated using the probe particle model.[2] The parameters used include a stiffness of 0.24 Nm^{-1} and a charge correction of -0.5 e. The electrostatic force was included in the AFM calculations using the Hartree potential calculated by DFT.

DFT method: We employed Density Functional Theory calculations using the FHI-AIMS code[3] to study our systems. Due to different registry with the substrate of the strained and relaxed structures, two different supercells were used to describe the Cu(111) surface. An 8x9 hexagonal cell was used to model the strained structure. To model the relaxed structure, it was necessary to modify an orthorhombic supercell with a 12° rotation of the y axis with respect to z axis to obtain a 8x(2$\sqrt{}$17)-R102° cell in Wood notation. Both supercells consist three Cu layers. All the atoms of the slab excluding the bottom Cu layer were allowed to relax until a decrease of the remaining atomic forces and the total energy below 10^{-2} eV/Å and 10-5 eV respectively. A Monkhorst-Pack grid of 1x10x1 was used for the integration in the Brillouin zone. All the geometric optimizations were performed at the GGA-PBE[4] level, using light wave functions and including the Tkatchenko-Scheffler [5] treatment of the van der Waals interactions.

QM/MM method: In this study, we used a QM/MM method, Fireball/Amber[6] based on the combination of classical force field techniques with Amber[7] and local orbital DFT with Fireball[8]. In the MM part we used the interface force-field[9] and in the DFT calculations, we used the BLYP exchange correlation functional[10,11] with D3 corrections[12] and norm-conserving pseudopotentials. We employed a basis set of optimized numerical atomic-like orbitals (NAOs)[13] with a 1s orbital for H, sp3 orbitals for C and sp3d5 orbitals for Cu atoms. The QM region contains 98 atoms: 3 molecules, 3 adatoms and 28 Cu atoms of the surface. The rest of the Cu surface atoms included in the MM region creating a total size the system is 1570 atoms. Before the calculation of the free energy profile we have perform a QM/MM geometry relaxation followed by a thermalization of the system from 100K to 300K in order to stabilize the system. The free energy profile was performed with the WHAM method.[14] To construct the free energy profile we made 66 windows of umbrella sampling from -1.8 Å to 2.0 Å for the δH reaction coordinate and 55 windows from 1.9 Å to 3.25 Å for Δ(Cu-C) distance. In each window we run a QM/MM MD of 2000 steps at 300 K with a time step of 0.5 fs.

Results and Discussion

1. Photoelectron spectroscopy study of MOC on Cu(111)

The X-ray photoelectron spectroscopy (XPS) was conducted to probe the chemical state of DBDMN precursor deposited onto Cu(111) surface at room temperature (Figure S2). The C 1s spectra reveal one prominent feature peaked at 284.5 eV and one weaker satellite peak at 283.5 eV. The main peak and satellite peak are associated to DBDMN monomers and as-formed Cu-C bonds respectively.[15-19] The XPS spectrum of Br 3p (Figure S1 b) reveals a lineshape characteristic for cleaved Br adatoms chemisorbed on Cu(111) surface[15], which is an additional evidence for occurrence of the DBDMN dehalogenation.

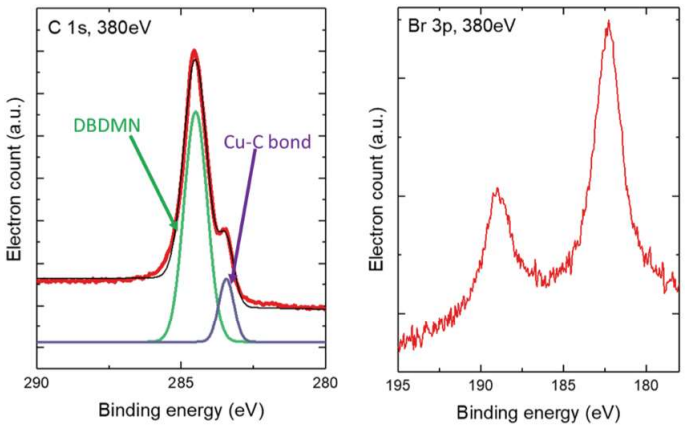

Figure S2. Photoelectron spectroscopy study. XPS core level spectra of (a) C1s and (b) Br 3p, measured directly after the deposition of DBDMN molecules on Cu(111) surface at room temperature.

2. nc-AFM imaging of homochiral and heterochiral MOC junctions

Supplementary Figure S3 and S4 show additional constant height STM current and nc-AFM images of individual homochiral and heterochiral MOCs, acquired at various tip-sample distances. At a large tip-sample distance, the strongest Pauli repulsion is observed over methyl groups of individual DBDMN momomers with bend confirmation (Figure 5f in main text), consistent with the results revealed by the df versus tip-sample distance (df(z)) curves (Figure S5). A further decrease of tip-sample distance allows us to visualize the features related to the naphthalene backbone and Cu adatoms.

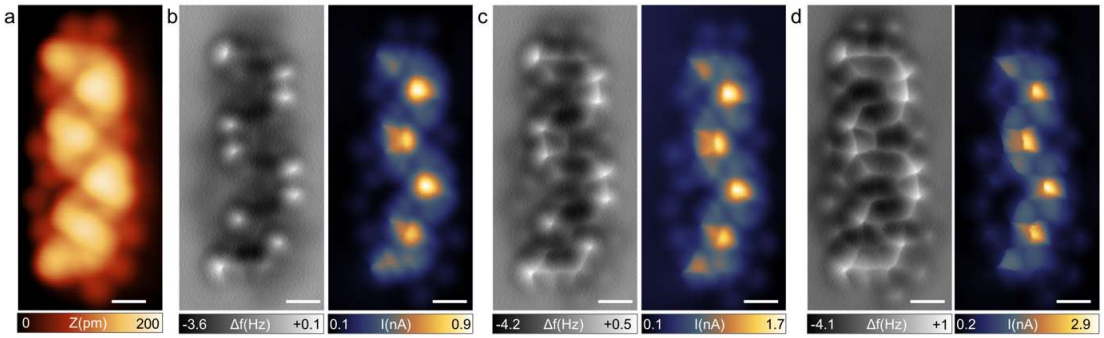

Figure S3. STM topography, constant height current (I) and nc-AFM (df) images of a heterochiral MOC collected at different tip-sample distances using a CO-functionalized tip. Tunnelling parameters for STM topography image (a): 1 V, 1 nA. Constant height current and nc-AFM images were collected at the tip-sample distance corresponding to set point (SP) 50 mV, 1 nA +200 pm (b), 150 pm (c), 140 pm (d) . Scale bar is 500 pm for all the images.

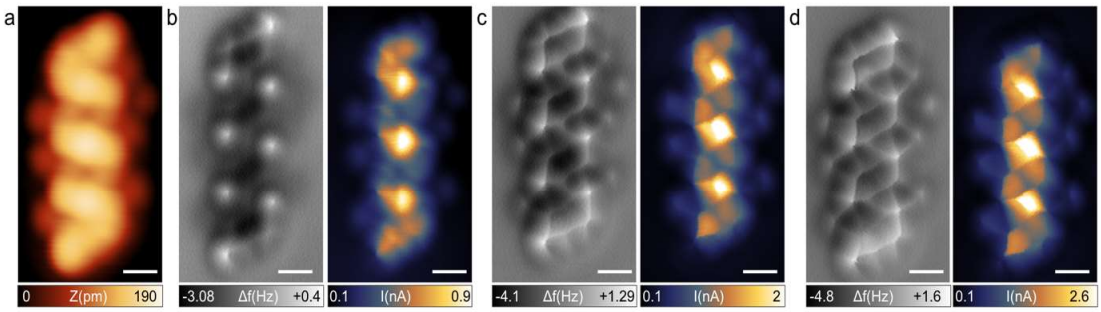

Figure S4. STM topography, constant height current (I) and nc-AFM (df) images of a homochiral MOC collected at different tip-sample distances using a CO-functionalized tip. Tunneling parameters for STM topography image (a): 1 V, 1 nA. Constant height current and nc-AFM images were collected at the tip-sample distance corresponding to set point (SP) 50mV, 1nA + 100 pm (b), +50 pm (c), +30 pm (d). Scale bar is 500 pm for all the images.

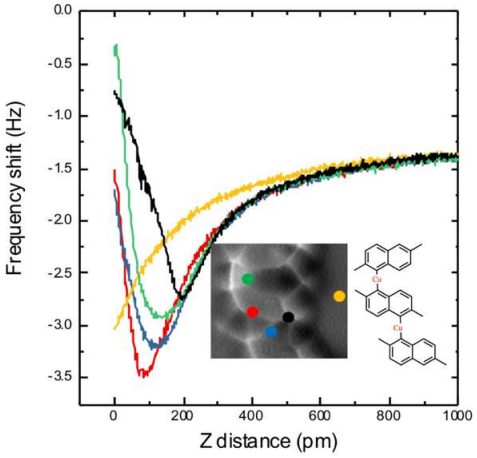

Figure S5. Frequency shift versus tip-sample distance curves (df(z)) collected over different specific sites of a MOC. Coloured circles mark positions where individual df(z) curves were acquired. The zero tip-sample distance is defined with respect to the set point of Vs=50 mV; I=1 nA

3. Determine the adsorption geometry of a MOC on Cu(111)

In order to probe the adsorption geometry of a MOC on the substrate, we imaged the atomic lattice of the Cu(111) substrate surrounding a MOC (see Figure S6). Superimposing the Cu(111) lattice over the MOC allows us to determine the adsorption site of Cu coordination centers. It is found that Cu adatoms predominantly occupy the bridge sites.

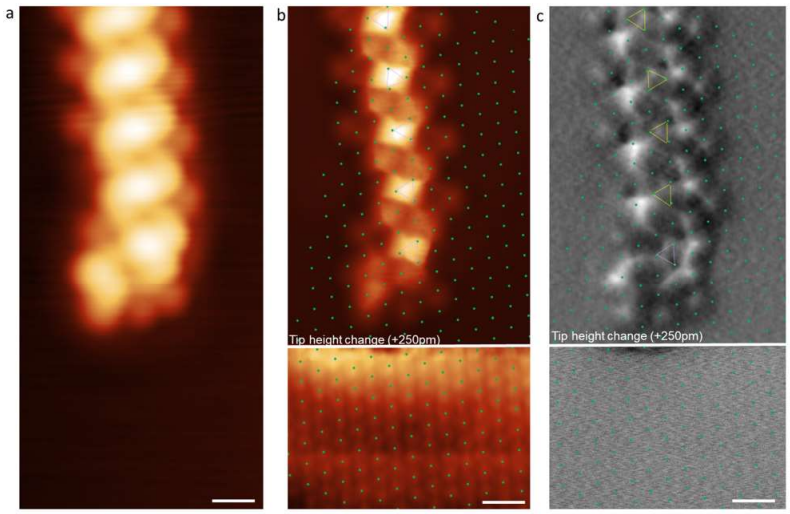

Figure S6. Probe the adsorption geometry of a MOC on Cu(111) (a) STM topography image of a MOC on Cu(111). (b) the corresponding constant-height current and (c) nc-AFM image respectively. Note: the tip sample distance was varied near the end of MOC in order to resolve the adsorption geometry of this MOC with respect to Cu(111) lattice. Green dots indicate top sites of the Cu(111) lattice. Scale bars are 500 pm for all the images.

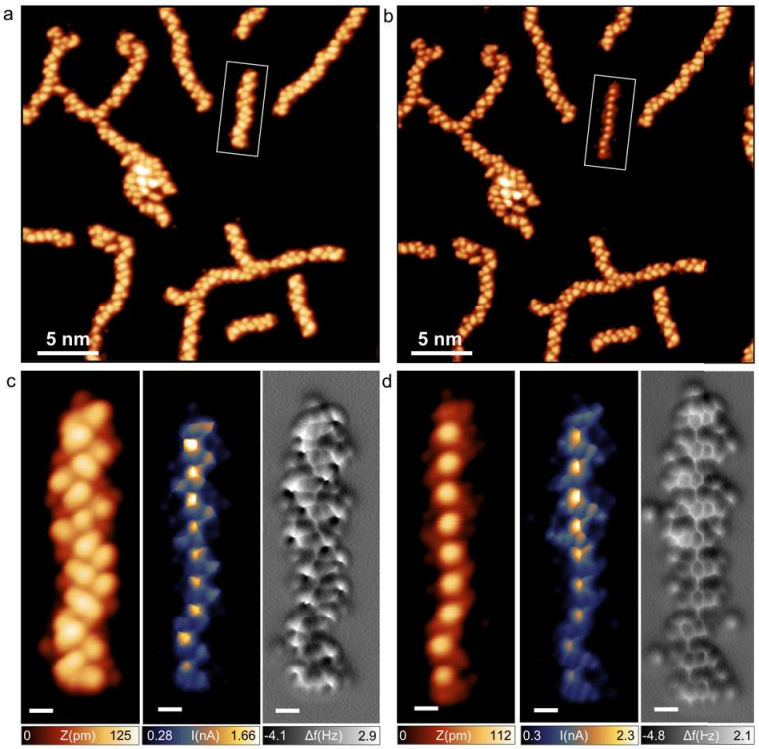

Figure S7. Tip-induced dehydrogenation of methyl groups of a relaxed MOC. (a,b) Large-scale STM image of the same area prior (a) and after (b) dehydrogenation of individual MOCs. The methyl groups of a MOC marked by a white rectangle were dehydrogenated via tip-assisted manipulation (scanning at 2V). (c, d) Topography (left), constant height STM (middle) and nc-AFM (right) images of a MOC prior (c) and after (d) dehydrogenation of its methyl groups.

4. Dehydrogenation of methyl groups of a relaxed MOC

Figure S7 shows results of the tip-induced dehydrogenation of methyl groups to better visualize the internal structure of a relaxed MOC. Individual MOCs marked by a white rectangle in Figure S7 a, b were imaged at Vs=2 V. Prior to the dehydrogenation, nc-AFM image of this MOC reveals characteristic features of individual DBDMN building block including rectangular features (naphtalene backbone) and bright apices (-CH_3 groups). In contrast, nc-AFM image of the dehydrogenated MOC with a planar conformation (Figure S7d) clearly resolves the internal structure of MOC including DBDMN backbones and C-Cu-C bond.

5. Temperature effects on the MOC isomerization

We also studied temperature dependent behaviour of this 1D system to better understand the temperature effect on isomeric transformation process. Figure S8 presents the temperature effect on the vertical position of the DBDMN naphthalene skeletons and Cu adatom. Firstly, the vertical positions of both monomers and Cu adatom tend to increase as temperature raises, which reduces the binding strength of DBDMN naphthalene skeletons with the substrate. Secondly, high temperature tends to increase the oscillation amplitude of out-of-plane vibrational modes, which otherwise will be quenched at low temperature. Such an effect allows system to explore many different states and eventually find most favourable reaction pathway. Thirdly, comparing the vertical position of the Cu adatom at different temperatures, we observe a vibrational mode present at higher temperatures that disappears for low temperatures at some point between 100K and 50K. These results indicate that the reaction may proceed under different reaction pathway at sufficiently low temperature.

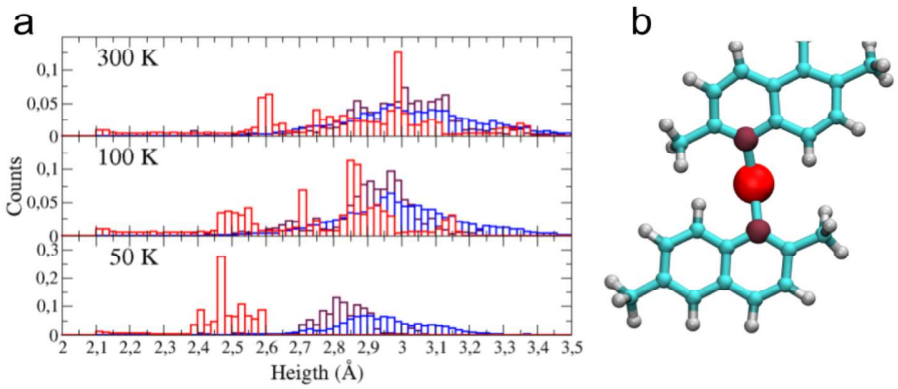

Figure S8. Temperature effect on the MOC isomerization (a) Histogram of the vertical position of different atoms of the strained homochiral MOC at different temperatures (50 K, 100 K, 300 K) during 2000 time steps of a molecular dynamics. The blue bars represent all the carbon atoms in these molecules; the purple ones represent the two C atoms coordinated by the Cu adatom and the red one refers to the Cu adatom. The counts were normalized to the number of atoms and time steps. (b) Molecular structure with the atoms color-coded correspondingly to the histogram colours for clearance.

6. Driving mechanism of the MOC isomerization

To determine the main driving mechanism of the reaction, we studied different gas phase structures before and after the isomerization. In Figure S9 we show the characteristic distances and the energy differences in relaxed and strained isomeric configuration for: i) freestanding individual DBDMN monomer with two Cu atoms attached, ii) freestanding infinite MOC iii) on surface supported infinite MOC.

We first analysed the bond length of an isolated DBDMN monomer bonded to two Cu adatoms (see Figure S8a) in order to evaluate possible variations of the aromaticity of the phenyl rings. Importantly, we do not observe significant changes in the bond length or total energy gain. We thus exclude hypothesis that reaction is driven by a seeking of aromaticity. In next, we analyzed an infinite freestanding strained and relaxed MOCs (see Figure S8b). We observe energy difference of only a 15.2 meV. In addition, the Cu-Cu distance is 7.2

Å (6.73 Å) for strained (relaxed) MOC isomer, respectively. Finally, we studied modifications of infinite MOC imposed by its coordination with the Cu(111) substrate (see Figure S9c). For this we compare the Cu-Cu distances of surface supported MOC with freestanding MOC. Comparison indicates the overall increase of Cu-Cu distance by 6.5% and 4% for strained and relaxed MOC respectively. Which suggests presence of a mechanical strain in strained MOC. This strain also implies substantial energy difference of 0.28 eV between the strained and relaxed MOC. We note that, to ensure a proper precision for energies estimation, we employed the hybrid exchange and correlation potential b3lyp [20].

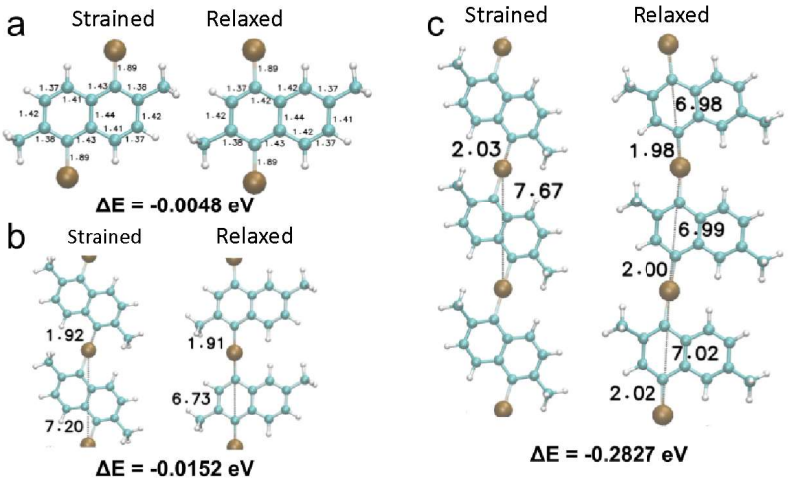

Figure S9. Calculation of the bond length and total energy of the strained and relaxed MOC in the (a) an isolated DBDMN molecule (b) an infinite freestanding MOCs with and (c) an infinite MOC adsorbed on Cu(111) surface. Below each pair of structures, the indicated ΔE is the result of subtract the total energy of the intact structure from the total energy of the relaxed structure. The energies are normalized per molecule. All the distances indicated in the figure are in presented in Å units.

Table S1. Absorption energy of the strained and relaxed infinite MOC adsorbed on the Cu(111) substrate. The energy is calculated as the energy of the total system minus the substrate and the MOC relaxed separately. The shifted energy is defined with the absorption energy of the strained MOC structure as the origin. Both energies are normalized per molecule

	Strained MOC	Relaxed MOC
Adsorption energy (eV)	-3.8087	-4.4801
Shifted adsorption energy	0	-0.6715

Our calculations yield that the most credible isomerization pathway is the one schematically depicted in Figure 10. This isomerization process is initiated by H atom translocation to the Cu adatom. In next, the lack aromaticity of DBDMN backbone facilitates further H migration to C1 site. The rearomatisation of naphthalene backbone occurs through breaking Cu-C1 bond and establishment of new C-C3 bond (see also Figure 5 in main text). Refer also to Supporting video 1.

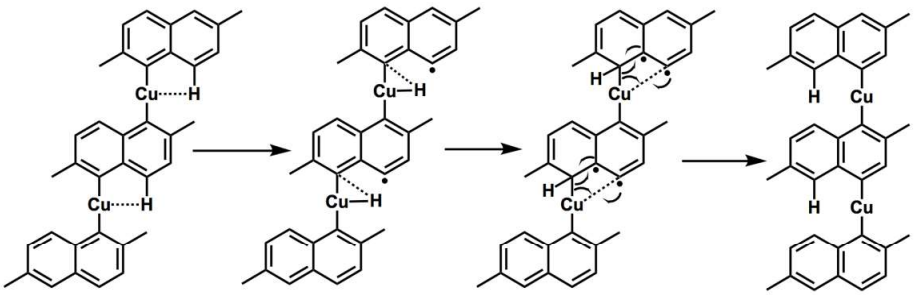

Figure S10. Detailed pathway of the isomerization process of MOC comprised by three DBDMN monomers.

SUPPORTING INFORMATION

To complete our study of the energy at 0K, we calculated the absorption energy per molecule of the infinite chains on a three-layer Cu(111) substrate (see Table S1). In agreement with the gas phase results and the obtained with molecular dynamics QMMM methods, we found the absorption of the structure after the reaction to be ~0.67 eV more favourable.

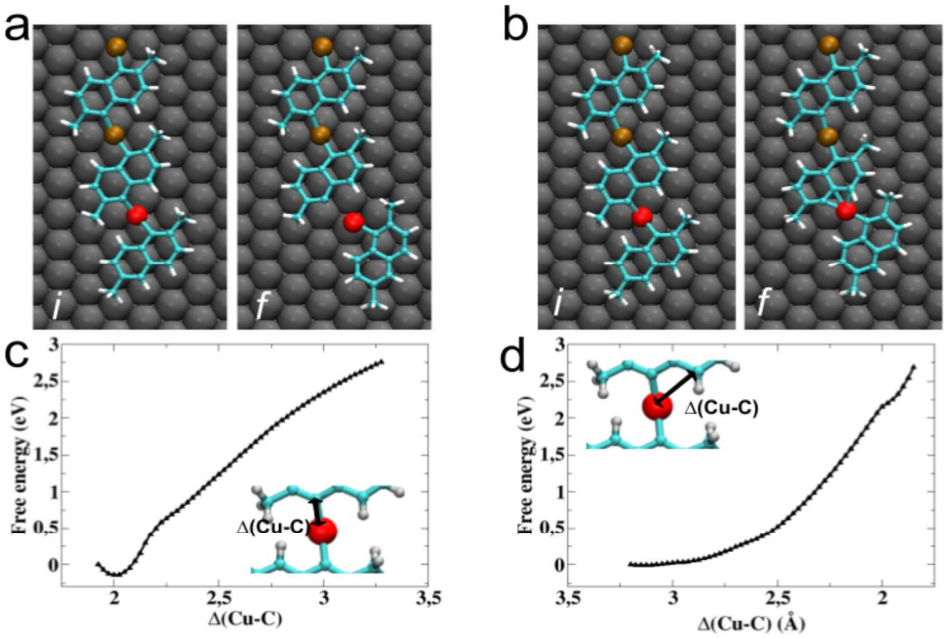

Figure S11. Alternative reaction pathways (a) pulling the Cu adatom away from the C (b) pushing the Cu adatom closer to the C atom. (c) Free energy barrier for (a). (d) Free energy barrier for (b).

We explored alternative reaction pathways to ensure that the one discussed in main text is energetically favorable one. Here we consider two alternative scenarios that start from the dislocation of the cooper adatom. Figure S11a shows the initial and final structures of a reaction scenario that consists in pulling the Cu adatom away from the C atom. That provokes the MOC breakage and, as a consequence, the free energy increases without reaching any minima (see Figure S11c). Figure 11b depicts another scenario initiated by forcing the Cu adatom to get closer to the other C atom. In this case the Cu adatom interacts unexpectedly with the molecule and the substrate, breaking the planarity of the system. This case also presents a high energy barrier (see Figure S11c) that does result in any stable configuration, so it was also discarded.

References

[1] F. J. Giessibl, *Applied Physics Letters* **1998**, 73, 3956–39584.

[2] P. Hapala, G. Kichin, C. Wagner, F. S. Tautz, R. Temirov, P. Jelínek, *Phys. Rev. B* **2014**, 90, 085421.

[3] V. Blum, R. Gehrke, F. Hanke, P. Havu, V. Havu, X. Ren, K. Reuter, M. Scheffler, *Computer Physics Communications* **2009**, 180 (11), 2175.

[4] J. P. Perdew, K. Burke, M. Ernzerhof, *Phys. Rev. Lett.* **1997**, 77 (18), 3865.

[5] A. Tkatchenko, M. Scheffler, *Phys. Rev. Lett.* **2009**, 102 (7), 073005.

[6] J. I. Mendieta-Moreno, R. C. Walker, J. P. Lewis, P. Gómez-Puertas, J. Mendieta, J. Ortega, *Journal of Chemical Theory and Computation* **2014**, 10 (5), 2185.

[7] D. A. Case, I.Y. Ben-Shalom, S. R. Brozell, D. S. Cerutti, T.E. III Cheatham, V. W. D. Cruzeiro, T. A. Darden, R. E. Duke, D. Ghoreishi, M. K. Gilson *et al.* AMBER **2018**, University of California, San Francisco 2018.

[8] J. P. Lewis, P. Jelínek, J. Ortega, A. A. Demkov, D. G. Trabada, B. Haycock, ,H. Wang, G. Adams, J. K. Tomfohr, E. Abad, H. Wang, D. A. Drabold, *Physica status solidi (b)* **2011** 248 (9), 1989.

[9] H. Heinz, T. J. Lin, R. Kishore Mishra, F. S. Emami, *Langmuir* **2013**, 29 (6), 1754.

[10] A. D. Becke, Density-functional exchange-energy approximation with correct asymptotic behavior. *Phys. Rev. A* **1988**, 38 (6), 3098.

[11] C. Lee, W. Yang, R. G. Parr, *Phys. Rev. B* **1988**, 37 (2), 785.

[12] S. Grimme, S. Ehrlich, L. Goerigk, *J. Comput. Chem.* **2011** 32 (7), 1456.

[13] M. Basanta, Y. Dappe, P. Jelínek, J. Ortega, *Computational Materials Science* **2007**, 39 (4), 759-766.

[14] S. Kumar, J. M. Rosenberg, D. Bouzida, R. H. Swendsen, P. A. Kollman, *Journal of Computational Chemistry* **1992**, 13 (8), 1011.

[15] M. Di Giovannantonio, M. El Garah, J. Lipton-Duffin, V. Meunier, L. Cardenas, Y. Fagot Revurat, A. Cossaro, A. Verdini, D. F. Perepichka, F. Rosei, G. Contini, *ACS Nano* **2013**, 7 (9), 8190.

[16] M. Di Giovannantonio, M. El Garah, J. Lipton-Duffin, V. Meunier, L. Cardenas, Y. Fagot Revurat, A. Cossaro, A. Verdini, D. F. Perepichka, F. Rosei, G. Contini, *ACS Nano* **2013**, 7 (9), 8190.

[17] Q. Fan, L. Liu, J. Dai, T. Wang, H. Ju, J. Zhao, J. Kuttner, G. Hilt, J. M. Gottfried, J. Zhu, *ACS Nano, **2018**, 12(3), 2267.*

[18] G. Galeotti, F. De Marchi, T. Taerum, L. V. Besteiro, M. El Garah, J. Lipton-Duffin, M. Ebrahimi, D. F. Perepichka, F. Rosei, *Chem. Sci., **2019**, 10, 5167.*

[19] M. Di Giovannantonio, M. Tomellini, J. Lipton-Duffin, G. Galeotti, M. Ebrahimi, A. Cossaro, A. Verdini, N. Kharche, V. Meunier, G. Vasseur, Y. Fagot-Revurat, D. F. Perepichka, F. Rosei, G. Contini, *J. Am. Chem. Soc.* **2016**, 138(51), 16696.

[20] X. Ren, P. Rinke, V. Blum, J. W., A. Tkatchenko, A. Sanfilippo, K. Reuter, M. Scheffler, *New Journal of Physics **2012***, 14, 053020.

Author Contributions

M.T., J.S. and A.G. contributed equally to this work. J.L, P.J and J. W are a corresponding authors

J.L. supervised the projects. M.T., J.S. performed STM, nc-AFM measurements and data analysis. Y.G., synthesized and characterized the molecular precursor under the supervision of J.W. A.G. and J. M.-M. performed the theoretical calculations under the supervision of P.J. All authors contributed to the scientific discussion and helped in writing the manuscript.